https://doi.org/10.15388/vu.thesis.23

VILNIUS UNIVERSITY
CENTER FOR PHYSICAL SCIENCES AND TECHNOLOGY

Aušra
BARADOKĖ

Fabrication of Miniaturised Electrochemical Sensor for Cancerogenic Biomarker Detection

DOCTORAL DISSERTATION

Natural Sciences,
Chemistry (N003)

Vilnius, 2019

Dissertation prepared 2014-2018 m., at the Center for Physical Sciences and Technology. The research was carried out in 2014-2018 during international collaboration between the State Research Institute Center for Physical Sciences and Technology, Lithuania and Dublin City University, Ireland and Trinity College Dublin, Ireland.

Academic supervisor - prof. dr. Rasa Pauliukaite (Center for Physical Sciences and Technology, Natural Science, Chemistry - N003)

Academic consultants:

- **Dr. Ramūnas Valiokas** (Center for Physical Sciences and Technology, Natural Science, Physics - N002)
- **Prof. dr. Kim McKelvey** (Trinity College Dublin, Ireland, Natural Science, Chemistry - N003)
- **Prof. dr. Robert Forster** (Dublin City University, Ireland, Natural Science, Chemistry - N003)

https://doi.org/10.15388/vu.thesis.23

VILNIAUS UNIVERSITETAS
FIZINIŲ IR TECHNOLOGIJŲ MOKSLŲ CENTRAS

Aušra
BARADOKĖ

Miniatiūrizuotas elektrocheminis jutiklis vėžio biožymenų tyrimams

DAKTARO DISERTACIJA

Gamtos mokslai,
Chemija (N003)

Vilnius, 2019

Disertacija rengta 2014-2018 m., Fizinių ir technologijos mokslų centre. Mokslinis tyrimas atliktas 2014-2018 m., bendradarbiaujant, valstybiniam mokslinių tyrimų institutui, Fizinių ir technologijų mokslo centrui ir Dublino miesto universitetui (Airijoje) bei Trejybės koledžui Dubline (Airijoje).

Mokslinė vadovė - prof. dr. Rasa Pauliukaite (Fizinių ir technologijos mokslų centras, gamtos mokslai, Chemija - N003)

Moksliniai konsultantai:

- **Dr. Ramūnas Valiokas** (Fizinių ir technologijos mokslų centras, gamtos mokslai, Fizika - N002)
- **Prof. Kim McKelvey** (Dublino universitetas, Airija, gamtos mokslai, Chemija - N003)
- **Prof. dr. Robert Forster** (Dublino miesto universitetas, Airija, gamtos mokslai, Chemija - N003)

Contents

Acknowledgements **8**

List of Abbreviations and Notations **11**

Introduction **14**

1 Literature overview **19**
1.1 Biosensor principle 19
1.1.1 Types of biocomponent and transducer 20
1.1.2 Immunosensors 21
1.1.2.1 Carcinoma antigen 125 as biomarker 21
1.1.2.2 Antibody as bioreceptor for carcinoma antigen 125 23
1.1.3 Surface plasmon resonance for characterisation of antibody-antigen complex 25
1.1.4 Antibody immobilisation techniques 27
1.1.5 Factors affecting antibody loading 27
1.1.6 Self-assembled monolayer 28
1.2 Electrochemical immunosensors 31
1.3 Principles of electrochemistry for biosensing 32
1.3.1 Interfacial double layer in electrochemical biosensors 33
1.3.2 Faradaic and non-faradaic processes 35
1.3.3 Electrochemical cell set up 36
1.3.4 Cyclic voltammetry as transduction method 37
1.3.5 Electrochemical impedance spectroscopy 39
1.3.5.1 Interpretation of electrochemical impedance data 41
1.3.5.2 Modeling of electrode liquid interface 41
1.4 Difference between macro and micro electrodes 43
1.4.1 Design of microelectrodes and microelectrode array . 43
1.4.2 Interdigitated microelectrode array 44
1.4.3 Simulation of electrochemical diffusion 46

1.5 Fabrication techniques of macro-/-micro-electrodes 48
1.5.1 Micro contact printing 48
1.5.2 Wet etching 50
1.5.3 Increasing of electrochemically active surface area by electroplating 50

2 Experimental part **52**
2.1 Materials and solutions 52
2.1.1 Materials and solutions for fabrication and modification of electrodes 52
2.1.2 Materials for immunosensing studies 53
2.1.3 Reagents for electrochemical analysis 53
2.2 Methods for fabrication of interdigitated array electrodes . 53
2.2.1 Design of electrode 53
2.2.2 Fabrication of silica master 53
2.2.3 Fabrication of PDMS stamp 54
2.2.4 Micro contact printing and wet etching 54
2.3 Surface characterisation of interdigitated array electrodes . 55
2.3.1 Optical Microscopy 55
2.3.2 Characterisation of surface by SEM and EDS 55
2.3.3 Electrochemical characterisation 56
2.4 Modification of electrode by Pt and Au nanostructures . . . 57
2.4.1 Several configurations of electrochemical cell 57
2.4.2 Simulation of diffusion on interdigitated array electrodes 57
2.4.3 Electrochemical analysis on miniaturised electrochemical cell 57
2.5 Modification of interdigitated array for detection of carcinoma antigen 125 58
2.5.1 Self assembled monolayer formation on interdigitated array surface 58
2.5.2 Immobilisation of antibody 58
2.5.3 Studies of antibody loading 59
2.5.4 Electrochemical characterisation of sensor fabrication 59

3 Results and discussion **60**
3.1 Characterisation of interdigitated array electrode 60
3.2 Modification of interdigitated array electrodes with Pt coating for H_2O_2 detection 62
3.3 Design and characterisation of the miniaturised electrochemical cell 67
3.3.1 Sealing of interdigitated array 67

3.3.2 Design and configuration of interdigitated electrochemical cell 68
3.4 Simulation of diffusion and comparison with experimental . 71
3.4.1 Simulation Model 71
3.4.2 Comparison of experimental data with simulation . . 72
3.5 Characterisation of Au as pseudoreference and sensing of ferrocene 74
3.6 Sensing of carcinoma antigen 125 using surface plasmon resonanse 77
3.6.1 Investigation of surface coverage by antibody 78
3.6.2 Real time detection of carcinoma antigen 125 79
3.6.3 Specificity to carcinoma antigen 125 79
3.7 Sensing of carcinoma antigen 125 on interdigitated electrodes 79
3.8 Sensing of carcinoma antigen 125 on Au and Pt nano-structured electrodes 86

Conclusions **99**

References **101**

List of Publications and Presentations **120**

Acknowledgements

First of all, I would like to thank my supervisor Prof. Rasa Pauliukaite and Dr Ramūnas Valiokas, head of Nanoengineering Department, for sharing their expertise and knowledge and guidance through my PhD years.

I would also like to thank everyone in the Nanoengineering group, the current members and the formers, particularly Gintare Garbenciute and Tomas Rakickas for their training in microscopy and ellipsometry. For people waiting in the lab before I finish my long hours. To Dr Martynas Gavutis, who made sure all the gold substrates needed arrived on time. Ignas Masiulionis was also in charge of helping design and manufacture PDMS stamps. To Lukas and Romualdas for helping to design connector for IDA electrodes.

To Vytukas for inspiration to use powerful 3D modelling and rendering open-source package Blender. I am great-full for biochemistry and immunology discussions to biochemistry people Airina and Dr Edita. To people from different research groups. To physics, people who always found some time to assist with laser cutting of gold-silica wafers. To Karolis, who gave me training on EDS and Simonas, who made sure that SEM was not destroyed by myself. To Tomas T., who sad LaTeX is the way to go for long documents.

To the administration, whose care kept me going. Thanks, Aneta, Dr Kristina and Dr Aleksandra! For Dr Gintaras Valušis for financial support to gain international experience. I want to thank the doctoral scholarship from the Lithuanian government and The Research Council of Lithuania. I also extend my thanks to the mobility grants given ERASMUS+ and Education Exchanges Support Foundation. Also, to SPIE and OSA for conference grants.

I want to share my thanks to Prof. Robert J. Forster for allowing me to work and learn in the National Centre for Sensor Research during my time at the Dublin City University (DCU), in Ireland. I am very grateful for all necessary training sessions at the Nano Research Facility team. I also would like to express gratitude to all the people from prof. R. J. Forster group. To Dr Column, Dr Bincy and Dr Samantha, who went with me to BEC conference and survived 41 °C in Lyon, France. To Dr Bincy Jose, thanks for being great lab mom! To people who taught me and I had a chance to teach. For visiting students: Lucia T., Lucia M., Amanda, Diego, thanks for a great time in Oviedo. You all became my academic family.

Also, I would like to thank Prof. Kim McKelvey from Trinity College Dublin for introducing me to the world of computational simulation-based

of finite difference method and for the supervision of modelling electrochemical processes on my fabricated interdigitated microelectrode arrays. I thank Prof. Mike Lyons from Trinity College Dublin for introducing me to Kim and useful scientific discussions.

To my former supervisors/professors in University of Vigo, Spain, Prof. Isabel Pastoriza-Santos for an opportunity to learn synthesis of nanoparticles for biosensing applications, to Prof. Elisa Gonzàlez-Romero for my first steps to electrochemistry. My big gratitude to prof. Rimantas Vaišnoras and Dr Loreta Rastenienė, who open the door for my first experience in the lab. To Prof. Vidmantas Gulbinas and Dr Marius Franckevičius, who allowed me to explore the synthesis of nanoparticles. Thank you and other members of the group!

To my extraordinary teachers in chemistry, physics and maths: Lina Šulinskaitė, Daiva Kukienė, Birutė Lėnertaitė; "A teacher takes a hand, opens a mind, and touch a heart (The Big Apple)."

The best friendships I could ever make happened during these years. Thanks, Marta and **B**rigita for crossing California together! Thanks, Dr Jing Zuo for showing me Huangshan Mountain! Dr Ivan, thanks for making me laugh, you always kept my dopamine

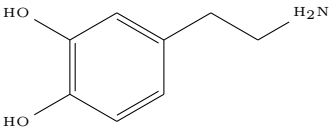

level high! My dear friend Michaella, thank you for a great time during lectures in DCU and caffeine

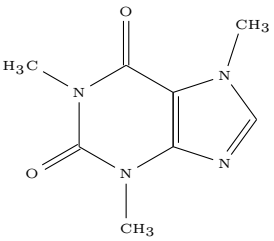

supply! To beautiful people, I have met on the plain during my trips between native Lithuania and Ireland. To my kindness friend Virginytė, I thank God for sending me You! "Eph 3:20: Now to him who can do immeasurably more than all we ask or imagine, according to his power that is at work within us". To grandma, who called me 'golden apple'. To my mother - the strongest women on this planet! To my father, who taught me wood carving... To my beautiful sister Raselė, who miss me badly during my years abroad! To my big brother Edvinas, who was my classmate all these years in school! To my little brother Lukas, "Dreams

do come true, if only we wish hard enough".

For those who loved me and supported and brought joy to my soul! We "Never play anything the same way twice." To those who truly know me! And most of all to my patient spouse Ainis, “Distance is not for the fearful, it’s for the bold. It’s for those who are willing to spend a lot of time alone in exchange for a little time with the one they love. It’s for those who know a good thing when they see it, even if they don’t see it nearly enough. (Meghan Daum)” To Irutė and Arvydas for raising the man of my dreams.

This dissertation was produced using open source software: TEXstudio integrated writing environment for creating LaTeX document and drawing molecules, Python for graphs; Blender and Inkscape for visualisation.

"Nothing but the best is good enough".

List of abbreviations and notations

Acronyms

µCP	Micro contact printing
BSA	Albumin from bovine serum
CA125	Carcinoma antigen 125
CE	Counter electrode
ChA	Chronoamperometry
CV	Cyclic voltammogram
DC	Direct current
EASA	Electrochemicaly active surface area
EDC	1-Ethyl-3-[3-imethylaminopropyl]carbodiimide hydrochloride
EDS	X-Ray spectroscopy
EI	Ellipsometry imaging
EIS	Electrochemical impedance spectroscopy
FcMeOH	Ferrocene methanol
FN	Fibrinogen
HSA	Human serum albumin
IDA	Interdigitated array electrode
IgG	Immunoglobulin G
LOD	Limit of detection
NHS	N-Hydroxysuccinimide
OCP	Open circuit potential
PB	Phosphate buffer
PBS	Phosphate buffer saline
PDMS	Polydimethylsiloxane

PSA	Double-sided pressure sensitive adhesive tape
Rct	Charge transfer resistance
RE	Reference electrode
RT	Room temperature, 20–23.5 °C
SAM	Self assebled monolayer
SEM	Scaning electron microscopy
SPR	Surface plasmon resonance
STDEV	Standard deviation
UV	Ultraviolet
WE	Working electrode

Symbols

Symbol	Description	Unit
E	Potential of an electrode versus a reference	V
E_0	Amplitude of the signal	V
E_t	Potential at time	V
E_f^0	Formal potential of an electrode	V
E_{eq}	Equilibrium potential of an electrode	V
E_p	Peak potential	V
E_{pa}	Anodic peak potential	V
E_{ca}	Catodic peak potential	V
i_{pa}	Anodic peak current	A
i_{pc}	Catodic peak current	A
G	Gibbs free energy	kJmol^{-1}
G^0	Standart Gibbs energy	kJmol^{-1}
ΔG^0	Standard Gibbs free energy change in a chemical process	kJmol^{-1}
ΔG	Gibbs free energy in a chemical process	kJmol^{-1}
$\overline{G}$	Gibbs free energy in electrochemical process	kJmol^{-1}

Introduction

The precision medicine promises increased life quality to humankind; as one aspect, it demands fast and localised sensing. Miniaturisation is a stringent requirement for biosensor transducers in biological and preclinical research and applications in diagnostics. Miniaturised patterns can be an excellent advantage for a low volume sample investigation in liquid samples such as blood plasma, serum, smear, etc.

However, several challenges in biocomponent engineering still need to be faced, where high sensitivity and selectivity for the analyte is required. Also, immobilisation of biorecognition element and selection of surface need to be improved to reduce the percentage of false-positive and false-negative results. In clinical diagnostics, the assay must be fast, reliable and highly reproducible. The surface of the transducer has to be both biocompatible avoiding contamination risk and stable in complex media. For instance, in a blood sample, thousands of biomarkers can be found which might non-specifically bind to the sensing interface. Additionally, cost of biosensor should be lower than the conventional test (e.g. blood test in a hospital). Biosensor should be miniaturised, portable and easy to handle, even in real-time sensing.

Therefore, an establishment of immunosensor for detection of protein biomarkers relies on obtaining appropriate techniques for a fast miniaturised transducer fabrication and surface functionalisation for an incorporation of specific bioreceptor. Such a surface is designed to display a controlled presentation of functional groups, interactions with environmental factors for flexible protein interaction studies.

Gold modified transducers are a common strategy for immobilisation of bioreceptor in biosensing. Gold is widely used as a biocompatible surface in surface plasmon resonance and electrochemical sensors. Unfortunately, the surface patterning for electrochemical sensing and functionalisation for biocomponent immobilisation is still challenging. It is even more complicated in miniaturised sensor platforms based on micro- and nanostructures, where reproducibility of an interface is low.

The aim of this work is to look for reproducible fabrication of interdigitated array electrodes by combining scalable production tools such as soft lithography, wet etching and electroplating for biosensing of carcinoma antigen 125.

Scientific novelty

Scientific novelty of this work is looking for simplification of sensor fabrication for carcinogenic metabolite H_2O_2 and biomarker carcinoma antigen 125 sensing.

1. The work explores combining of soft lithography and wet etching for rapid and simplified interdigitated microarray electrode fabrication and also achieving better sensor performance.

2. We explore unique configuration of electrodes, where interdigitated microarrays are used as working and counter electrodes. Such a configuration can change diffusion of redox active molecules from linear to spherical, which could potentially improve sensing performance.

3. The sensor unique positioning of electrodes were studied by modelling expected electrochemical response using finite difference simulation method.

4. Pt was electroplated at different scan rates controlling structure of Pt and roughness with high precision. This method allows performing the process without toxic agents (lead III), contrary to the established methods.

5. The sensitivity for detection can be tuned by using more in depth data analysis methods for electrochemical impedance spectroscopy such as classical fitting to Randless equivalent circuit or imminence analysis, where components of resistance in impedance $Z^{'}$, $Z^{''}$ vs frequency plots analysed at single frequencies giving faster data analysis.

6. To improve sensing performance flat electrodes were modified by Au or Pt nanostructure and sensing performance for the first time between Au and Pt nanostructures compared. Nanostructured surface is expected to improve antibody loading, also different electroactivity properties between Au and Pt might lead to better values of sensing parameters such as slope and LOD. Fabricated electrodes can be used for electrochemical applications in biosensing.

Statements to defend

1. The fabricated microarray electrodes are highly reproducible with a low standard deviation of 7 %.

2. The interdigitated array electrodes can be modified with Pt coating for H_2O_2 sensing, using electroplating, where roughness of Pt can be reliably controlled by varying number of cycles performing cyclic voltammetry.

3. Electroplated Pt is excellent for a hydrogen peroxide sensing. This approach differs from the conventional galvanostatic plating on Pt itself or chemical synthesis of nanoparticles based approaches.

4. Microarray patterned electrode is an excellent platform for the biomarker carcinoma antigen 125 detection. For comparison, different electrode materials such as nanostructures of gold and platinum have been investigated for biocomponent immobilisation and biomarker sensing.

Research aim and tasks

The goal of this work was to improve the sensor limitations by establishing a new design of microelectrode arrays to obtain rapid manufacturing of miniaturised electrochemical cells for the development of immunosensors and biomarker detection applications. The following tasks were established to achieve the aim:

1. To design and fabricate interdigitated microelectrode array using biocompatible materials (e.g. Au), soft lithography and wet etching techniques and evaluate the quality of electrodes using microscopy images and electrochemistry.

2. To modify interdigitated array electrodes, controlling roughness factor of material (using electroplating) for optimisation of coated layer in sensing of electroactive analyte (e.g. H_2O_2).

3. To design model, including the geometry of fabricated interdigitated electrodes and simulate the diffusion of electroactive species using finite difference method.

4. To design miniaturised electrochemical cell for measurements of low volume (up to 5 µL) of analyte; To evaluate replacement of conventional reference electrode by pseudoreference Au electrode by investigating its electrochemical stability.

5. To calibrate electrochemically active species (FcMeOH) as a proof of concept of interdigitated electrode interface for sensing; Evaluation of dynamic range, linear range, sensitivity, LOD.

6. To incorporate a bioreceptor - antibody using microcontact printing and evaluate antibody coverage by imaging ellipsometry and biosensing of carcinoma antigen 125 real-time binding by using surface plasmon resonance.

7. To transfer immobilisation of bioreceptor (antibody) on interdigitated array electrodes and electrochemical sensing of carcinoma antigen 125 using electrochemical impedance spectroscopy; To evaluate dynamic range, sensitivity and LOD using various sensing parameters including fitting of R_{ct}, and single frequency analysis.

8. To compare carcinoma antigen 125 sensing on higher electrochemical area electrodes by modifying commercial electrodes by Au and Pt nanostructures using electroplating; To investigate electrochemical rate constant changes after anti-CA125 loading; To evaluate dynamic range, sensitivity and LOD using various sensing parameters including the fitting of R_{ct} and single frequency analysis.

The contribution of the thesis author: The author in advice of supervisor and consultants developed all research plans and performed the experimental work including 1) fabrication of the microarray electrodes using microcontact printing, wet etching and electroplating methods; 2) characterisation of the surface using SEM and optical microscopy, imaging ellipsometry and analysed data of measurements; 3) patterning of antibody (anti-CA125) for CA125 on -COOH modified surfaces; 4) investigation of antibody-antigen interaction using SPR ellipsometry; 5) processing and analysis of experimental data and development of two scientific articles related to the thesis; 6) presentation of the results in scientific conferences and seminars.

The contribution of others:

Gintarė Garbenčiūtė assisted in the preparation of bioinert hydrogels for immobilisation of antibodies in surface coverage studies and real-time antigen binding. Dr Martynas Gavutis and Ignas Masiulionis performed PDMS stamp.

1. Literature overview

This chapter represents literature review on immunosensors including their functioning principle and sensing methods as well as sensor fabrication, which covers design of transducers and surface modification to immobilise recognition element.

1.1 Biosensor principle

The first analytical device for the measuring of analyte concentration was reported in 1960 and later (in 1962) described as a biosensor by Clark and Lyons [94].

According to IUPAC in 1996, a biosensor can be defined as an integrated tool in its own right that can provide precise quantitative or semi-quantitative analytical information using a biological recognition element that is in direct spatial contact with the translator element [43]. During the last few decades, platforms of biosensing were of enormous interest in academic and industrial research in the areas such as food safety, environmental monitoring and healthcare [25, 16, 24].

Various sensing systems have been investigated, and sensors developed for helping not only in industry but also in daily life. For instance, temperature sensor, proximity sensor, accelerometer, infra-red sensor, pressure sensor, light sensor, ultrasonic sensor, alcohol and gas sensor are successfully used in daily life. There are various commercialised immunochemistry types of analysis equipment produced by diagnostics companies (e.g. Roche, Siemens, Abbot), which has been used to target molecules in biological samples. However, such instruments have limitations of costly equipment and reagents, so research in biosensing is still of considerable interest.

A diagram of biosensor functioning principle is demonstrated in Fig. 1.1. Two main components are integrated: biological analyte recognition component/receptor (e.g. antibody) and transducer for signalling. Biosensor employs a biological recognition element to capture an analyte and applies transducer to convert this recognition event into a measurable signal [94].

During the interaction of the analyte with the receptor, physicochemical properties on transducer surface change, the difference is registered and converted to a signal through the amplifier. After signal processing, the output is converted and displayed as a quantitative and qualitative response to an analyte in a sample. For instance, a glucose oxidase (used as a biorecognition component in a glucose biosensor) catalyses chemical reaction creating a product which can be detected in an electrochem-

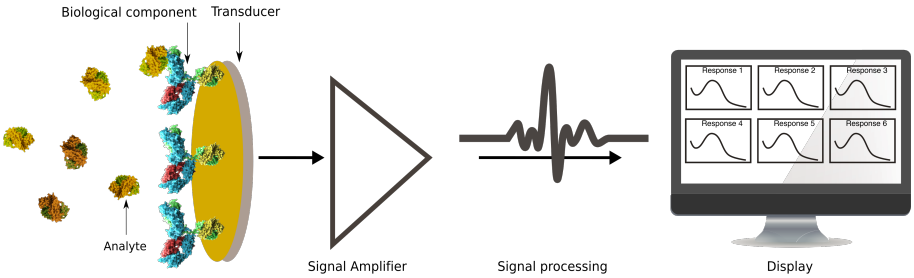

Fig. 1.1. *Diagram of whole assembly of biosensor.*

ical cell. In such a way, various biological analytes as biomarkers can be detected and quantified using selective biocomponents and various transducing elements [108, 6]. However, there are several challenges in the fabrication of biosensors. The sensor needs to be sensitive in physiological concentrations of analyte. Also, high selectivity of bioreceptor to target analyte is required. The sensing has to be fast, reliable and highly reproducible. Finally, the materials used for the fabrication of the device must be biocompatible. Moreover, the cost of biosensor should be lower than a conventional test (e.g. blood test in hospital). For this, biosensor should be miniaturised, portable and easy to handle. For this, non-fouling materials or molecular layers are on a high interest.

1.1.1 Types of biocomponent and transducer

According to the type of the bioreceptor applied for analyte recognition, biosensors can be classified based on specific receptor-analyte interaction, e.g. enzyme-ligand, antibody-antigen, nucleic acids-DNA, cellular structures-cells, or biomimetic materials, for example, scaffold-tethered peptides [123, 10, 9]. The main biocomponents used in sensors are classified based on recognition element used in sensing: antibody, enzyme, cell, tissue, oligonucleotides and aptamers (in Fig. 1.2). For detection of the specific analyte, biocomponent (bioreceptor) is immobilised on a transducer (element for signalling).

The primary examples of transducers are optical (detecting change of light) [32], electronic-based on field-effect transistors (detecting changes in electric field) [142], piezoelectric (gravimetric) [8], pyroelectric (detecting change in temperature) [97] and electrochemical (e.g. detecting potential difference, electrical conductivity, change in charge or steric blocking) [91]. The main types of sensors based on transduction method are summarised below:

- Optical transducers are based on surface plasmon resonance phe-

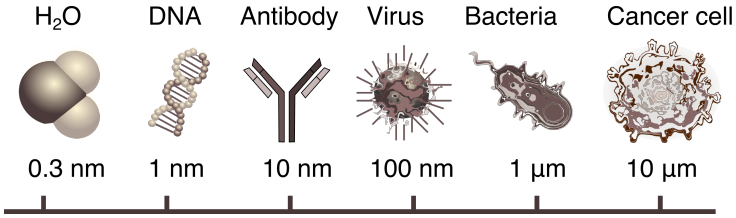

Fig. 1.2. *Diagram demonstrating size of various biocomponents used in sensors comparing to size of H_2O.*

nomena [171] or fibre optics [87], where a change in light absorption or the light intensity is measurable during analyte interaction with biorecognition element.

- Piezoelectric transducers are based on the registration of change in the oscillation frequency of the device representing the concentration of analyte [8].
- Pyroelectric transducers are used to measure a change in temperature during the biochemical reaction [97].
- Potentiometric biosensors use an electric field to control the device. The principle of operation of bio- devices are based on the determination of electrostatic potential changes caused by interaction with analyte [142].
- Electrochemical biosensor as the transducer is an electrode, generating an electrochemical signal that is proportional to the analyte concentration. The signal is caused by steric blocking on the electroactive transducer, change of charge or catalysed reaction [91].

Electrochemical biosensors are very attractive in biointeraction studies resulting in high sensitivity, selectivity and rapid analysis [110, 109, 76, 78]. In this thesis, electrochemical biosensors have been chosen due to advantage of miniaturisation and simplified signal reading systems, which has a high interest for point-of-care diagnostics.

1.1.2 Immunosensors

1.1.2.1 Carcinoma antigen 125 as biomarker

According to the US National Cancer Institute, a biomarker is a biomolecule appearing in blood or other body fluids or tissues reflecting a normal or abnormal process [77]. As biomarkers, specific proteins, e.g. expression of antibodies, antigens, expressed by cells or tissues, might be

detected as a sign of illness. Various biomarkers can be detected helping to diagnose diseases such as diabetes, cardiovascular diseases, neurotic diseases (e.g. Parkinson and Alzheimer) or risk of oncology illness. Detection of biomarkers is beneficial not only in the prediction of decease in the early stage but also in the monitoring of disease where the progress of biomarker expression and efficiency of the treatment can be tracked.

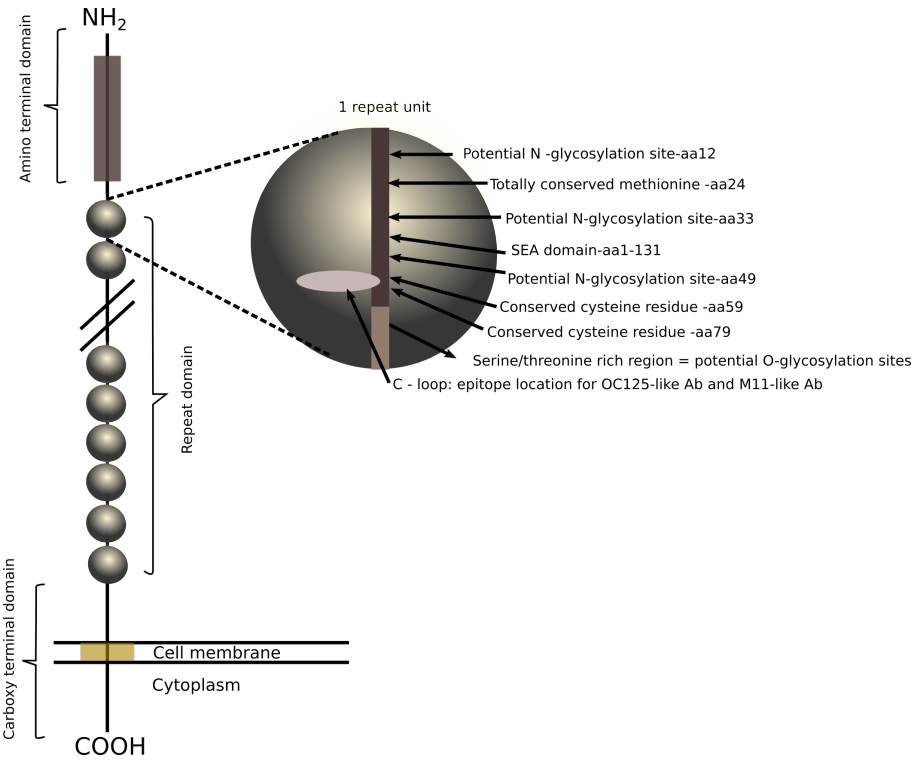

Fig. 1.3. *Schematic diagram of CA125 structure (modified from [159, 128]).*

There are three types of tests in the market based on genetic: molecular, biochemical and chromosomic ones. In the genetic test, the focus is on changes in genes, e.g. breast cancer – BRCA1 gene). To detect differences or mutations within the genome, molecular genetic testing, or gene testing, investigate single genome or short stretches of DNA is used. In the biochemical test, attention is driven to protein over-expression, e.g. biomarkers indicating prostatic cancer - PSA CDK2 or Parkinson's disease – α-synuclein, syntenin, tetraspanin. In chromosome analysis, a procedure that assesses the number and function of an individual's chromosomes to identify abnormalities. Protein over-expression can be detected in various body fluids and tissues e.g. blood [92], urine [81], smear [4], mucus [104] or sweat [151]. Unfortunately, detection of biomarkers is complex, due to

individual unique characteristics, and it requires further investigation.

CA125 is one of the most used biomarker in clinical testing of ovarian cancer. It is a transmembrane glycoprotein with a high molecular weight of 200-1000 kDa [100]. In 80-85 % of women with an ovarian cancer case, the level of CA125 in blood serum is higher, making detection of this biomarker a useful tool for early identification of disease [122, 5]. Monitoring of concentration of CA125 is also critical during the treatment of oncological disease as the level of CA125 should go down during successful therapy. The purpose of early detection is to help provide treatment as early as possible and to increase the possibility of a successful treatment [74]. Usually, after the detection of higher expression of CA125 produced in cells, additional tests (e.g. ultrasound scan) in hospital are performed helping to diagnose the disease as early as possible. It should be noted, that an increased level of CA125 can also be useful for detecting other diseases such as endometriosis, uterine fibroids, cirrhosis, peritonitis, pericarditis or pelvic inflammatory disease [125]. Also, raised CA125 level can be caused by other of non-disease conditions in the body such as menstruation or pregnancy, giving false-positive results [68].

Reducing the risk of cancer through prevention, early diagnostics and better monitoring after treatment is promising a better quality of life. As it has been reported in National Health Service in the UK, CA125 physiological levels considered normal (the cutoff point) is 35 UmL^{-1}. The levels above can be considered as a higher probability of disease.

For instance, for endometriosis, a negative predictive value was 78 % for the cutoff CA125 value of 20 UmL^{-1}, whereas positive predictive value was 93 % at the cutoff value of 30 UmL^{-1} [74]. According to previous studies, the predictive value of CA125 level higher than 35 UmL^{-1} was of 60 % for ovarian cancer. The current methods for CA125 detection are enzyme-linked immunosorbent assay (ELISA), sandwich immunoassay and fluoroimmunoassay. Unfortunately, these techniques usually are time-consuming, cost-inefficient and require high-level technical staff [174, 29]. Here, electrochemical immunosensor could be more promising because of the simplicity of measurement and potentially higher sensitivity.

1.1.2.2 Antibody as bioreceptor for carcinoma antigen 125

For specific detection of biomarkers, receptors are required. Antibodies are biopolymers of approximately 150 kDa molecular mass used as bioreceptor in sensing systems. Immunoglobulin G (IgG) is the most common class of glycoproteins used in biosensing with a structure of four polypepchains: a pair of heavy chains (H) of about 50 kDa and a pair of the light chains (L) of about 25 kDa [90, 160] and molecular dimension

of 14.5 x 8.5 x 4 nm^3 [135].

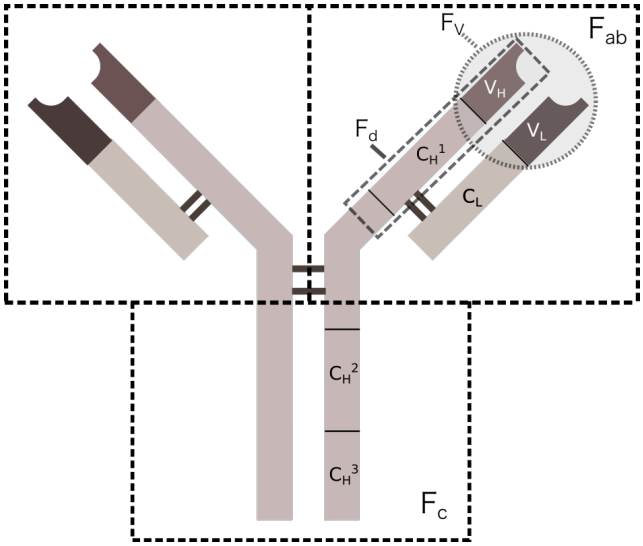

Fig. 1.4. *Schematic diagram of an antibody and its fragments. The F_c fragment contains the antibody effector functions, such as complement activation, cell membrane receptor interaction and transplacental transfer. The F_{ab} fragment consists of the heavy - H, light - L and variable - V chains (V_H and V_L) and the constant (C_H^1 and C_L) chains [90]. F_V fragment contains the V_H and V_L chains and the F_d fragment consist of the V_H and C_H^1 chains [90].*

The heavy chain of an antibody consists of one variable region and three constant regions represented as C_H^1, C_H^2 and C_H^3 as shown in (Fig. 1.4). The light chain consists of a constant and a variable region: C_L and V_L, respectively. A disulfide bond constrains the two heavy chains to one another and to a light chain [90]. Antibody consists of two identical regions F_{ab} (Fig. 1.4) with antigen-binding sites positioned at N-terminal of each domain and one F_c region for antibody immobilisation [120]. IgG antibody has carbohydrate (CH_2) located at the F_c domain of the two heavy chains. The flexibility of the hinge region (an area where the two F_{ab} fragments meet) allows extension of the distance between the binding sites leading to the higher efficiency of antigen-binding.

Since its first discovery in 1981, numerous antibodies (bioreceptor) against CA125 were made. These antibodies are classified as OC125, M11, or OV197 with respect to a recognized antigenic determinant. CA125 was defined by monoclonal mouse antibody, OC125, which was obtained by Bast from the ovarian cell line OVCA 433 as an immunogen [103]. Antibodies similar to OC125 and M11 are proposed to detect an enclosed

cysteine loop (C-loop in Fig. 1.3) structure in the repeat unit [159]. Several studies have carried out a comprehensive analysis of various classes of antibodies against the CA125 epitopes isolated from normal abdominal fluid, cervical mucus, cell culture or ascites [159].

In the literature, various different molar weights of CA125 were reported. Mass greater than 1000 kDa, as well as proteins with a lower molecular weight of 200-400 kDa, 130 kDa, 205 kDa and 55 kDa were observed depending on the raw material analysed [159]. Numerous of these studies have also identified a modular CA125 structure that can be decomposed into species of 200 kDa, 70 kDa and 50 kDa. These forms of CA125 have been termed splice variants resulting in amino acid sequences with molecular weights of 49 to 1500 kDa [159].

For compatibility requirement of the bio-assay principle with the transducer, immobilisation of antibody onto transducer in many biotechnological applications is critical [71, 83].

1.1.3 Surface plasmon resonance for characterisation of antibody-antigen complex

The term 'active antibodies' refers to the immobilised antibodies on the surface that can capture antigen from solution. It has been reported that the required number of well-orientated antibody molecules on the surface has to be >40 times higher than the captured antigen [126]. The binding of an antigen to a captured antibody can be described using a standard ligand-receptor model (1.1), where A is the antigen and B is the immobilised capture antibody-forming immunocomplex - AB.

$$A_{(aq)} + B_{(s)} \longleftrightarrow AB \tag{1.1}$$

Several interactions between an antibody and antigen-binding happen including Van der Waals forces, electrostatic bonds, and attractive hydrophobic forces due to the close positioning of non-hydrophilic parts of the two molecules. None of these interactions are covalent, and this makes the antigen-antibody conjugation a reversible reaction. Mostly, the antigen-antibody complex could be reassembled by chemical, electrical or thermal denaturation. Rate of antigen binding to antibody depends on several factors including size of antigen, temperature, flow rate and density of antibodies, the surface density of immobilised capture probe, the fluid velocity, diffusion of analyte and quality of antibodies [93]. Real-time antigen-antibody interactions can be studied using optical methods. The most common is the surface plasmon resonance phenomenon, where binding-rebinding of antibody-antigen is measured as a change in the reflective index.

Surface plasmon resonance (SPR) as a detection tool has been reported including real-time analysis of cells [139] and bacteria [66], DNA and protein [160, 28]. The configuration of an SPR sensor (shown in Fig. 1.5) consists of a prism and glass coated with a thin metallic layer (e.g. gold), on which bioreceptor is immobilized for analyte sensing through the change of intensity of SPR.

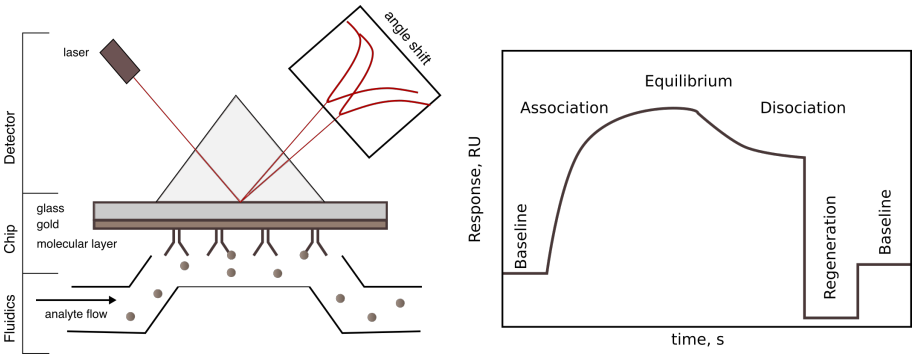

Fig. 1.5. *SPR working theory scheme (on the left), where light is beamed through a prism onto a metal film, and the reflected beam goes to the detector. The intensity profile of the reflected beam exhibits a dip or minimal intensity at the resonance angle. SPR measures the shift of position (angle shift) during molecular adsorption, and this shift represents the adsorption kinetics plotted against time (right) and shows response changes before and after analyte injection, association, equilibrium, dissociation, and sensor regeneration.*

During the measurement, the laser beam (in Fig. 1.5 on the left) goes through a prism and the reflected beam from the gold surface is collected by a digital imaging device (such as CCD camera). SPR provides real-time, label-free detection of binding kinetics by monitoring reflectance as a function of time (in Fig. 1.5 on the right) , which gives us information about a protein and its affinity to a ligand (in Fig. 1.5).

Measuring different concentrations of antigen allows us to determine the association rate constant - k_a and dissociation rate constant - k_d (mol/s) providing information about equilibrium dissociation constant $K_D = k_a/k_d$ (mol) [99].

Such studies of antibody-antigen can provide information about incubation time required for the reaction, and this can be transferred to a more simplified static systems as well as applied in miniaturised biosensors. Also, factors such as antibody loading and efficiency need to be studied prior to fabrication of a miniaturised immunosensor.

1.1.4 Antibody immobilisation techniques

The main types of immobilisation of antibodies on transducer are physical entrapment, covalent cross-linking and affinity-based immobilisation [84]. The physical adsorption of antibodies onto solid immunoassay supports offers straightforward immobilisation via electrostatic and hydrophobic interactions [46]. Since physical adsorption of antibodies has mild conditions for protein immobilisation, it is a popular method for fabrication of immunosensors. Adsorption on insoluble matrices can be investigated by intermolecular forces such as van der Waals force and hydrophobic ones as well as ionic bonding, hydrogen bonding interactions or their combination [131, 73].

Covalent immobilisation of antibody could be more attractive because immobilised antibody, after antigen binding, can be regenerated several times (using 2 M NaCl or glycerol) [61, 106].

Usually, the transducer is modified with a molecular layer consisting of -COOH and -NH_2 or -SH groups allowing chemical crosslinking to functionalised molecules assembled on a surface. Cross-reactants (or crosslinkers) are molecules having two or more reactive ends (e.g. NHS/EDC, glutaraldehyde) capable of chemically linking between two specific functional groups on transducer surface and antibody (primary amines, sulfhydryls, etc.) forming irreversible linkage [73]. Different molecular films can be used to form functional groups for covalent crosslinking of antibodies, including self-assembled monolayers (e.g. gold alkanethiols). Here, it is essential to have a clean, smooth surface of an electrode to obtain homogeneous SAMs for highly controlled biocomponent immobilisation. Unfortunately, the covalent coupling is a time-consuming and complicated chemical reaction, where toxic reagents are often used. Additionally, the activity of proteins is reduced by forming linkage on active protein sites [73]. Also, it is challenging to control the crosslinking reaction, and this method requires a high concentration of proteins. These factors have to be considered before building immunosensor.

Many proteins such as protein G [138], protein A [84] or recombinant protein A/G have been documented as immobilisation technique for affinity to the necessary antibody concentration and safe operation. These factors have to be considered before building immunosensor.

1.1.5 Factors affecting antibody loading

The surface density of the immobilised antibodies can strongly influence immunosensor sensitivity and long term stability [120]. Depending on the electrode surface, the number of immobilised antibodies varies, giving influence to sensor properties. For higher antibody loading, vari-

ous structures such as nanoparticles, polymeric, metal nanowires were explored [113, 160, 40].

For well-packed antibodies, the total surface coverage reaches values of 8.1 - 150 ngcm^{-2} [173]. Total coverage of antibody has been reported as 51 $\times$ 10^2 antibodies per nanoparticle (64 $\times$ 10^{10} cm^{-2}) [126]. The amount of active antibodies is around 4 - 5 % in a formed monolayer on a surface[126].

If the packing of antibodies is increased to well-packed assembly, the antibody activity can drop down to 0.6 %. Loss of antibody activity can be caused by its random orientation, denaturation and reduced steric availability. Immobilisation density depends on protein size, concentration and physicochemical surface properties. If the immobilisation density is too high, active sites could be sterically blocked, leading to 'crowding effect' or overloading of the antibodies [126].

1.1.6 Self-assembled monolayer

Biorecognition element (e.g. antibody) can be immobilised on various solid surfaces by the formation of linkages, e.g. SAM, involving alkaline, carbodiimide, amide, or maleimide [70, 18]. However, the electrode surface for SAM formation needs to be clean and relatively flat to keep monolayer homogeneous and functional SAM groups well orientated [145]. SAM were used for antibody immobilisation on various surfaces in immunosensors.

For instance, oligo(ethylene glycol) (OEG) SAMs are highly biocompatible and are widely applicable as low-fouling surface for detection in real sample (e.g. serum, plasma) [17, 96, 152, 118, 153, 154].

SAM are organic molecules, assemblies formed spontaneously on surfaces by adsorption organising large ordered domains. Hydrophilicity and hydrophobicity, chemical resistance, biocompatibility, molecular recognition for micro-/-nanofabrication and biosensors can be manipulated simply by changing the functional group surface. SAMs are cost-efficient surface coatings having extensive control of surface properties [89].

In electrode fabrication, it is used to protect the metal surface from an aggressive environment and etching process. Anti-fouling SAM coating can be formed on a gold substrate even from the short-chain structure of –(O-CH_2-CH_2)$_m$–, where m is the length of chain. Understanding of SAM phenomena started in 1773 when Benjamin Franklin placed a small amount of oil onto a lake, and he realised that the waves over a considerable distance became calm. Oil formed a film on top of the water of about one molecule thickness as was experimentally confirmed later by Lord Rayleigh. A very first scientific paper based on area control of oils

films published in 1891 by Agnes, Pockels gave an impact for opening a new field in surface science [111].

When a small amount of insoluble liquid is placed on another, it spreads out across the surface. For instance, amphiphile molecules (having hydrophilic and hydrophobic ends) would stand on the water orientated with the hydrophilic end next to the water and hydrophobic out of the water as demonstrated in Fig. 1.6. After dipping substrate in such a liquid with a monolayer of molecules, the molecules can be transferred onto a surface forming physically adsorbed monolayer called Langmuir-Blodgett (LB) film [19]. In such a way, several numbers of layers can be created merely repeating dip in and out process [19].

Unfortunately, it is challenging to fabricate such a film, because formed layer can be not homogeneous or randomly orientated depending on the substrate surface or prepared solution. Also, physical adsorption is not stable enough and can be damaged easily.

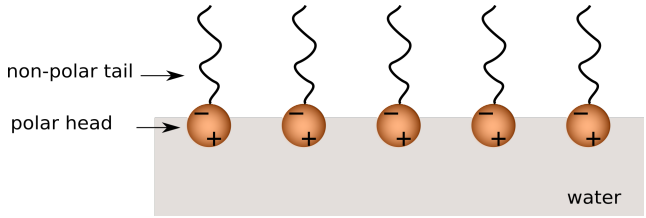

Fig. 1.6. *Scheme of amphiphile molecules arrangement on water surface.*

The SAM films can be generated on solid substrates such as Au, Ag, Cu, Pt, Ge, Si, SiO_2, GaAs can be used for SAM formation [50, 79]. The main difference between LB and SAM films is that in SAM the head of the molecule is chemically adsorbed on the surface, making the bond stronger. SAM formation is a straightforward process. Usually, monolayer film can be formed immersing the clean substrate in a prepared solution of target molecules and incubating for some time by letting molecular units naturally to assemble and pack on the surface due to low surface energy, i.e. by chemical adsorption [79].

Depending on the application of SAM, for binding of molecules to different substrate surface various functional groups can be involved including -SH, -OH, -COOH, $-NH_2$, $-CH_3$ [50]. For SAM formation on a gold surface, mostly, alkanethiols molecules constructed of an alkyl chain, $-(C\text{-}C)^n$ - the backbone, a tail group and -SH group are used. The SH-Au bond has an energy of 44 kcal/mol.

For a high-quality SAM formation to have a clean gold surface is critical. So, gold needs to be freshly sputtered or electroplated, or cleaned

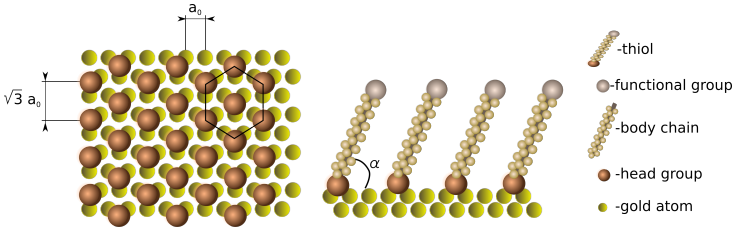

Fig. 1.7. *Scheme of thiols forming SAM structure.*

in a proper way before immersing it into thiol solution in order to form a high-quality SAM.

$$CH_3(CH_2)nSH + Au_m \rightarrow CH_3(CH_2)nSH^-(Au_3^+)Au_{m-3} + 1/2H_2 \quad (1.2)$$

The reaction of alkanethiol with the gold surface is demonstrated in 1.2 [79]. Alkanethiol binds to the thermal S atom in a pit between a triplet of Au atoms as shown in Fig. 1.7.

Alkanethiol pack at 1/6 available sites forming a hexagonal closest packed (HCP) layer with the spacing of $\sqrt{3}a_0$, where $a_0 = 2.88$ $\AA$ is the distance between gold atoms as demonstrated in 1.2 [79]. Van Der Waals bonds form between the chains with a strength of 1.75 kcal/mol [79]. The thiol chain spacing is wider than the distance required to have maximised van Der Waals interactions between the chains. To maximise molecular interactions between carbon chains a natural tilt around 30^o is being developed [79]. The chain length can be controlled during the synthesis of alkanethiol, where more alkane groups can be attached to control the thickness of SAM [79]. The longer the alkane chain, the higher van Der Waals force between molecules leading to well-packed SAM on gold surface. The top functional group on the surface describe SAM surface physical and chemical properties. For instance, surface hydrophilicity and/or hydrophobicity can be controlled choosing -NH_2, -COOH, -CH_3, -$(OEG)_n$, -OH, functional groups [89].

Unfortunately, the formation of SAM on other surfaces such as glass, silica or carbon materials is complicated and requires to look for different surface chemistry approaches. Polymers such a Nafion [60, 2], polyvinylpyrrolidone (PVP) [34], quinone-amine (QAP) [149], carbosilane [69], poly(vinyl chloride) (PVC) [53] have been also investigated in order to stabilise nanoparticles on electrode. For instance, Nafion has -SO^3 ionic group and on another side polytetrafluoroethylene (PTFE) giving non-fouling (highly electronegative) surface properties. In comparison, poly(phenylenediamine) (PoPD) film provides an interface and even has more active free amino groups for the conjugation of noble metal

nanostructures to construct biosensors of high stability [172, 75, 150, 156]. PoPD as one of the aniline derivatives and the aromatic diamine is widely used as a binding polymer due to its electrical, mechanical, and thermal properties [52, 27]. Moreover, positively charged surface, homogeneity, and firm adhesion of electropolymerised films on electrode surface have made PoPD very attractive for application in biosensors [42, 161, 124, 45]. Additionally, PoPD can be used to improve selectivity and avoid electrode contamination [165].

1.2 Electrochemical immunosensors

In the case of electrochemical immunosensors, the formation of the antigen-antibody complex is converted into an electrical signal: current (amperometric immunosensors), a voltage difference (potentiometric immunosensors), or a resistivity change (impedimetric immunosensors). According to the biological recognition process, electrochemical immunosensors can be classified into two main categories: biocatalytic [112, 117, 73] and affinity sensors [93, 51, 69].

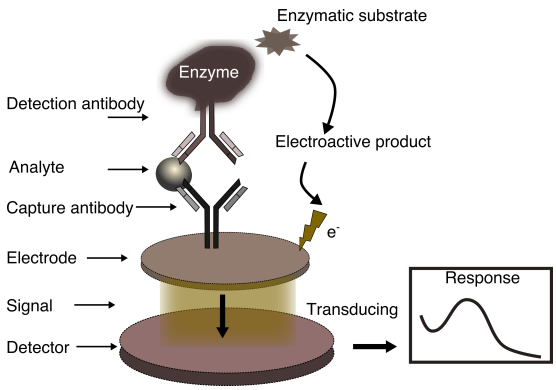

Fig. 1.8. *Analytical principle of electrochemical immunosensor.*

Usually, in biocatalytic immunosensor enzymes are used as a label to biorecognition element (antibody) to a target analyte (Fig. 1.8). Changes in the electrical signal from antibody conjugated with electroactive label binding to the antigen are detected in electrochemical cell [132]. For electrochemical signal amplification, peroxidase, alkaline phosphatase, glucose oxidase, β-galactosidase, and lysozyme have been employed to label antibodies and antigens [3].

Affinity sensors are based on direct recognition of biomolecules, without electroactive species involved. For instance, antibody-analyte produce charge, mass or steric changes in the electrical signal, which is detected

in electrochemical cell [133].

Depending on the electrochemical process registered after antibody-antigen interaction in electrochemical cell, biosensors can be classified to amperometric [105], voltammetric [86], potentiometric [142] and impedimetric biosensors [129]. In this thesis, electrochemical impedance spectroscopy has been used for studies of the antibody-antigen complex.

The immunosensors have been studied for a variety of uses, including bioprocess control, food quality and agriculture, military and medical. Currently, some research groups are working on environmental monitoring biosensors (Bahadir and Sezginturk, 2015; Verma and Bhardwaj, 2015). However, in the clinical analysis, the establishment of acceptable levels of new contaminants such as pesticides, phenols, hormones and antibiotics, as well as drugs, protein and hormone levels, requires the development of fast and reliable methods to detect concentrations of pM levels (Belkhamssa et al., 2016).

Unfortunately, there are still no electrochemical immunosensors to diagnose diseases in hospitals or medical centres. Specific reasons could include sophisticated automation of such devices, advanced equipment needed for multi-analysis, and long-term stability of sensor elements. However, a broad scientific community is seeking to develop analytical, diagnostic methods and these issues will be resolved sooner.

On the one hand, multilateral detection and synchronisation analysis with multichannel electrochemical devices already were carried out, proving the usefulness of medical institutions with many applications. On the other hand, this technology allows the production of cheap care products that can be used by patients, for example, glucose sensors, commonly used by diabetics. To this end, great attention was paid to the immune sensors as they combine the specificity of the specific immunoreactivity with the very high sensitivity of different detectors. According to electrochemical sensing principle, immunosensors can be categorised to: amperometric, potentiometric, voltammetric, conductometric and impedimetric.

1.3 Principles of electrochemistry for biosensing

As transducer should be capable of converting the biorecognition event into a measurable signal, it is vital to understand fundamental processes happening on an interface. Electrochemistry is the branch of physical chemistry, where the relationship of chemical changes is expressed as an electrical signal (e.g. potential, charge or current). Electrochemical reactions take place at the electrolyte-electrode interface. The electrode surface forms a junction between the solution and electrode [13].

1.3.1 Interfacial double layer in electrochemical biosensors

When an electrode is brought in contact with an electrolyte, the layer of charged ions on the electrode are formed and oppositely charged ions from solution form another layer, which appears as a structure called double layer (Fig. 1.9) [13]. The statement that the structure of the double layer and specific adsorption of ions can affect the kinetics of electrode reactions was recognised in 1933. Such effects can cause a variety of problems in biosensing. For instance, the rate constant k° of electrochemical reaction might be a function of the supporting electrolyte concentration even when no binding event of antigen to antibody occurs, or nonspecific adsorption of ions from the electrolyte is present. A German physicist, Hermann von Helmholtz in 1853 demonstrated that an electrical double layer behaves as molecular dielectric and stores charge electrostatically, and the behaviour of the electrode-solution interface is linked to a capacitor. The stored charge density can be modelled as a constant differential capacitance depending on the dielectric constant of the pH of electrolyte, concentration and electrode material and geometrical area of the electrode. The store charge density is called capacitance and described by equation (1.3).

$$C = \varepsilon\varepsilon_0 \frac{A}{d} \tag{1.3}$$

Where, A - the area of electrode, d - the distance between two charged layers, ε - the dielectric constant of solution, ε_0 - the dielectric constant of vacuum.

It is vital to understand the concept of electrical double layer for a description of the interfacial processes. The Debye length characterises the extent of the active sensing distance. In most of the physiological fluids its lower than 1 nm. Variation of k_0 can be understood in terms of the variation of potential in double-layer region [13].

Also, a small molecule carrying no charge or a small charge has a little impact on changes in the electrochemical system unless changes were happening close to the Debye length or effect electrode potential [101]. Debye length (at 25 °C) depends on ionic strength (concentration) of electrolyte. For instance, Debye length for 1 mM is 10 nm, for 10 mM - 3 nm, for 100 mM and for 1 M - 0.3 nm as shown in Table. 1.1.

In physiological concentrations, the bound antigen to antibody is in a higher distance from transducer, outside of the Debye length or electrochemical double layer due its size. So, electrical charge from antigen is

Table. 1.1. *Thickness of the Debye length [13].*

C, M	κ^{-1}, nm
1	0.30
0.1	0.96
0.01	3.04
0.001	9.62
0.0001	30.4

difficult to measure.

$$\kappa^{-1} = \sqrt{\frac{\varepsilon_r \varepsilon_0 k_B T}{2 \times 10^3 N_A e^2 I}} \tag{1.4}$$

Debye period is calculated in the way shown in Eq 1.4, where I is the electrolyte ionic strength (M or mol/L), ε_0 is the permittivity of free space, ε_r is the dielectric constant, k_B is the Boltzmann constant, T is the absolute temperature in kelvins, N_A is the Avogadro number. e is the elementary charge [13].

In electrolyte, the Debye length is a measure of the net charge electrostatic effect in solution and the extent to which its electrostatic force remains. Debye length is an essential parameter in electrolyte providing information about the sensitivity of the electrochemical system [13]. The electrical double layer can be modelled as consisted of two parallel sublayers. The nearest sublayer to the electrode is called the inner Helmholtz layer, which is connected to the surface charge (positive or negative), consisting of ions adsorbed to the material due to chemical interactions.The second layer, called the diffuse layer, is composed of ions that are attracted by Coulomb force to the surface charge, filtering the first layer electrically. The diffusion layer is weakly associated with the electrode [13]. It has consisted of free ions that move in the solution under the influence of electric attraction. In "Gouy-Chapman model" the charge distribution of ions decreases linearly in the Helmholtz layer and exponentially starting from the diffusion layer [13]. Unfortunately, essential factors including the diffusion/mixing of ions in solution, the probability of surface adsorption and the communication through solution dipole moments and the electrode are not considered, and this involves more model refinement for specific systems [13].

Measurement of the double-layer capacitance provides information on adsorption and desorption processes as well as on the structure of modified electrodes, which is very important for the application of the immune sensor. The charge transfer and properties of an electrical double layer

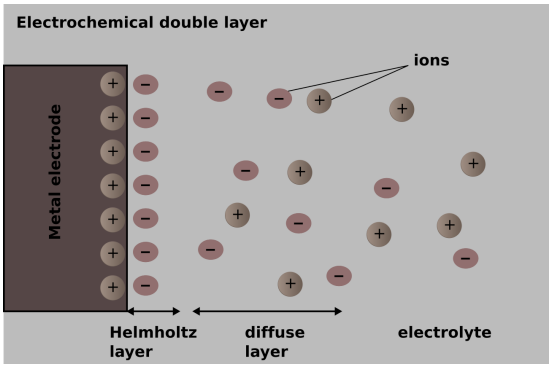

Fig. 1.9. *Diagram of electrochemical double layer, demonstrating Helmholz layer, diffusion layer appearing after immersion of electrode in electrolyte solution.*

can be studied in the electrochemical cell using voltammetric and impedimetric methods.

1.3.2 Faradaic and non-faradaic processes

Two types of electrochemical methods: faradaic and non-faradaic at the electrode/electrolyte interface occurs. The faradaic process involves the electron charge transfer (1.5) from redox active solution, and the non-faradaic process is measured out of redox activity window [13]. Electrochemical reaction of redox molecules is driven by two main processes on electrode: oxidation (Ox) and reduction (Re) (1.5)[13].

$$\mathrm{Ox(aq)} + \mathrm{ne^-} \rightleftarrows \mathrm{Re(aq)} \tag{1.5}$$

The total electrochemical potential - μ (1.6) consist of both chemical (μ_j) and electrical ($Z_j F\phi$) potentials appearing during interaction between redox active molecules and electrode [13].

If μ_j 0 at [Ox]/[Red]= 1, chemical potential of species is added.

$$\mu = \mu_j + Z_j F\phi \tag{1.6}$$

where Z_j - the charge of molecule j, F - the Faraday constant (the charge on one mole of electrons- 96,487.0 C) and ϕ - the potential of phase (electrode or solution)[13].

Chemical potential depends on the ratio between the concentration of oxidised and reduced species, as shown in 1.7 [13].

$$\mu_j = \mu_j^0 + RTln(\left(\frac{[\mathrm{C_{Ox}}]}{[\mathrm{C_{Re}}]}\right) \tag{1.7}$$

Electrical potential is discribed as potential difference between two phases: metal electrode (ϕ_M) and solution (ϕ_S) phase. The difference is expressed as a potential different of oxidised (μ_{Ox}) and reduced (μ_{Re}) species 1.8 [13].

$$F(\phi_M - \phi_S) = \mu_{e^-} + (\mu_{Re} - \mu_{Ox}) \tag{1.8}$$

Combining 1.7 and 1.8 the famous Nerst equation is obtained, which relates an electrochemical cell potential to the concentration of electroactive species in the cell can be written [13]:

$$\phi_M - \phi_S = \frac{\Delta\mu^0}{F} + \frac{RT}{F} ln \left(\frac{[\mathrm{C_{Ox}}]}{[\mathrm{C_{Re}}]} \right) \tag{1.9}$$

However, it is impossible to measure the absolute value of $\phi_M - \phi_S$ in a single electrode-solution interface.

Later it was proved that the mass transport of molecules penetrating electrode area is a time-dependent function forming a flux [13]. The flux is dependent on several factors, including diffusion coefficient, concentration gradient, potential gradient, and charge of the analyte.

However, the Cottrell equation should be used according to experimental and instrumental constraints.

$$i(t) = \frac{nFAD^{1/2}C_{Ox}}{\pi^{1/2}} \tag{1.10}$$

When diffusion, convection and migration all take place at the same time, the mass-transport process is very complicated, making it difficult to study the relationship between current and analyte concentration.

In the case of a planar electrode, convection can be eliminated by using an unstirred solution, and migration can be reduced by adding a high concentration of support electrolyte to reduce the electric charge field [13]. If the reaction rate is limited only by diffusion, the ratio between current and analyte concentration would be described by the Cottrell equation (1.10).

1.3.3 Electrochemical cell set up

A conventional electrochemical cell consists of three electrodes: working (WE), auxiliary/counter (CE) and reference (RE) are immersed in electrolyte solution [58]. The WE on which electrochemical reactions occur is placed close to the CE (e.g. Pt wire), which has a role of passing the same current as generated on working electrode preventing WE electrode from damage. If the WE has small dimensions of microsize and current flow is low, the elimination of the CE can be considered.

For measurement electrochemical reactions on the WE electrode, the availability of a stable, well-known potential reference electrode (e.g. Ag/AgCl, SHE, RHE) is important in order to maintain stable applied potential during the measurement.

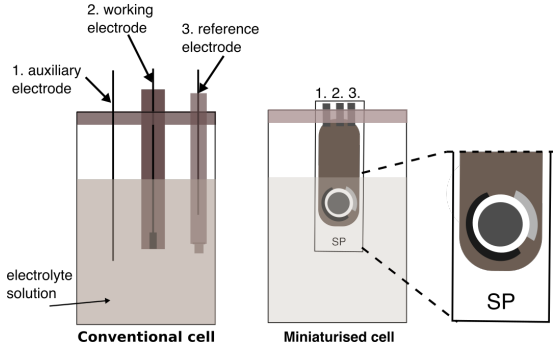

Fig. 1.10. *Diagram of electrochemical cell consist of three electrodes: WE, RE and RE in conventional (on the left) and miniaturised for screen printed (SP) electrodes (on the right) systems.*

Two types of electrochemical cells: conventional and miniaturised are demonstrated in Fig. 1.10. In electrochemical systems, it is imperative to have a stable interface, where the distance between electrodes, the concentration of electrolyte has to be fixed. However, the final design of cell needs to be understood, prioress designing miniaturised electrochemical cells and depending on the application such a requirement might be passed.

1.3.4 Cyclic voltammetry as transduction method

Cyclic voltammetry is one of the most common electrochemical methods for analytical studies, providing information on redox potential and kinetics of the heterogeneous electron transfer [13]. CV is described as an electrochemical technique which measures the current that develops in an electrochemical cell, where linear increase (from E_1 to E_2) and decrease voltage is applied over time as demonstrated in Fig. 1.11. As CV is reversal technique, the time corresponding to E_2 is switching time, where potential scan starts to change direction back to lower (E_1).

During the change of potential from E_1 to E_2 would oxidise redox molecules, and the reverse scan reduces the analyte from oxidised form to reduced form accordingly [13]. The current at the beginning of a scan is the charging current caused by the electrical double layer at the electrode surface- capacitive current, and the current response (peak current) related to the concentration of the redox-active molecules is called faradaic

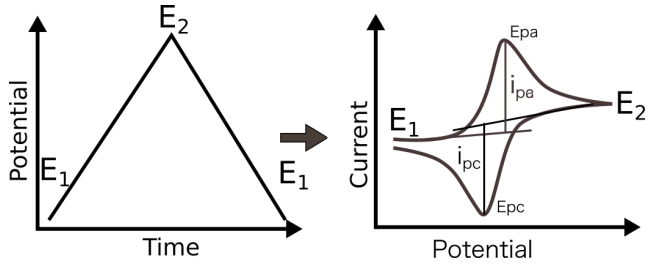

Fig. 1.11. *Experimental setup for cyclic voltametry. The potential waveform applied as a function of time to the working electrode, output is a current reflecting oxidation and reduction process in a typical CV process.*

current. When the potential increase from E_1 to E_2, a current corresponds to oxidation peak potential (E_{pa}), where i_{pa} is observed due to the loss of an electron from the reduced form of an analyte when the potential is reversed from a higher value E_2 to lower E_1, a peak current (i_{pc}) would be observed corresponding to the reduction peak potential (E_{pc})[13].

Potential of redox-active molecules can be described by the Nernst equation, where two reactions: oxidation and reduction can be described as in 1.11.

$$E = E^{\circ} + \frac{0.059}{n} \log \frac{C_{ox}}{C_{re}} \tag{1.11}$$

where: n - number of transmitted electrons in reaction, C_{ox} - concentration of oxidized, C_{re}- concentration of reduced.

Electron transfer happens when a potential difference is added to the electrode, converting active electrochemical molecules at the surface into reduced electrochemical active molecules. Concentrations of reduced and oxidises molecules at the electrode surface vary as a function of the potential E applied to the electrode[31].

If a redox system remains in equilibrium i_{pc}/i_{pa}=1 throughout the potential scan, the redox process is described as reversible. Otherwise is called quasi reversible or irreversible [13].

The characterisation of reaction provides information about the electrochemical system and processes happening on the electrode. For instance, the distance between E_{pc} and E_{pa} can tell us how fast is the electron charge transfer as after analyte binding to the electrode we could expect such a change. Mostly, the increase in peak to peak separation in CV is caused by the blocking of the electrode, creating resistance in the system. Such strength can be correlated to the blockage of the electrode and even calibrated depending on how many molecules are on the

electrode.

1.3.5 Electrochemical impedance spectroscopy

Electrochemical impedance spectroscopy (EIS) became a powerful tool for novel impedimetric biosensors providing information of surface properties. EIS has been used as a tool for thin film characterisation in SAM formation [155], electroplating [167], ion diffusion [63] studies and investigation of semiconductors [62]. In EIS, a small oscillating voltage (5-10 mV) is applied, and as a response to this potential, the current signal is recorded as demonstrated in Fig. 1.12. The ratio of potential and current gives the value of impedance at every single frequency applied to the system [13].

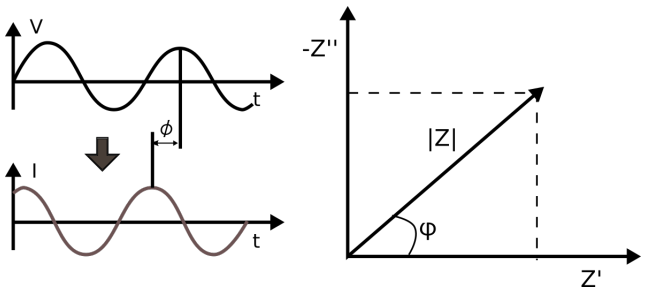

Fig. 1.12. *Impedance setup for measurement. Applied oscillating voltage (V) and current response (I) at a single frequency. The response for single frequency is visualised as the real (Z') and imaginary (Z") part giving a module of |Z| with a phase angle ψ.*

The applied potential has the form as in 1.12 [21]:

$$E_t = E_0 sin(\omega t) \tag{1.12}$$

Where Et is potential at time t, E_0 is the amplitude of the potential and ω- radial frequency ($\omega = 2\pi f$)[13].

The response signal of I_t is recorded, which has different amplitude (I_0) and a shift in phase (ϕ):

$$I_t = I_0 sin(\omega t + \phi) \tag{1.13}$$

The ratio of input and output signals gives the value of the system called impedance (Z) 1.14, where Z_0 is magnitude [13].

$$Z = \frac{E_t}{I_t} = \frac{E_0 sin(\omega t)}{I_0 sin(\omega t + \phi)} = Z_0 \frac{sin(\omega t)}{sin(\omega t + \phi)} \tag{1.14}$$

After plotting Et on the X - axis of a graph and It signal on the Y - axis, the parametric equation result would be an oval (Lissajous-Bowditch curve) and impedance can be analysed as a complex number 1.15:

$$Z = Z^{'} + jZ_{im} \tag{1.15}$$

where $Z^{'}$ is real impedance independent of frequency ($\phi = 0$) and $Z^{'}$ is imaginary impedance dependent on frequency ($\phi \neq 0$), j is complex number [116]. By involving Euler's formula 1.16 impedance is expressed as a complex function (1.16, 1.17, 1.18).

$$exp(ix) = cosx + isinx \tag{1.16}$$

$$cos(\omega t + \phi) = \frac{1}{2}\left[e^{j(\omega t+\phi)} + e^{-j(\omega t+\phi)}\right] \tag{1.17}$$

$$sin(\omega t + \phi) = \frac{1}{2j}\left[e^{j(\omega t+\phi)} - e^{-j(\omega t+\phi)}\right] \tag{1.18}$$

Given the symmetry, only the analysis for one right-hand term needs to be performed and can be simplified to 1.19 and 1.20:

$$cos(\omega t + \phi) = \Re\left\{e^{j(\omega t+\phi)}\right\} \tag{1.19}$$

$$sin(\omega t + \phi) = \Im\left\{e^{j(\omega t+\phi)}\right\} \tag{1.20}$$

When ϕ=0, potential can be described as 1.21 and current described as 1.22:

$$E_t = E_0 exp(j\omega t) \tag{1.21}$$

$$I_t = I_0 exp(j\omega t - j\phi) \tag{1.22}$$

Then impedance can be expressed as real and immaginary parts through a complex number in 1.23.

$$Z = Z_0 exp(j\phi) = Z_0(cos\phi + jsin\phi) \tag{1.23}$$

For interpretation of measured spectra real and an imaginary part of impedance expression through complex exponent can be understood by analysing Nyquist and Bode plots.

1.3.5.1 Interpretation of electrochemical impedance data

Nyquist and Bode plots (demonstrated in (Fig. 1.13)) are the most common data representation for EIS data analysis [67]. The advantage of the Nyquist plot provides a quick overview of the data, where qualitative interpretation can be achieved from the plot. Data from EIS is presented as a plot of $Z^{'}$ relative to $Z^{''}$ (y-axis) (in Fig. 1.13). When plotting data in the Nyquist format, the real absolute axis values must be equal to the imaginary axis so as not to change the curve shape [21]. The value of R_s appearing at high frequencies correspond to total cell resistance, including resistance of electrolyte solution [67]. R_{ct} is the main parameter used in Faradaic impedance for estimation of charge transfer resistance, which is usually observed at low frequency (0.1 Hz), showing diameter of semicircle.

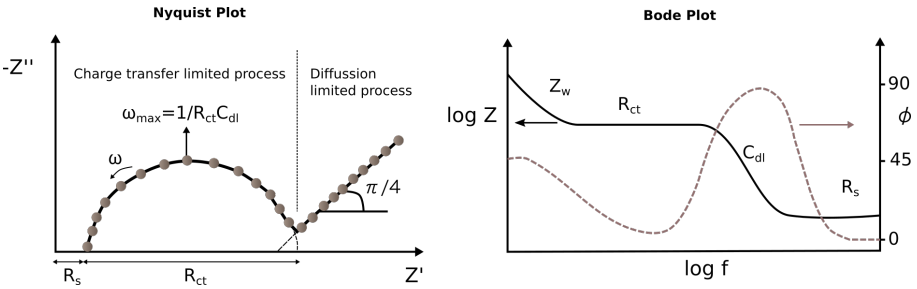

Fig. 1.13. *Nyquist and Bode plots reflecting signal at changing angular frequency. Parameters used in modelling of experimental data: R_s - solution resistance, R_{ct} is charge transfer resistance, C_{dl} is double layer capacitance and Z_w is Warburg element.*

For higher expression of lower values of impedance, another data presentation - Bode plot is used. The advantage of the Bode plot is that information of frequency is plotted, and an essential low impedance behaviour appears at high-frequency [21, 37]. Applied frequency values are presented on X-axis and the absolute values of the impedance and the phase-shift on the Y-axis (shown in Fig. 1.13).

Precise values of parameters described in Fig. 1.13 can be extracted by fitting the data using equivalent circuit models.

1.3.5.2 Modeling of electrode liquid interface

The modelling of the Nyquist plot (in Fig. 1.13) as the equivalent circuit is essential for the quantitative interpretation of data. As Warburg suggested (1899), the electrode-solution interface can be represented by polarisation resistance in a series with capacitors [14].

The equivalent circuit theory was improved when the Randles model was established in 1947 [14]. The Randles circuit model for microelectrodes is demonstrated in Fig. 1.20, where passive elements of resistors and Warburg impedance are integrated sequentially and parallel to form a complex equivalent circuit. In equivalent circuit model, resistor (R), capacitor (C), inductor (L) and distributed elements Constant phase element (CPE) and Warburg impedance (Z_w) are commonly used [136].

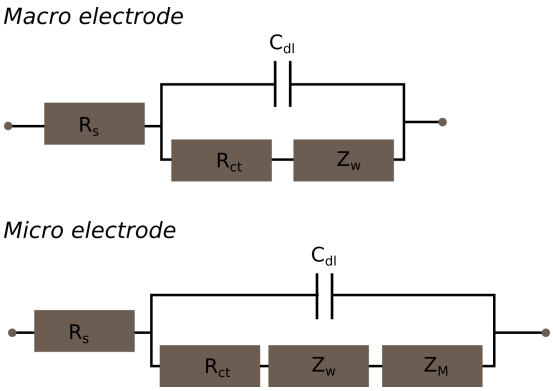

Fig. 1.14. *Equivalent circuit model for macro and microelectrode.*

Various simple electrical circuits were reported such as series of R-C circuit, parallel R-C circuit, RLC series circuit [37].

Randles circuit model is used as one of the simplest models describing kinetics and diffusion processes on the electrochemical interface. Briefly, Randles circuit model consists of an active electrolyte resistance (R_s) in series of parallel combined double-layer capacitance (C_{dl}) and a faradaic reaction consisting of active charge transfer resistance (R_{ct}) and unique electrochemical unit of diffusion - Warburg element (Z_w).

In a real electrochemical system, especially for microscale devices, spectra of impedance is more complex, and the Randles circuit does not always give expected results. Here, the main difference between macro and microelectrodes can be related to a different diffusion profile. Unfortunately, microelectrodes require analytical solution by modifying the Randles circuit to include different type of diffusion. Usually, macroelectrodes are associated with a planar diffusion and microelectrodes are associated with spherical diffusion.

As it was reported in the literature, microelectrodes have two dominating types of diffusion at high and low frequency. Commonly, Randles equivalent circuit can be modified as shown in Fig. 1.14 to have a better fitting model consist of spherical diffusion impedance at a high frequency (Z_M) and Warburg element for low frequency (Z_w)[72].

1.4 Difference between macro and micro electrodes

In macro electrodes, the diffusion layer thickness is much smaller in comparison with the size of the electrode leading to linear diffusion [30]. Additionally, the shape of the electrode is not essential, as long as the electrode is planar and dimensions of the electrode are more significant than the thickness of the diffusion layer δ (1.24).

$$\delta \sim \sqrt{Dt} \tag{1.24}$$

Depending on dimentions of macroelectrodes, diffusional transport to the electrode surface can be planar or radial(spherical).

Additionally, spherical diffusion can be measurable for electrodes of millimetres in radius. For linear diffusion electrodes of size $\geqslant$ 4 mm radius for electrochemical investigation are recommended[102]. Scan rate equation1.25:

$$v = \frac{RT}{Ft} \tag{1.25}$$

Diffusion layer thickness δ of electrode can be calculated based on equation 1.26:

$$\delta = \frac{FADc}{I} \tag{1.26}$$

For planar electrode diffusion thickness δ:

$$\delta = \frac{\sqrt{\pi}\sqrt{D}}{z}\sqrt{\frac{RT}{Fv}} \tag{1.27}$$

1.4.1 Design of microelectrodes and microelectrode array

Microelectrodes are the type of electrodes where at least one of dimension is in microscale range (less than 1000 μm) [13].

For microelectrode where radial diffusion is dominating, the flux of redox molecules toward the electrode is much faster in comparison to micro-electrode, where a planar diffusion is dominating Fig. 1.15[13].

The electrochemical properties of microelectrodes variate depending on the design and arrangements of the electrode configuration. The kinetics of voltammogram for macro electrodes can be analysed by studies of the position of the half-wave potential $E_{1/2}$. At this potential, the current reaches half of its maximum [31].

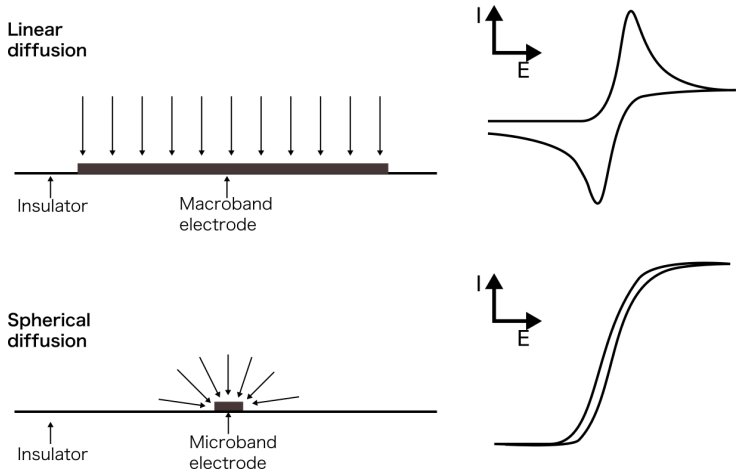

Fig. 1.15. *Diagram of diffusion and typical cyclic voltammograms: linear diffusion for macro and spherical for micro electrodes.*

For microelectrode or microelectrode arrays, the diffusive mass transport can keep the surface gradient constant with time, and the steady-state current is achieved [31]. In this case any potential of steady state current can be used, which simplify data analysis when microelectrodes or microelectrode arrays are used.

1.4.2 Interdigitated microelectrode array

In microelectrode array where single microelectrodes placed very close to each other allows overlapping of their diffusion layers leading to significant sensitivity benefits and higher signal to noise ratio [146]. Very important characteristic parameters for a microband electrode are its width W_e and length L. Considering those facts, Aoki has derived an equation for the diffusion layer thickness of a microband electrode in a dimensionless time-domain (θ) [146].

In microband electrode case,

$$I = I_{Cott} + \frac{zFcDP}{2} \tag{1.28}$$

$$\Theta = \frac{Dt}{W_e^2} \tag{1.29}$$

$$\delta = \frac{W_e}{0.97 - 1.1e^{-\frac{9.9}{|\log(12.37\Theta)|}} + \frac{1}{\sqrt{\pi}\sqrt{\Theta}}} \tag{1.30}$$

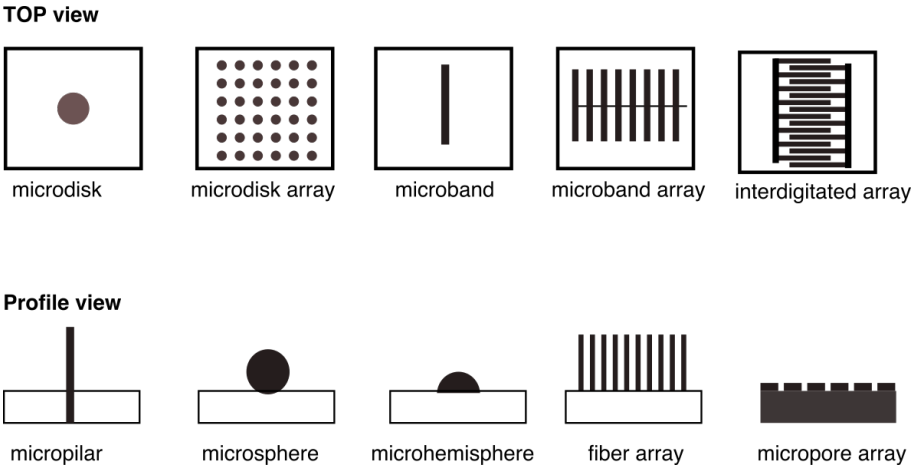

Fig. 1.16. *Diagram of the main types of microelectrodes and microelectrode arrays.*

$$\delta = \frac{W_e}{0.97 - 1.1e^{-\left|\log\left(\frac{12.37D}{W_e^2}t\right)\right|^{\frac{9}{9.9}}} + \frac{1}{\sqrt{\pi}\sqrt{\frac{Dt}{W_e^2}}}} \tag{1.31}$$

In Fig. 1.17 diagram of two microband electrodes is demonstrating overlapping of diffusion layers depending on dimensions of an electrode and a distance between electrodes. Overlapping of diffusion layers can be controlled by the design of electrode arrays, where no diffusion overlap, partial diffusion overlap or a total diffusion overlap can be achieved [146].

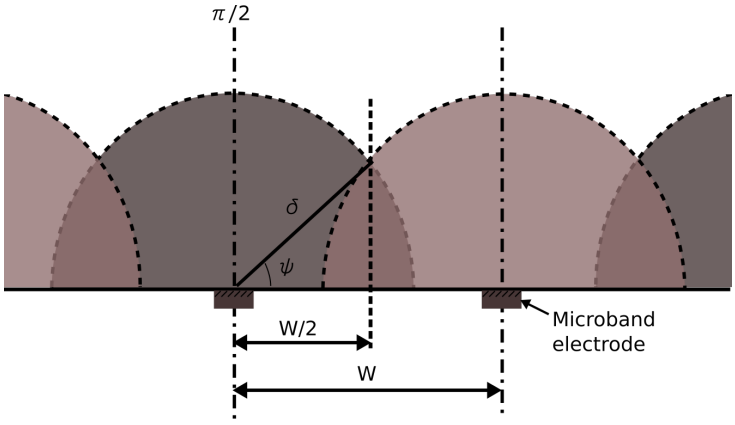

Fig. 1.17. *Diagram of diffusion layer overlap for a microband electrode array.*

For instance if δ < W/2 (in Fig. 1.17), where $W = W_e + W_g$ and Wg is the gap width between two adjacent microelectrodes, no diffusion layer overlap and the total current of the microelectrode array is equal to the sum of the currents of all microelectrodes coupled in the array [146]. On the other hand, when δ > W/2 (in Fig. 1.17) diffusion layers are partially overlapped and overlapping angle, ψ is growing as with diffusion layer thickness. At the point when ψ is equal to $\delta/2$, diffusion layers are described as fully overlapped [146]. Diffusion problems accrued on microelectrodes can be carried out by numerical simulations, where the flux of electroactive species through a solution to the electrode surface is described by Fick's First Law or Fick's Second Law [31].

1.4.3 Simulation of electrochemical diffusion

By solving the mass transport equation at various electrodes, the current response can be simulated as a function of applied potential. To simulate the cyclic voltammetry, the applied potential varies as a linear function of time, determined by the scan rate v ($\mathrm{mV}s^{-1}$) [82, 31].

For an explanation of flux caused by redox activity, some boundaries need to be considered. The energy of the electrons in the donor orbital of reduced species must be higher (or equal) than the energy of electrons in the electrode during oxidation. Also, the energy of the electrons during reduction on electrode must be higher than the energy in the acceptor orbital. The electrical current on an electrode depends on the electrode potential. Considering that both a cathodic and an anodic reaction occur on the same electrode, relationship between current density and potential is described by Butler-Volmer equation (1.32).

$$j = j_0 \cdot \left\{ \exp\left[\frac{\alpha_\mathrm{a} z F}{RT}(E - E_\mathrm{eq})\right] - \exp\left[-\frac{\alpha_\mathrm{c} z F}{RT}(E - E_\mathrm{eq})\right] \right\} \qquad (1.32)$$

Most of the Faradaic processes can be modelled using this equation consist of anodic and cathodic current terms, j - electrode current density, j_0- exchange current density, E - electrode potential, E_{eq} - equilibrium potential. T - absolute temperature, z - number of electrons involved in the electrode reaction, F - Faraday constant, R - universal gas constant, α_a - cathodic charge transfer coefficient, α_a - anodic charge transfer coefficient, η - activation overpotential (defined as η = E - E_{eq}).

In case, when E = E_{eq}, no net current flow happens but cathodic and anodic current density terms still changes depending on exchange current density.

Although the Faradaic process is usually the primary process of the electrode reaction study, the non-Faradaic process must be considered.

Non-faradic processes such as adsorption or desorption can replace the electric double layer, thus changing the electrode area, potential and current [13].

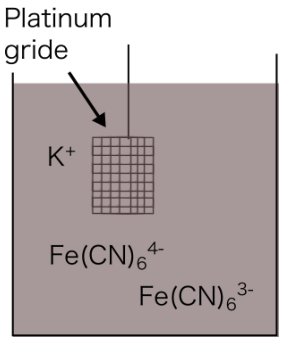

Fig. 1.18. *A platinum grid immersed into redox solution containing* $Fe(CN)_6^{4-}$ *and* $Fe(CN)_6^{3-}$.

To measure the potential difference between electrode and solution second electrode (reference electrode) is introduced in the system. Ions solution in the reference electrode also has it's potential, depending on ions activity. As solutions are non- ideal, ions from higher concentration should move to lover concentration trying to reach equilibrium. Therefore, some ions can move faster than others, depending on single-ion conductivity in water. It is crucial in reference electrode that ions in solution are in equilibrium, meaning that ratio of potential of positive and negative ions have to be equal to 1 and have similar speed if they move from higher to lower concentration, so commonly Ag/AgCl electrodes are used.

In case when ionic strength is only one variable in the system, diffusion equation (from Fick's second law) for the macroelectrode can be described as a parabolic second-order partial differential equation [82]:

$$\frac{\partial c}{\partial t} = D\frac{\partial^2 c}{\partial^2 z} \tag{1.33}$$

The electrode is modelled in the cylindrical coordinate system (r, Φ, z). r- radial distance, Φ -angular coordinate, and height - z , where the angle coordinate $\Phi = 0$ due to the symmetry of the electrodes. If the diffusion is radial to the electrode and the concentration is not evenly distributed along the r direction. The diffusion equation for microdisk electrode is [82]:

$$\frac{\partial c}{\partial t} = D\left(\frac{\partial^2 c}{\partial^2 r} + \frac{1}{r}\frac{\partial^2 c}{\partial r} + \frac{\partial^2 c}{\partial^2 z}\right) \tag{1.34}$$

For the microcylinder electrode only the radius of the microcylinder is at microscale and the diffusion equation is written as:

$$\frac{\partial c}{\partial t} = D\left(\frac{\partial^2 c}{\partial^2 r} + \frac{1}{r}\frac{\partial^2 c}{\partial r}\right) \tag{1.35}$$

The simulation space and boundary conditions for a microband electrode is the same as that for a microdisc in normal coordinate system:

$$\frac{\partial c}{\partial t} = \frac{\partial^2 c}{\partial^2 r} + \frac{\partial^2 c}{\partial^2 z} \tag{1.36}$$

where D is the diffusion coefficient, and c is the concentration of the species which is a function of the time t and coordinates r, Φ, z. When designing microelectrode arrays for sensor applications, it is recommended to keep diffusional independence on electrode bands avoiding overlapping effect in order to achieve higher sensitivity [98].

1.5 Fabrication techniques of macro-/-micro-electrodes

Beam lithography and ink-based screen printing of electrodes were reported as a common techniques in fabrication of electrodes. Wide range of materials for working electrode fabrication have been reported covering metals: Au, Pt, Ag and alloys (e.g. ITO), carbon-based materials: glassy carbon, graphite, diamond [130, 163, 33] and carbon-based materials [168, 134, 2, 115], also conductive polymer films [115, 27].

Usually, the metal film is deposited initially on an electrically insulating substrate [20]. This is followed by deposition of a protective positive photo-resist, which is patterned and developed using photolithography. Various designs and sizes of microstructured gold patterns can be fabricated [146].

1.5.1 Micro contact printing

Micro-contact printing is commonly called as soft lithography, and various application of such a technique exists from SAMs formation to protein immobilisation. This method allows to precisely control the position and pattern of printed material on the substrate. Microcontact printing and printing transfer approaches represent an alternative lithography method for fabrication of nano- or microstructured gold patterns [162, 59]. Microcontact printing (μCP) is a form of soft lithography that uses patterns on polydimethylsiloxane (PDMS) stamp [114]. The pattern consisting of self-assembled monolayers (SAMs) of ink is formed as

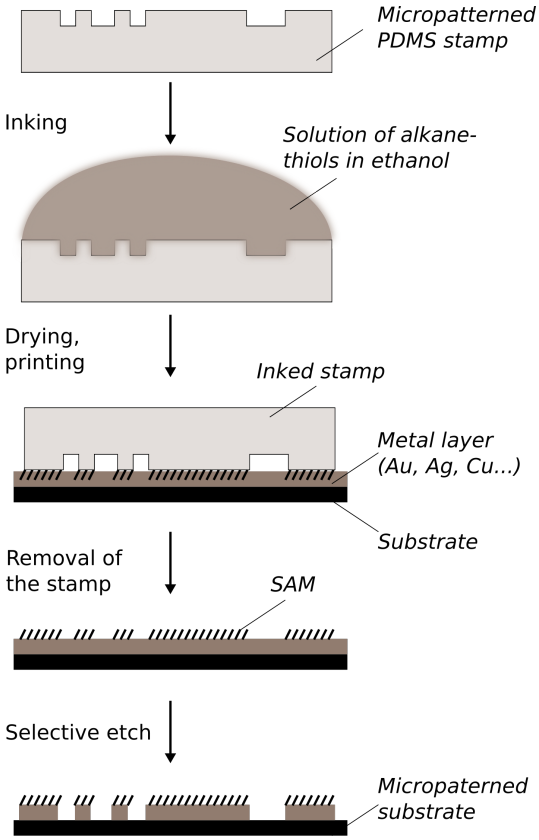

Fig. 1.19. *Scheme of microcontact printing of SAMs and etching for fabrication of microstructures (adaptive from [56]).*

a mask on the surface of a substrate (for example, gold) [55]. Usually, PDMS stamp with a wide range of structures from dots to lines or even complicated hollow structures is formed by mould replicating the master made by beam lithography. Subsequently, a stamp is incubated for some time with ink, which can be an alkanethiol solution or protein solution (e.g. fibronectin, antibodies). After gentle removing of ink, the ink is transferred onto a previously cleaned substrate. Depending on the application, it can be gold surface, functionalised glass, silica or even simple plastic.

Such a technique can be used for fabrication of various conductive structures, e.g. microelectrodes. Various patterns of SAMs can be formed on a clean gold surface using microcontact printing to protect the metal surface from etching compounds.

1.5.2 Wet etching

Removal of the unprotected metal by etching and dissolving of the remaining photoresist leaves a patterned metal on the substrate [11]. There are several papers where wet etching technique was used for the preparation of metal-based microelectrode arrays [1, 57, 11]. Wet etching has an advantage because this process does not require high-cost equipment such as high energy plasma systems used for dry etching.

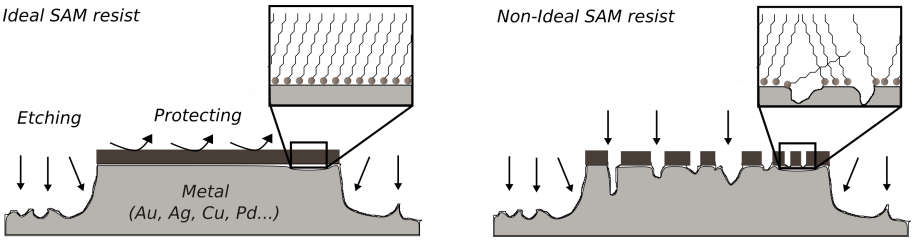

Fig. 1.20. *Scheme of wet etching demonstrating ideal SAM resist and non-ideal SAM resist (adaptive from [56]).*

Wet etching is a chemical process where depending on application non-protected selected materials (e.g. Au, Ti, Al, Si) can be removed from the substrate surface by incubating patterned thin layer in the wet etching solution. Wet etching removes the material through a chemical reaction between the etching solution and the layer to be etched. Various types of liquids can be used for wet etching process such as KOH, SF_6, BCl_3 , HF depending on etch materials.

As a wet etching solution especially for metals mixture of $Fe(NO_3)_3$ and CH_4N_2S is used [41]. The etching compound can interact with the layer under protecting mask. Accordingly, it is essential to optimise etching conditions such as etching liquid recipe including the ratio of used materials, concentration, time and temperature.

1.5.3 Increasing of electrochemically active surface area by electroplating

The electroplating process is used to increase the electrochemically active surface area (EASA), leading to improve the performance of sensors. Electroplating is also used to modify surfaces changing surface chemical properties. For instance, the platinum group metals are the most active electrocatalysts available and can be easily applied for hydrogen peroxide detection. As hydrogen peroxide plays a considerable role in various fields, e.g. in ferment reaction. Biosensors based on Pt nanostructures display higher sensitivity as compared to bare Pt electrodes [26]. Electroplating

is also used to modify surfaces changing surface chemical properties. For example, the platinum group metals are the most active electrocatalysts available and can be easily applied for hydrogen peroxide detection. Biosensors based on Pt nanostructures display higher sensitivity as compared to bare Pt electrodes [80].

Platinum group metals are one of the most active electrocatalysts available [26] and these metals can be easily applied for the fabrication of IDA microelectrodes for hydrogen peroxide detection. Biosensors based on Pt nanostructures display higher sensitivity as compared to bare Pt electrodes [143]. The use of platinum for electrode fabrication has been a significant issue because of the scarcity of resources and relatively high price. Possible solutions of this problem are a synthesis of materials with electrocatalytic properties similar to those of platinum group metals or reducing the amount of platinum by dispersing thin layer of small nanoparticles onto substrates [148]. One of the main challenges in the preparation of high-quality platinum IDA electrodes is the weak adhesion between platinum layer and the substrate, what has limited the commercial availability and use of such electrodes [85]. In review articles, the methods of chemical and electrochemical deposition of platinum group metals from aqueous solution have been discussed [119, 39, 166, 12, 127]. Treatment of the substrate with copper precursor is usually required to form an adhesion layer before deposition of platinum from Chloroplatinic acid [20].

2. Experimental part

2.1 Materials and solutions

All reagents were of analytical grade and used without further purification. Aqueous solutions were prepared in MilliQ water (18.2 MΩcm) from a Synergy 185 unit equipped with a UV lamp (Millipore, USA). All experiments were carried out at room temperature 21 ± 2 °C.

2.1.1 Materials and solutions for fabrication and modification of electrodes

- 20 nm of gold-coated glass plates (10 × 10 mm) were purchased from Ssens (Netherlands).
- Standard cleaning solution (SC_1) was composed in a 5:1:1 mixture of H_2O, H_2O_2 and NH_3. H_2O_2 (30 %), NH_3 (25 %) solutions were obtained from Carl Roth GmbH (Germany).
- The master was fabricated on Si plate using a SU-8 photoresist (MicroChem Corp, USA) spin coated on Si with the thickness of 40 µm and then pattern by photolithography. Such a master was reused several times.
- Polydimethylsiloxane (PDMS) replicas were prepared by mixing elastomer and elastomer curing agent in 10:1 mass ratio from SYLGARD® 184 silicone elastomer kit (Dow Corning, USA). Degassed mixture was cast on master (described above) and placed for 2 h at 70 °C in the oven. Subsequently, PDMS replicas were carefully peeled of the master and stored in closed plate. Prior, µCP, PDMS replicas were sonicated in C_2H_5OH for 1 min and dried in N_2.
- As a ink for µCP $C_{20}H_{42}S$ eicosanethiol (Alpha Aesar, Germany) prepared in C_2H_5OH (distillate before use) (Sigma Aldrich, Germany) was used.
- For wet etching of gold 20 mM $Fe(NO_3)_3$ (Fluka, Switzerland), 30 mM CH_4N_2S (Fluka, Switzerland) were used.
- For electrode surface modification 10 mM $HAuCl_4$ x H_2O (Sigma Aldrish, Germany) and 10 mM $H_2PtCl_6H_2O$ (Sigma Aldrish, Germany) electroplating solution was used.
- Class 5.0 N_2 gas (Aga, Lithuania) was used for drying substrates.

2.1.2 Materials for immunosensing studies

Required dilutions of anti-CA125 antibody were made from 1 $mgmL^{-1}$ monoclonal mouse anti-CA125 (HyTest, Finnland). Several dilutions of CA125 were prepared from 1 $mgmL^{-1}$ of CA125 human antigen (HyTest, Finnland). Aqueous phosphate-buffered saline (PBS) pH 7.4 (from Sigma Aldrich, UK) was used to prepare protein solutions. For specificity test bovine serum albumin (BSA), human serum albumin (HSA), fibrinogen and IgG obtained from Sigma Aldrich, UK were used.

2.1.3 Reagents for electrochemical analysis

$K_3[Fe(CN)_6]$ and $K_4[Fe(CN)_6]$ were purchased from Sigma Aldrich (UK) and used for CV and EIS measurements. Phosphate buffer (PB), pH 7.4, was employed as electrolyte and it was prepared from 1 M stock solutions of Na_2HPO_4 (Sigma Aldrich, UK) and NaH_2PO_4 (Sigma Aldrich, UK). Hydrogen peroxide solution of 0.1 M was prepared freshly in PB (from stock solution of 35 % H_2O_2 obtained from Carl Roth GmbH (Germany)).

2.2 Methods for fabrication of interdigitated array electrodes

2.2.1 Design of electrode

Design of electrode consisted of 25 units of 40 µm width and 0.9 mm length interdigitated micro-band array electrodes (Fig. 2.1), with a distance of 40 µm between integrated area. 1 mm width lines were design as a connection part of electrode. The zones with h = 1.5 mm was design to prevent alignment issue during fabrication of electrode.

2.2.2 Fabrication of silica master

The photolithograpy mask was fabricated using photolithography with DWL66, Heidelberg Instruments. The master for the layout fabricated in house. The positive resist ma-P 1275G (Microresist GmbH, Germany) was spin-coated on the 4 inch silicon wafers (Topsil, Denmark) to form a 20 um thick resist layer. After prebaking the spin-coated photo-resist layer was UV (405nm) exposed using a laser lithography equipment from Heidelberg Instruments. The exposed pattern layout was developed using a developer (Microresist GmbH, Germany). The developed resist was baked at 65 °C for 1 h and silanized with fluorosilane in a custom-made vacuum chamber (Nanoengineering group).

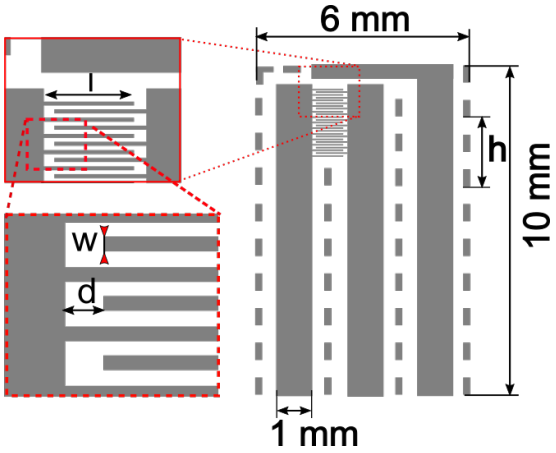

Fig. 2.1. *Design of the chip: microelectrode array of 25 interdigitated electrodes, where length of electrode l = 0.9 mm and with w = 40 µm, d = 100 µm, isolated zones (h = 1.5 mm) for stability of µCP were also designed, width the connections of 1 mm to connector.*

2.2.3 Fabrication of PDMS stamp

Fabrication of elastomer replica polydimethylsiloxane (PDMS) was performed by mixing elastomer and it's curing agent in 10:1 mass ratio from SYLGARD 184 silicone elastomer kit (Dow Corning, USA). The degassed mixture was cast on master mentioned before and cured for 2 h at 70°C in an oven. After curing, PDMS replicas were carefully peeled and examined under optical microscope (Olympus BX-51, Japan).

2.2.4 Micro contact printing and wet etching

The diagram of fabrication of IDA electrode is shown in Fig. 2.2. 20 nm thickness gold surface was washed twice using SC_1 solution heating on the heater plate at 85 °C for 7 min, followed by extensive rinsing with ultrapure water and drying in the N_2 stream.

10x10 mm^2 PDMS stamp was sonicated in ethanol for 1 min before use. Afterwards, PDMS was covered with 50 µL of eicosanthiol (HS-C_{20}) from 1 mM solution in ethanol for 1 min and gently dried in N_2 stream. PDMS stamp and the gold substrate contact time was optimised to 1 min. Unprotected gold with the mask was etched using wet etching. Different times were used to optimise the quality of the etched gold structures. For wet etching of gold, 20 mM $Fe(NO_3)_3$ (Fluka, Switzerland) and 30 mM CH_4N_2S (Fluka, Switzerland) were mixed in 1:1 volume ratio and gold substrate immersed for 5min.

The resulting Au patterns were treated with UV (254 nm wavelength)

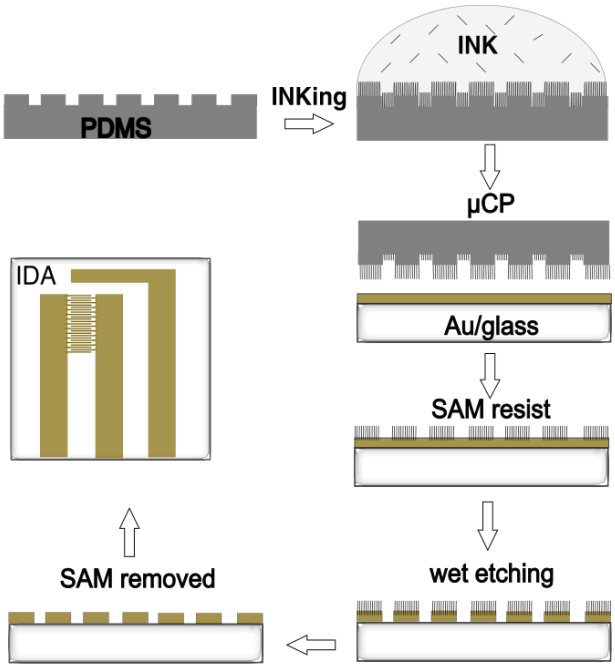

Fig. 2.2. *Diagram of IDA fabrication steps including microcontact printing for resist eicosanthiol (HS-C_{20}), wet etching and removing of resist.*

radiation for 20 min and ultrasonicated in ethanol for 2 min to remove the products of HS-C_{20} resist degradation. Additionally, gold microelectrodes after UV treatment were cleaned in SC_1 solution twice.

2.3 Surface characterisation of interdigitated array electrodes

2.3.1 Optical Microscopy

The quality of the PDMS replica was investigated using microscope prior to microcontact printing (μCP) in the fabrication of gold IDA electrode. Also, HS$-C_{20}$ SAM micro-patterned gold after chemical etching was studied with the same optical microscope with magnification of 10×, 20×, 50× in mapping function.

2.3.2 Characterisation of surface by SEM and EDS

Pt images were acquired with a scanning electron microscope Hitachi S3400N VP-SEM (Japan) operating at an acceleration voltage of 10 kV.

SEM was used for analysis of the morphology of electroplated gold and platinum nanostructures on screen printed electrodes. The electroplated Pt on IDA was characterised by JEOL JSM 6490 LV (Japan) equipped with an energy dispersive X-ray spectroscopy (EDS) detector. Additionally, Pt structure was studied with a high resolution SEM Helios NanoLab 650 (The Netherlands).

2.3.3 Electrochemical characterisation

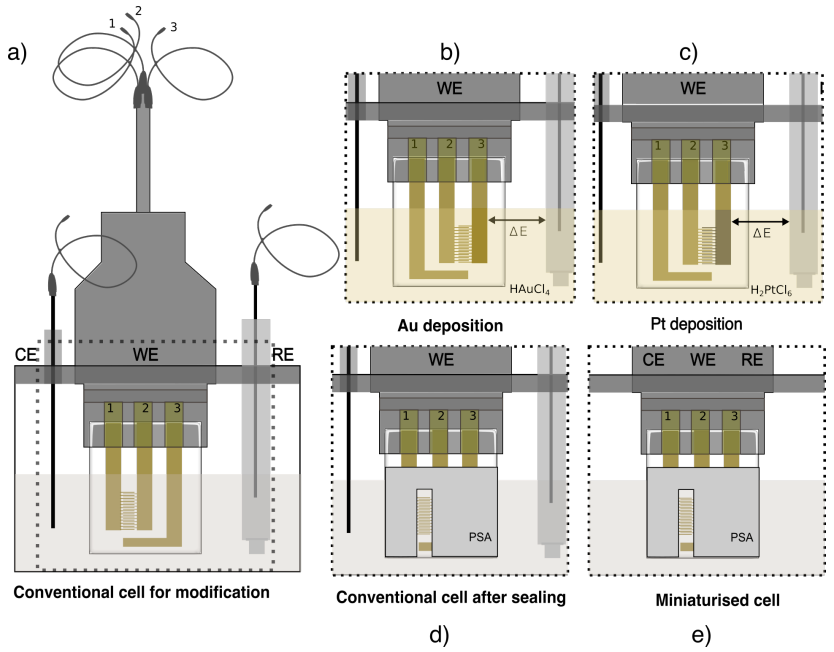

Fig. 2.3. *Diagram of conventional electrochemical cell with external CE, RE - a) for selective electroplating of Au b) and Pt c). The region of interest was sealed using PSA d). Miniaturised electrochemical cell with internal CE, RE e)*

Electrochemical studies were carried out with the potentiostats CH Instrument 760e (USA), CompactStat, IVIUM Technologies (Netherlands) or Autolab PGSTAT 30 (Netherlands). Whole microelectrode was connected to custom made connection (as shown in Fig. 2.3), where 1^{st}, 2^{nd} and 3^{rd} were clipped in a several configurations described later.

2.4 Modification of electrode by Pt and Au nanostructures

Electrochemical cell for Au and Pt electroplating is shown in Fig. 2.3. Electrodeposition of Pt on the Au microelectrode was performed in aqueous solution of 10 mM $H_2PtCl_6 \cdot 6\,H_2O$. Pt wire and Ag/AgCl/3 M KCl were used as an external counter electrode and reference, respectively. Pt was deposited by means of cycling the potential of microelectrode within the potential range of -0.4 - 0.8 V varying the potential scan rates from 5 mVs^{-1} to 50 mVs^{-1}.

Gold was electroplated from 6 mM $HAuCl_4 \cdot 6\,H_2O$ solution on IDA electrodes using cyclic voltammetry method, within potencial range of -0.8 - 0.9 V and scan rate of 100 mVs^{-1}.

2.4.1 Several configurations of electrochemical cell

The area of interest on IDA electrode was a microcomb region. To avoid electrochemical signal from electrode tracks zone, the track zone was sealed using double-sided pressure sensitive adhesive (PSA) tape (140 µm thick, ARcare 90106 from Adhesive Research Ltd., Limerick, Ireland) design as 1x3.5 mm (in SolidWork software) as shown in Fig. 2.3. The shape of the sticker cut using a computer-controlled Cameo 3 blade cutter (Silhouette, Inc., Lindon, UT, USA)

2.4.2 Simulation of diffusion on interdigitated array electrodes

The COMSOL Multiphysics 5.3a used for the simulations. Simulations have been carried out on a Windows PC equipped with 32 Gb Intel(R) Core (TM) i5-6500 CPU @ 3.20GHz. CV was generated based on finite differential method comparing interdigitated and non-interdigitated WE and CE electrodes. All simulations have been performed for 3 cycles of CV between -0.3 and 0.3 V with several scan rates including 10, 30, 50, 100, 150, and 200 mVs^{-1}).

2.4.3 Electrochemical analysis on miniaturised electrochemical cell

Electrochemical measurements were carried out in 5 µL (as shown in Fig. 2.4) in ferrocene methanol (FcMeOH) supported with 0.01 M PB, pH 7.4 on IDA configuration. CV was recorded in the potential window from -0.2 to 0.4 V at the scan rates of 5 and 50 mVs^{-1} vs. Au pseudoreference.

Range of concentrations of FcMeOH from 0.5 µM to 1000 µM were scanned for calibration.

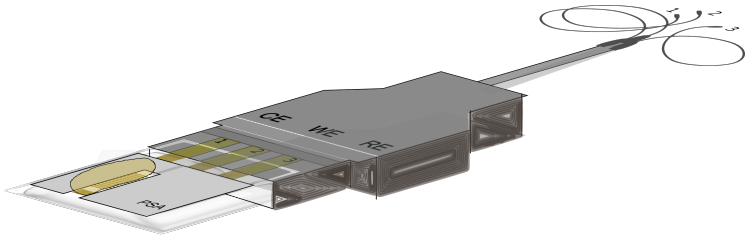

Fig. 2.4. *Pseudo3D image of IDA electrode for measurements in 5 µL solution.*

2.5 Modification of interdigitated array for detection of carcinoma antigen 125

2.5.1 Self assembled monolayer formation on interdigitated array surface

After SC_1 treatment, IDA were immersed into 70 % HS−EG_3−COOH and 30 % of HS−EG_6−OH ethanol solution (as shown in Fig. 2.5) overnight. The IDA electrode was subsequently ultrasonicated for 3 seconds in purified ethanol (95 %) and rinsed with water and gently dried in the N_2 stream. IDA electrode modified with SAM and sealed with PSA stored at room temperature.

2.5.2 Immobilisation of antibody

Terminal groups of -COOH were activated with a mixture of freshly prepared 0.2 mL of 2.5 mM N-hydroxysuccinimide (NHS) and 10 mM 1-ethyl-3-[3-imethylaminopropyl] carbodiimide hydrochloride (EDC) in ethanol for 30 min. Subsequently, the IDA electrode removed from thiol solution and ultrasonicated in MilliQ water for 3 seconds. Finally, the IDA electrode was rinsed with MilliQ water to remove ethanol molecules and gently dried with N_2 stream.

Anti-CA125 diluted 1:100 in 0.1 M PB with freshly added NaCl was immobilised on NHS/EDC activated surface using microcontact printing (using flat PDMS) procedure with ink incubation time of 5 min on stamp, stamp and gold contact time of 10 min. Subsequently, 2 µL of 0.5 % of BSA in 0.1 M PB was drop-coated for 30 min to block active sites of NHS/EDC to prevent electrode surface from non-specific adsorption of

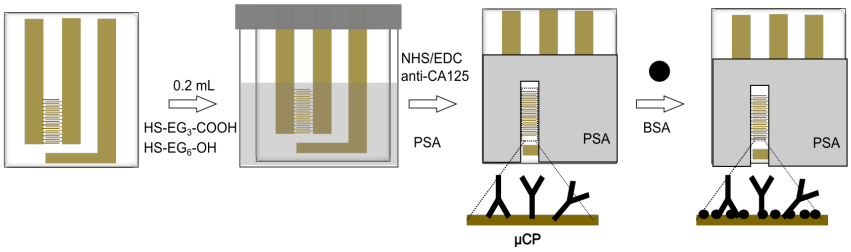

Fig. 2.5. *IDA electrode was blocked by SAM consisted of 70 %* $HS-EG_3-COOH$ *and 30 % of* $HS-EG_6-OH$ *ethanol solution overnight, NHS/EDC activation, anti-CA125 immobilisation, PSA sealing. To prevent non-specific binding IDA was blocked with BSA.*

other protein. The immunosensor was stored in the fridge at 4 °C before use.

2.5.3 Studies of antibody loading

The surface coverage of anti-CA125 was investigated by imaging null ellipsometer Accurion GmbH, NanofilmEP (Germany) with a laser emitted light with a wavelength of 658 nm. Additionally, this instrument has an integrated objective system and CCD camera for imaging. Such a system is capable not only to measure thin film thickness according to refractive index changes, but also generating 3D maps of selected regions of interest (ROIs). Mapping measurements were performed at the 56° angle of incidence. The -COOH layers and ani-CA125 were modelled as an 'organic' layer with a refractive index of n = 1.5 and k = 0. The corresponding layer thicknesses were determined for each substrate before -COOH preparation and kept constant during anti-CA125 pattern analysis. Also, integrated SPR system has been used for analysis of real time binding of biomarker CA125, with a flow rate of 25 $\mu Lmin^{-1}$.

2.5.4 Electrochemical characterisation of sensor fabrication

CHInstrument was used for EIS measurements in the frequency range from 0.1 Hz to 10^6 Hz at open circuit potential in 1 mM FcMeOH after each fabrication step. The voltage perturbation amplitude was 10 mV with 20 data points in total. The data were plotted as Nyquist and Bode plots and fitted to Randles equivalent circuit, from which charge transfer resistance - R_{ct} and other parameters were compared.

3. Results and discussion

3.1 Characterisation of interdigitated array electrode

IDA electrodes were fabricated using the procedure described in section 2.2. Soft lithography and wet etching were combined with having rapid IDA electrode fabrication. HS-C_{20} thiol was chosen as ink to form a thin well-packed SAM hydrophobic restive molecular layer to protect patterned Au from the wet etching process. Several µCP and wet etching times 0.5 min, 1 min, 2 min, 5 min and 10 min were investigated.

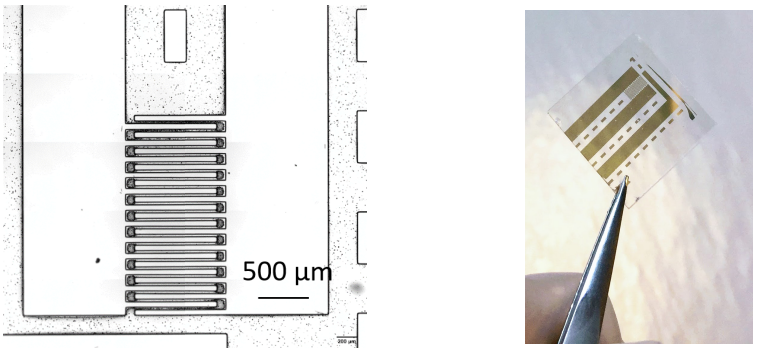

(a) *(b)*

Fig. 3.1. *Optical microscope image of fabricated PDMS stamp, showing region of interest with 40 µm microband array (a); IDA electrode after optimised conditions: µCP time of 1 min fallowing wet etching time of 5 min (b).*

To form the homogenous layer of such a resist the contact of PDMS stamp and 20 nm Au-covered glass substrate was limited to 1 min to avoid ink spread issues. The contact times lower than 1 min caused fair coverage by the resist (Fig. 3.2). After µCP process, the PDMS stamp was sonicated in ethanol for 30 s and reused for several (up to 15) µCP procedures on new Au substrates. More prolonged usage caused issues such as swelling of PDMS stamp itself, leading to an increase of the width of printed resist. As a quality of IDA, the width of microband and defects (Au micro/nanostructure in resist free zone) were tracked using an optical microscope. First of all, the quality of the resist layer was optimised by changing µCP of eicosanthiol (HS-C_{20}) time from 0.5 to 10 min and applying 5 min wet etching procedure. The correlation between width values of microband and IDA fabrication parameters is shown Fig. 3.2. The fabricated microband structures after the wet etching process had a

higher width when µCP contact time was longer than 1 min.

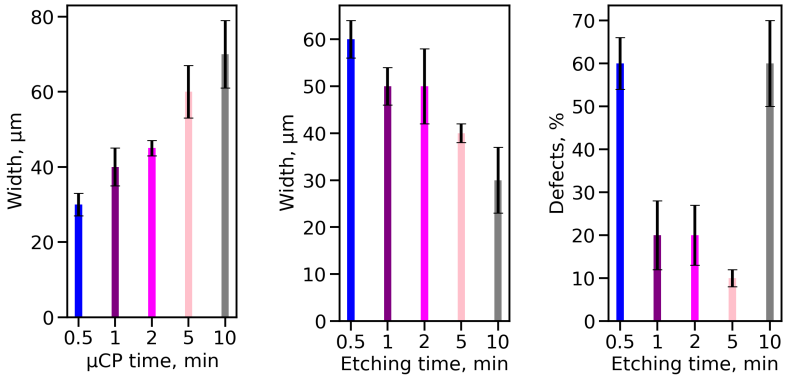

Fig. 3.2. *Comparison of influence to the width of IDA microband at several times of µCP) (a), wet etching (b) and reserved defects (c) at several etching times, showing wanted width of microband of 40 µm obtained at µCP time of 1 min and lowest amount of defects obtained after wet etching time of 5 min.*

It was noticed that wet etching process for microband array zone was faster than that for contact track zone, so an optimisation of etching time was required. At shorter etching times (1 - 5 min) some micro-/nanostructures of Au were remaining in the resist free area. Longer etching times caused an increased roughness on the edges of the microband array leading to a lower width (35 ± 5 µm) of microband. The etching time was limited upto 5 min giving an expected width value of 40 ± 2 µm (Fig. 3.3).

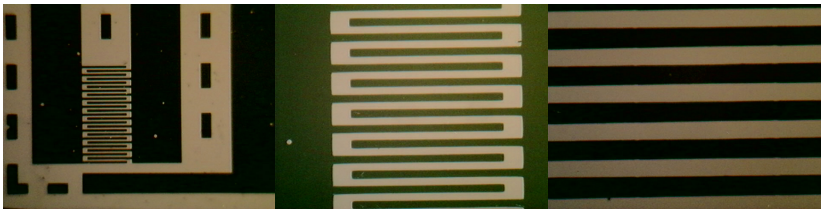

Fig. 3.3. *Bright-field microscope images of IDA fabricated under optimised conditions, showing area of 3 electrodes (a), zoom in area of interdigitated microband electrodes (b) and zoom in showing defects free zone (c) after 5 min of wet etching.*

The PDMS stamp inking, µCP and wet etching for fabrication of IDA took no longer than 10 min. In such a way, 125 units of hand made IDA electrodes were fabricated for further application. Before electrochemical characterisation, fabricated IDA electrodes were treated using high energy UV light. Several times: 10, 30, 60 min, were tested under incubation of UV light to make sure that -SH bond of thiol is destroyed. As 10 min was too short of obtaining clean Au surface and 30-60 min lead to clean Au surface, 30 min was chosen as the optimal (shorter) time for UV treatment to remove remaining thiol resist. To avoid any impurities of remain thiols, the IDA electrodes were washed in SC_1 solution (as described in subsection 2.2.4) leading to the hydrophilic Au surface as proof of clean electrode.

3.2 Modification of interdigitated array electrodes with Pt coating for H_2O_2 detection

Fabricated IDA was connected to a modified USB port (as shown in Fig. 3.4 (a)) for Pt deposition by electroplating using cyclic voltammetry (see section 2.4). The CV during electroplating in (b), where chloroplatinic acid was used for the formation of Pt layer on Au IDA, is shown in Fig. 3.4. Main electrochemical process during electroplating in the solution of H_2PtCl_6 is shown in equation 3.1.

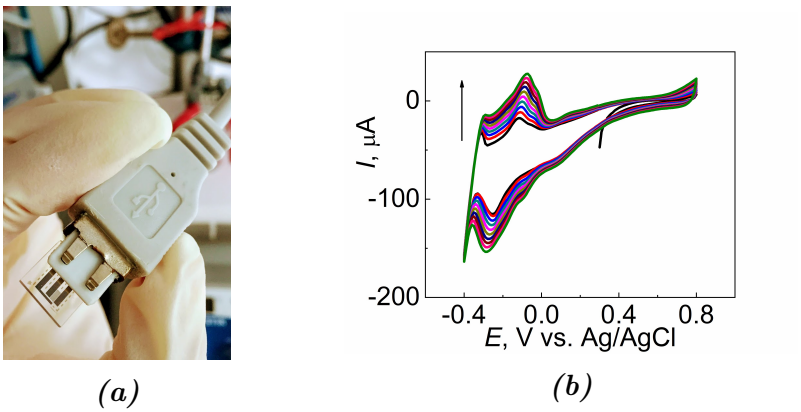

(a) *(b)*

Fig. 3.4. *Modified USB port for IDA connection (a) CVs of Pt electroplating in the potential region from -0.4 to 0.8 V of in 10 mM H_2PtCl_6, at 50 mVs^{-1}, 10 scans (b).*

$$H_2PtCl_6 + 4e^- \rightarrow Pt^0 + 2H^+ + 6Cl^- \tag{3.1}$$

Several potential scan rates from 10 to 100 mVs^{-1} were investigated in order to determined EASA and morphology of Pt. The EASA of Pt coating was evaluated according to the model of hydrogen monolayer adsorption/desorption on Pt, assuming that the theoretical charge density corresponding to the monolayer of adsorbed hydrogen on ideal polycrystalline Pt surface is 0.21 $mCcm^{-2}$ [38].

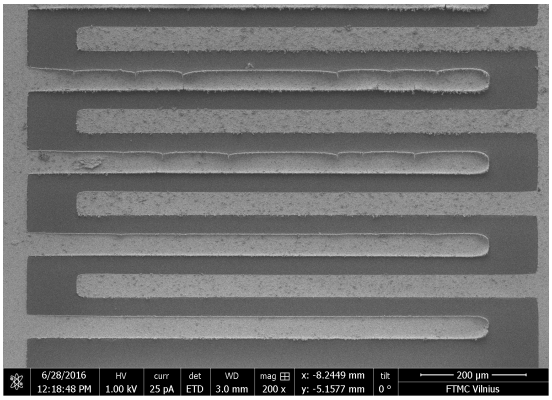

Fig. 3.5. *SEM image after Pt electroplating at 10 mVs^{-1} (comb on the left) and 50 mVs^{-1} (comb on the right) for 10 cycles, showing rough surface of electrode and even pealing off (comb on the left) at low scan rates.*

For the derivation of the surface roughness factor (R_f), the determined EASA of the Au surface was divided by the geometric area of the IDA. The obtained values of the R_f are described in Table. 3.1. After the Pt electroplating, the R_f of the electrode increased by 49.8 - 214.0 times, depending on the scan rate. Pt coating cracks were observed at a slow potential scan rate (10 mVs^{-1}) (Fig. 3.5) and even peeling off of the coating fabricated at 5 mVs^{-1} (not shown) . The observed cracks in the Pt coating can be also detected by increasing current values in the CVs at the Pt-plated electrode.

Table. 3.1. *R_f obtained after Pt electroplating at several scan rates.*

v, mVs^1	R_f
10	158.0 ± 7.0
50	214.0 ± 7.0
100	49.8 ± 0.8

High-resolution SEM images showed the difference in Pt structures deposited by applying different potential scan rates (Fig. 3.6). Homogeneous Pt twinning nanocrystals, with dimensions from 5 nm to 140 nm (in

the direction of long axis) were observed. Each crystallite had multiple twin lamellas, orientated perpendicular to the symmetry axis reported previously. The largest nanocrystals appeared in case of Pt plated at 50 mVs^{-1}, and it was selected as an optimal for further use.

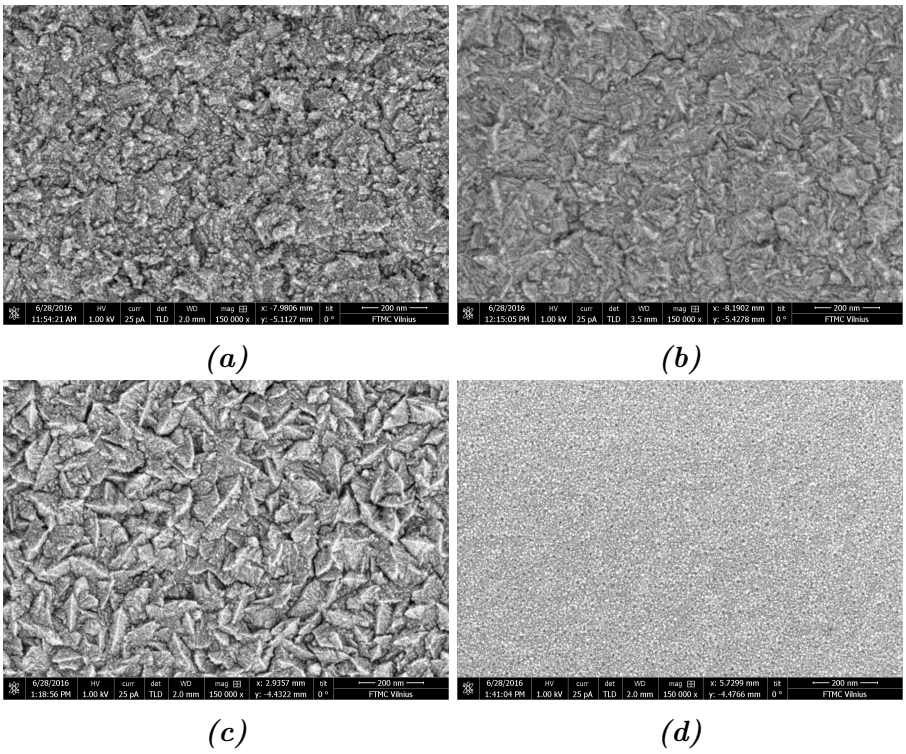

Fig. 3.6. *SEM images of Pt electroplated in potential window of 0.4 to 0.8 V vs. Ag/AgCl at 5 mVs^{-1} (a), 10 mVs^{-1} (b), 50 mVs^{-1} (c), 100 mVs^{-1} (d).*

For identification of elemental composition of Pt-coated IDA, EDS mapping was used. In Fig. 3.7, one of two combs electroplated by Pt at 50 mVs^{-1} is shown. The performed EDS mapping showed that Au was completely covered with Pt coating, with Pt amount of 96.9 % and low amount of O, C (summarised in Table. 3.2). Only, a small amount of Pt (4.2 %) was found on the comb that was not clipped for electroplating. In order to investigate sensing ability of obtained Pt microelectrode, H_2O_2 was used as analyte. The sensitivity of the fabricated Pt microelectrode to H_2O_2 was investigated electrochemically, and the results are presented in Fig. 3.8.

CVs at the Pt microelectrode in PB pH 7.3 was registered in absense (Fig. 3.8 (a), black line) and presence of various concentrations of H_2O_2. As seen in Fig. 3.8 (a), the CV at the bare Pt has a typical profile in

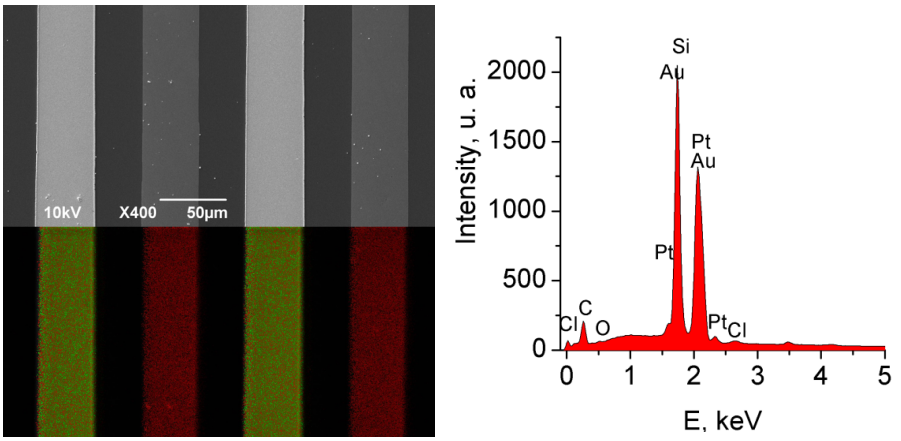

(a) *(b)*

Fig. 3.7. *EDS mapping of electroplated Pt on one of the combs (green) and non-modified comb (red), showing zoom in area of Au and Pt layers (a), EDX spectra, showing composition of elements (b).*

Table. 3.2. *Element weight and atomic mass obtained from EDS data in the area of Pt electroplated IDA, showing high amount of Pt of 93.55 %.*

Element	Weight %	Atomic %
C	3.68	36.93
O	0.53	3.97
Pt M	93.55	57.74
Au	2.24	1.37
Totals	100.00	

neutral pH [163]. Oxidation of H_2O_2 took place in the potential range from 0.4 to 0.8 V vs Ag/AgCl. Further addition of the analyte to buffer solution caused an increase in the oxidation and reduction current densities with increase in H_2O_2 concentration (Fig. 3.8 (a)). However, the increase in oxidation current density of 0.3 $mAcm^{-2}$ per 2 mM of H_2O_2 in the anodic region was lower compared to that of reduction current, i.e., 0.7 mA cm^{-2} for the same increase in the concentration of H_2O_2. The sensitivity to H_2O_2 in the CV mode was 0.23 and 0.34 mA cm^{-2} mM^{-1} for H_2O_2 oxidation and reduction regions, respectively. The difference in the sensitivities of the cathodic and anodic regions appear due to different electron transfer rate in oxidation and reduction rate of H_2O_2 determined by the influence of oxidation of Pt surface and reduction of the oxides formed, respectively. Additionally, calibration in the cathodic

and anodic regions was performed using chronoamperometry. Increase of response to H_2O_2 using chronoamperometry is shown in (Fig. 3.8 (b). It was found that the best sensitivity was at the potential of +0.35 V, especially for concentrations down to 20 M of H_2O_2, and this potential was chosen as optimal for further experiments.

A typical hydrodynamic chronoamperogram for various H_2O_2 concentrations is shown in Fig. 3.8 (b). As seen, the response was linearly proportional to H_2O_2 concentration. The response time was 5 s up to concentrations of 0.5 mM H_2O_2. The entire tested range of H_2O_2 concentrations spanned from 1 M to 6 mM (Fig. 3.8 (b) showed responses up to 2 mM because the range of the lower concentrations is more relevant for sensors applications. Inset in Fig. 3.8 (b) presents the calibration curve. In general, the linear H_2O_2 detection range was found to span two intervals from 1 to 8 M and from 10 µM to 6 mM, whereas the LOD value, calculated from calibration curve using 3 σ method (3 times standard deviation of the calibration curve divided from slope) was 21.7 nM, and the sensitivity of the Pt IDA microelectrode to H_2O_2 was 770 and 428 µA $cm^{-2}mM^{-1}$ (if normalised per electroactive are(a)) for the first and the second linear range, respectively. The majority of the existing works and all the works discussed below use normalise current per geometric area, in our case, it would be 2662 and 1443 $\mu Acm^{-2}mM^{-1}$, for each linear range, respectively. Comparing to other works the sensitivity was reported 2.70 $\mu Acm^{-2}mM^{-1}$ for Pt bulk electrode [64]. However, the formed nanostructured Pt microelectrodes were less sensitive than a Pt black microelectrode in a microfluidic system with a reported sensitivity of 6 $mAcm^{-2}mM^{-1}$ [80]. Moreover, Pt nanoparticles modified electrodes obtained in other way such as sputtering [169]. The attention should be paid to that EASA differs significantly from the geometric area, which is not always available from the reported data in the literature to the comparison of the sensitivity is not straightforward.

Therefore, LOD is a more convenient parameter for comparison with other reported electrode systems. Thus, for our Pt IDA microelectrode, the determined LOD was 21.7 nM. For comparison, for the first generation of glutamate biosensor based on Pt microelectrode array at 0.7 V (Ag/AgCl) (where H_2O_2 obtained during the enzymatic reaction was detected), the LOD was 790 nM [157]. Also, LOD = 4.5 µM at mesoporous Pt microelectrode was reported in [47], whereas Pt black electrodes yielded a LOD of 10 nM [121]. Thus, the Pt IDA microelectrode system described herein can be applied for detection of low concentrations of H_2O_2 and its electrochemical performance is close to that of Pt nanocrystalline structures [80, 48, 144]. At the same time, fabrication of such Pt nanostructure-enhanced microelectrodes is simple and reproducible,

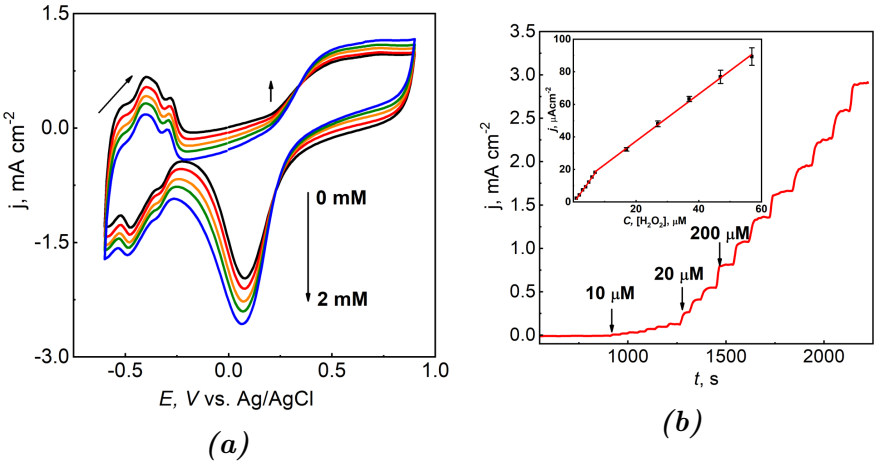

Fig. 3.8. *Sensing of H_2O_2 in physiological medium. CVs for increasing concentration of H_2O_2 (0 - 2 mM, step of 0.5 mM), at scan rate 50 mVs^{-1} (a), Chronoamperometry at 0.35 V vs. Ag/AgCl in dynamic range of H_2O_2 injections from 10 μM to 2 mM.*

compatible with other processes necessary for a microsystem development.

3.3 Design and characterisation of the miniaturised electrochemical cell

3.3.1 Sealing of interdigitated array

As a microband array was a region of interest, Au dedicated as a contact track was required to be masked. Several insulating materials were tested including hydrophobic pen, nail polish and PSA tape. As hydrophobic pen and nail polish were mechanically unstable, PSA was selected as an insulating layer and used in this work. The photograph of IDA electrode with formed PSA mask is shown in Fig. 3.9 (a), with zoom in area imaged by optical microscope showing overview of fabricated IDA including contact tracks, the remaining Au rectangular are isolated zones used for alignment of PDMS stamp. CVs in Fig. 3.9 (b) show electrochemical behaviour of Au in H_2SO_4 vs. Ag/AgCl, with cathodic peak at 0.815 $\pm$ 0.002 V. The electrochemical characteristics of 1^{st}, 2^{nd}, 3^{rd} contacts and geometrical area calculated from microscope image are summarised in Table. 3.3.

The 2^{nd} electrode has higher area (18 %) than the 1^{st} one, which can be explained by a higher number of microband arrays in the design

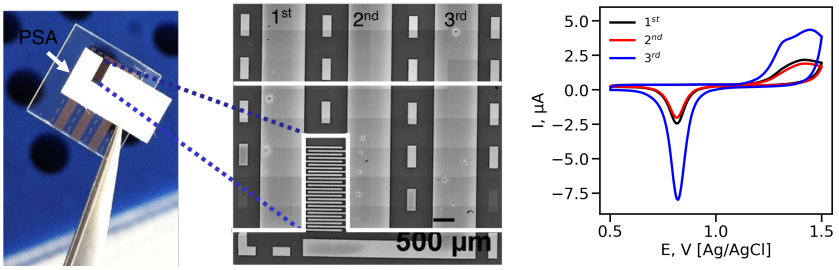

(a) *(b)*

Fig. 3.9. *Region of interest was sealed using PSA tape (a). Bright field microscope image, showing the region of interest for electrochemistry, 1^{st}, 2^{nd}, 3^{rd} contacts for clipping of electrodes. CVs in 10 mM H_2SO_4, with scan rate of 50 mVs^{-1}, where 1^{st}, 2^{nd}, 3^{rd} contacts clipped subsequently as a WE (b).*

Table. 3.3. *Values of geometrical area of electrodes (evaluated from microscope image) and electrochemical parameters from CV in 10 mM H_2SO_4. Error calculated as 1 STDEV.*

	A, cm^2	i_{pc}, µA	Q, µC	E, V
1^{st}	4.61 ± 0.08 x 10^{-3}	2.60 ± 0.09	5.71 ± 0.04	0.815 ± 0.002
2^{nd}	4.32 ± 0.06 x 10^{-3}	2.25 ± 0.013	4.73 ± 0.07	0.815 ± 0.001
3^{rd}	13.2 ± 0.2 x 10^{-3}	7.817 ± 0.29	16.46 ± 0.15	0.815 ± 0.002

of IDA electrode. The 3^{nd} electrode has larger geometrical area exposed to electrochemical solution (seen from microscope overview marked zone Fig. 3.9 (a)) leading to higher values of total charge (16.46 ± 0.15), calculated from integrated area under cathodic peak from Fig. 3.9 (b). The total charge was calculated, after the sealing of electrodes with PSA from several measurements with a minimal standard error of 1% (1 STDEV).

3.3.2 Design and configuration of interdigitated electrochemical cell

In this work several different electrochemical cells described in Experimental section were used. Different potential scan rates in 1 mM FcMeOH in 0.1 M PB were measured for WE with external CE (Fig. 3.10 (a)) and WE with internal interdigitated CE (b) systems. Fig. 3.10 shows linear increase of i_{pa} and i_{pc} withing the square root of the scan rate (from 5 to 200 mVs^{-1}) demonstrating diffusion controlled process [147]. The slope of the current vs. potential scan rate for WE only and WE-CE interdigitted

in Fig. 3.10 (c) and (d)) respectively is shown. For WE only, the slope values were of $0.0741\,\mu A(Vs^{-1})^{-1/2}$ and $-0.0371\,\mu A(Vs^{-1})^{-1/2}$, with R^2 of 0.998 and 0.969 for i_{pa} and i_{pc}, respectively.

$$i_p = 0.4463\ nFAC\left(\frac{nFvD}{RT}\right)^{\frac{1}{2}} \tag{3.2}$$

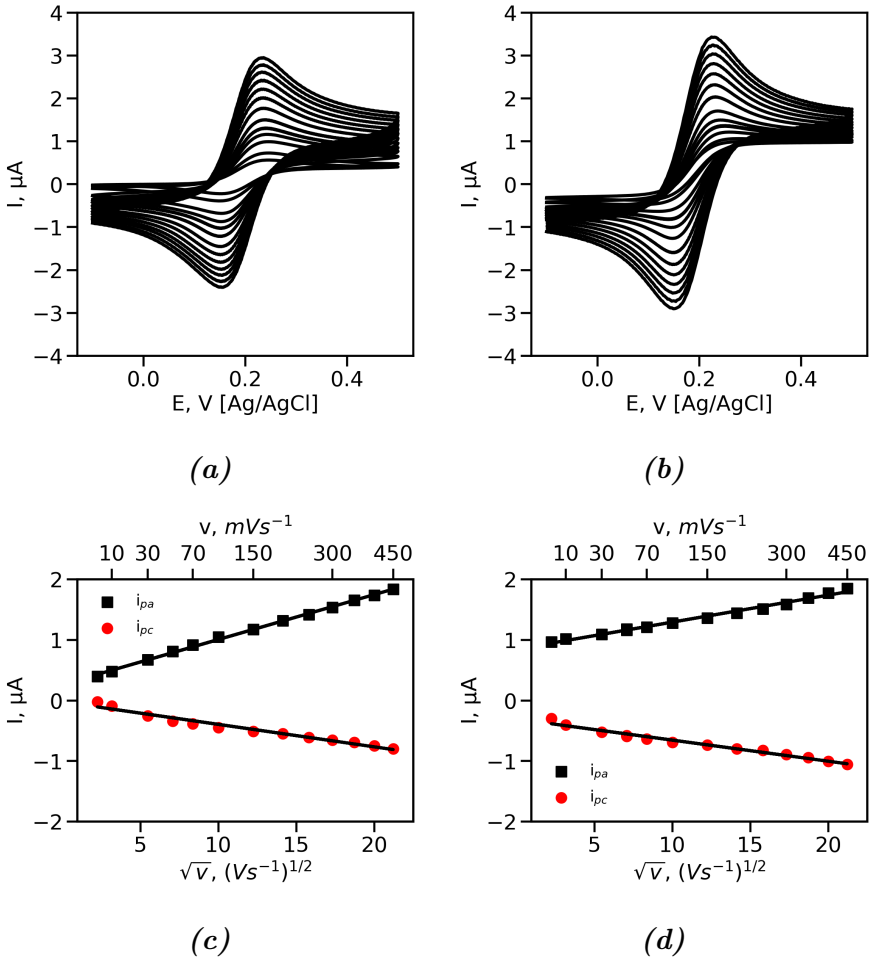

Fig. 3.10. *CV of oxidation and reduction of 1 mM FcMeOH at different scan rates from 5 mVs^{-1} to 450 mVs^{-1} for WE only (a) and interdigitated WE/CE (b). The dependence of current on square root of the scan rate for WE only (c) and interdigitated WE/CE (d). Error bar is smaller than data symbol.*

For the WE-CE configuration, the slope values were of $0.0445\,\mu A(Vs^{-1})^{-1/2}$ and $-0.0348\,\mu A(Vs^{-1})^{-1/2}$, with R^2 of 0.989 and 0.976 for i_{pa} and i_{pc},

respectively. The diffusion coefficient of FcMeOH was calculated using Randless-Sevcick equation (3.2) giving comparable to literature value of 2.002×10^{-7} cm^2s^{-1} [88], which was used later for CV simulation.

3.4 Simulation of diffusion and comparison with experimental

The electrochemical response of a microelectrode array, most commonly assessed via CV, depends on the geometry and the diffusional transport of the electroactive species to the electrode surface. Unfortunately, transport of an active redox species to the microelectrode is complicated, with overlapping of spherical diffusion fields leading to linear diffusion profiles at lower potential scan rates. An understanding of the complex mass transport can be drawn from finite element simulation.

3.4.1 Simulation Model

A simulation of the CV response for WE only and WE/CE integrated microelectrode arrays (in Fig. 3.11) at different potential scan rates were constructed.

The diffusion transport of the FcMeOH redox species to the working and counter electrode array was simulated. Diffusion transport was described by the Fick's second equation:

$$\frac{dc_i}{dt} = D_i \bigtriangledown^2 c_i \tag{3.3}$$

where c_i is the concentration of species i (either neutral ferrocene (F_c) or oxidised $F_c{}^+$) and D_i is the diffusion coefficient for species i, which was set to 2.002×10^{-7} cm^2s^{-1} [88] for both species and initial concentration of F_c was 1 mM and for $F_c{}^+$ was 0 mM.

The simulation was carried out using a 2D geometry as shown in Fig. 3.11, using the lateral symmetry along the 900 µm digits of the interdigitated electrode to minimise the simulation computing time and a reflectional symmetry to further reduce the simulation domain to the one shown in Fig. 3.11.

The oxidation and reduction of the ferrocene redox couple at both the working electrode and counter electrode were described using the Butler-Volmer equation:

$$J_{Fc+} = c_{Fc} k_0 e^{\left((1-\alpha)\frac{zF}{RT}\eta\right)} - c_{Fc+} k_0 e^{\left(-\alpha\frac{zF}{RT}\eta\right)} \tag{3.4}$$

Where η is the activation overpotential (defined as η =E - E_{eq}). E_{eq} was set as 0 V. Temperature was set as 300 K, $\alpha = 0.5$, k_0 was set to 5 cm/s to simulate the fast kinetics of the $F_c/F_c{}^+$ redox couple, z = +1, and F is the Faraday's constant. On the CE we only consider the reduction of F_c and so set the potential on the Au counter electrode as E= -0.3 V, which was estimated from empirical data. The other boundaries of the

simulation domain were set to either the bulk concentration (labelled as C^*. In Fig. 3.11, $C_{Fc} = 1$ mM, $C_{Fc+} = 0$ mM), a symmetry boundary (labeled as symmetry in Fig. 3.11), or no flux boundaries ($\partial C/\partial y = 0$ in Fig. 3.11).

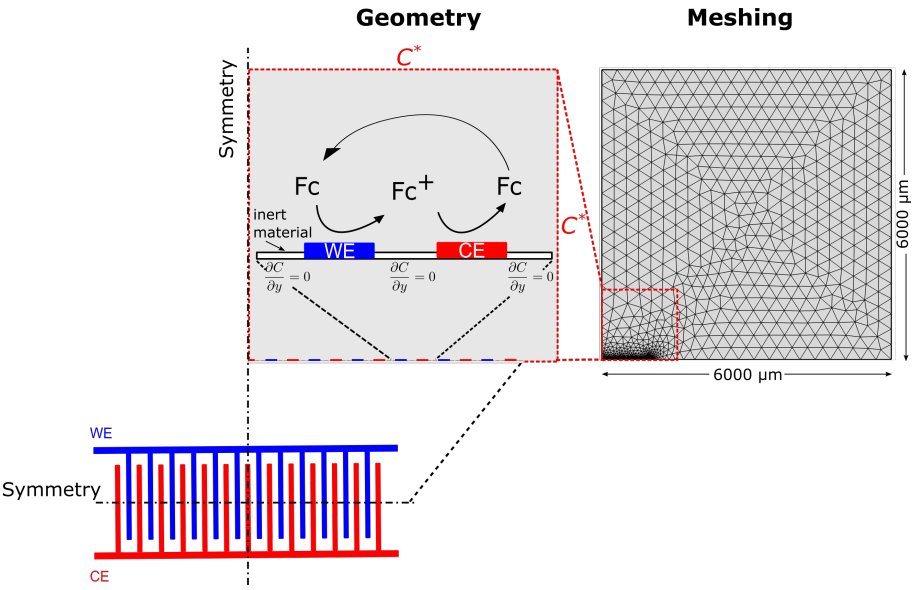

Fig. 3.11. *Schematic view of the model obtained for simulation including design of geometry, height and width domain, meshing and boundary conditions for the diffusion of 1 mM FcMeOH.*

The domain meshed with triangular elements, and the simulations of CV and concentration profiles have been optimised until no changes occurred in simulated CV and concentration profiles with an increase in the number of mesh elements. The number of elements was optimised to have high-resolution mesh, especially on the edges of IDA electrode, where the number of elements was required to be 12000. The current was calculated integrating diffusive flux of FcMeOH over WE, and multiplying by two times the length of the microelectrode band (2×900 µm).

3.4.2 Comparison of experimental data with simulation

For comparison of expermental and simulated values, steady state currents from experimental and simulated CVs were plotted and the matching values are shown in Fig. 3.12 (a). Divergence between WE only and WE/CE is observed below 100 mVs^{-1} in both experiment and simulation, with expectation of 2 times higher current at low potential scan rates in both our experimental data and our simulations. However, at the higher

potential scan rates, the current values between the two configurations match. This effect can be understood by considering the concentration profiles Fig. 3.12 (b) for both experimental configurations.

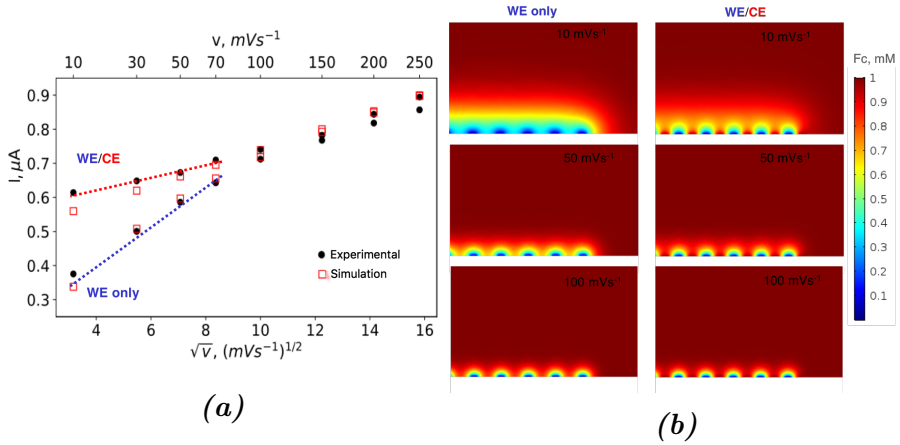

Fig. 3.12. *Plot of steady-state current at 0.3 V for the experimental and simulations for a range of potential scan rates in the two experimental configurations, WE only and WE/CE interdigitated. (a) Fc concentration profiles at three different potential scan rates in both the WE only and WE/CE configurations, showing a total overlapping of diffusion from interdigitated electrodes at low potential scan rates for WE only and partial stooped overlapping for WE/CE interdigitated electrodes at low potential scan rate (b).*

Concentration profiles at 10, 50 and 100 mV s^{-1} at E = 0.3 V are shown in Fig. 3.12 (b). It can be observed from the 2D diffusion profiles that during ferrocene oxidation at the WE the interdigitated CE (set at E=0.25 V) provided a sink (a location for the reduction of oxidised ferrocene) and reduced the overlap of the diffusion profiles from adjacent parts of the WE. This sink effectively stopped diffusional overlap occurring between different digits of the working electrode and prevented a linear diffusion profile developing. At the lower potential scan rates, it was enough time to elapse for the diffusion profiles to overlap and therefore for a difference between WE only and WE/CE to be observed. At the faster potential scan rates (>100 mVs^{-1}), not enough time passed during the CV for diffusional overlap to occur and therefore we do not observe the difference between WE only and WE/CE configurations. Interdigitating the CE with WE effectively increase the flux (measured as an increase in current) of redox species to the WE surface. An interdigitated electrode configuration the size of the diffusion layer is reduced, preventing the generation of a linear diffusion profile. The effect of the integrated

CE regenerating the redox species and suppressing diffusional overlap between different digits of the WE array can be expected to increase the sensitivity for an interdigitated electrode that relies on the interaction of Fc with the target species. As such, this unusual configuration might be employed for interdigitated electrode design, effectively making use of the CE, typically located far away from the working electrode surface to increase mass transport to the working electrode and prevent diffusion overlap from the different digits of the working electrode.

3.5 Characterisation of Au as pseudoreference and sensing of ferrocene

Nevertheless, Ag/AgCl is mostly used as the reference electrode in biosensors; it was reported that some inaccuracies leading to low reproducibility in measurements of reference potential might occur [44].

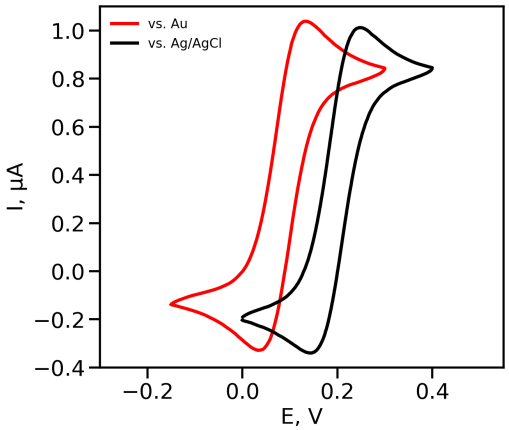

Fig. 3.13. *CV of interdigitated WE and CE measured in 1 mM FcMeOH in 10 mM PB, at 50 mVs^{-1} vs. Ag/AgCl and Au reference electrodes, giving a negative shift by -100 mV.*

To simplify fabrication of electrochemical cell, the fabricated IDA was design as three electrode electrochemical cell: 1^{st}- WE, 2^{nd}- CE and 3^{rd}- RE electrodes (Fig. 2.3 (e)). Avoiding, extra modification step, the Au (3rd electrode) was considered as pseudoreference electrode. Au was chosen, due to its simplified single-stage 3 electrode system fabrication, its possibility to use of ultra-thin electrodes, its strong biocompatibility, Au relatively stable reference potential and environmental durability reported previously [54, 81, 158, 170]. In Fig. 3.13, CV measured vs. Ag/AgCl

and Au pseudoreference electrode show potential shift to lower values by 100 mV.

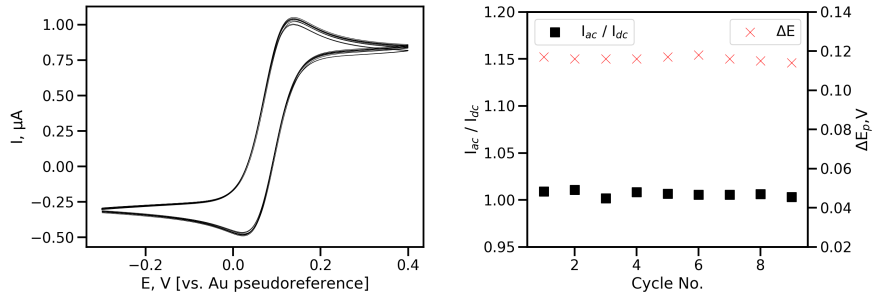

(a) ***(b)***

Fig. 3.14. *CV of Au/Au/Au system in 1 mM FcMeOH in 10 mM PBS, at 50 mVs^{-1} for 9 measurements (a). The ratio of anodic (i_{pa}) and cathodic (i_{pc}) current at steady state current and peak to peak separation ΔE_p over several scans showing good stability in 5 µL droplet (b).*

The stability of Au as pseudo reference electrode was evaluated by comparing at least 9 repeated measurements of CV (Fig. 3.14 (a)) in 5 µL of 10 mM PBS solution containing 1 mM FcMeOH. The average of peak to peak separation ΔE_p was 116 ± 1.2 mV demonstrating quasi reversible system, where the i_{pa}/i_{pc} was 1.006 ± 0.003. The standard deviation of cathodic and anodic currents and potentials, calculated from 9 measurements was less than 1%. The stability of Au pseudoelectrode was with a variation of ΔE_p of only 1 %.

As for the characterisation of interdigitated, WE and CE showed predictable higher sensitivity up to 2 times in experimental and simulated values of steady currents at low potential scan rates; FcMeOH was studied as a model system to prove the concept.

Table. 3.4. *Slope values representing sensitivity to FcMeOH at the potential scan rates of 50 mVs^{-1} and 5 mVs^{-1}. Error calculated as 1 STDEV from 3 measurements of the same concentration.*

	Slope, $nA\mu M^{-1}$		LOD, μM^{-1}	
	i_{pa}	i_{pc}	i_{pa}	i_{pc}
50 mVs^{-1}	0.718 ± 0.005	-0.283 ± 0.004	32	74
5 mVs^{-1}	0.851 ± 0.008	-0.498 ± 0.011	24	51

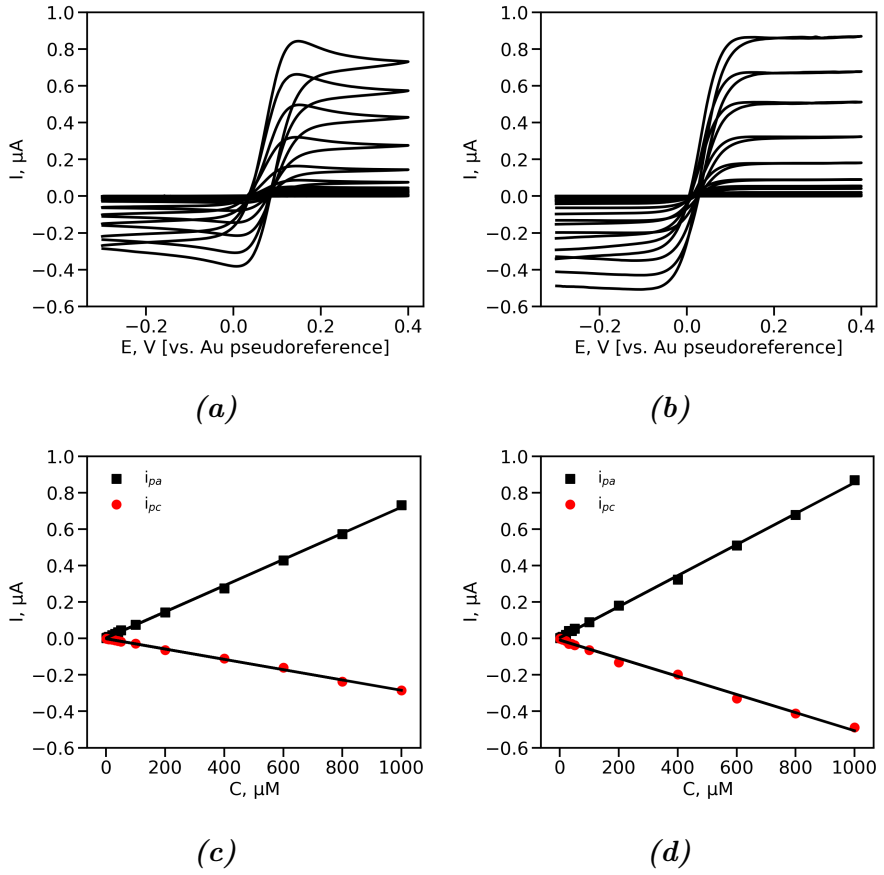

Fig. 3.15. *CV of oxidation and reduction of FcMeOH in dynamic range from* 0.5 µ*M to* 1000 µ*M at 50 mVs*$^{-1}$ *(a) 5 mVs*$^{-1}$ *(b). Calibration curves obtained at steady state* i_{pa} *and* i_{pc} *current from 50 mVs*$^{-1}$ *(c) and 5 mVs*$^{-1}$ *(d).*

Electrochemical detection of FcMeOH using CV in a wide range of concentrations from 0.5 µM to 1000 µM (supported by 10 mM) PB at higher (50 mVs^{-1}) and lower (5 mVs^{-1}) potential scan rates was studied. The values of anodic and cathodic currents in CV increased, with increased concentration of redox-active molecules, as shown in Fig. 3.15 (a), (b). When the potential scan rate was low (5 mVs^{-1}), the steady-state currents were obtained showing the domination of spherical diffusion. Also, the value of steady-state current was much higher than the one obtained at a higher potential scan rate. Calibration curves were obtained, at the steady-state current at -0.3 V and 0.4 V with increase of concentration is shown in Fig. 3.15(c), (d). Interestingly, the anodic current increased much faster than the cathodic one with the increase in concentration,

with the $R^2 = 0.999$ for i_{pa} and i_{pc} $R^2 = 0.998$.

The slope of the current vs. concentration representing sensitivity measured at 50 mVs^{-1} and 5 mVs^{-1} (Fig. 3.15 (c), (d)) and LOD are sumarised in Table. 3.4. At 50 mVs^{-1}, the sensitivity calculated from slope of signal vs. concentration was of $0.718\,nA\mu M^{-1}$ and $-0.283\,nA\mu M^{-1}$, with R^2 of 0.999 and 0.998 calculated for i_{pa} and i_{pc}, respectively. At 5 mVs^{-1}, the slope was higher giving values of sensitivity of $0.851\,nA\mu M^{-1}$ and $-0.498\,nA\mu M^{-1}$, with R^2 of 0.999 and 0.995 for i_{pa} and i_{pc}, respectively. Comparing LOD, the lower values for higher slopes were obtained reaching 32 μM^{-1} and 24 μM^{-1} for 50 mVs^{-1} and 5 mVs^{-1}, respectively. The obtained highest sensitivity ($0.851\,nA\mu M^{-1}$) for $5mVs^{-1}$ was 1.6 times higher than the highest reported in literature ($0.547\,nA\mu M^{-1}$ and $0.521\,nA\mu M^{-1}$)[170].

The sensitivity to FcMeOH was higher, when sensing at low potential scan rate (5 mVs^{-1}), with approximately 18 % and 75 % for i_{pa} and i_{pc}, accordingly. Also, LOD was 31-33 % lower when scanned at 5 mVs^{-1}.

3.6 Sensing of carcinoma antigen 125 using surface plasmon resonanse

For sensing of CA125, antibody anti-CA125 was used. To have covalent immobilisation of anti-CA125 SAM was formed as described in subsection 2.3.3. The -COOH groups were activated by using NHS/EDC crosslinker. The anti-CA125 was attached using µCP. Several incubation times of 5, 10, 20 and 40 min of anti-CA125 diluted in 0.1 M PBS on structured hydrophobic PDMS stamp was investigated. After 5 or 10 min incubation, the stamp was still hydrophobic and after 20 min inking, PDMS stamp became hydrophilic meaning that the antibody physisorbed on PDMS stamp. Longer incubation for 40 min did not give any changes, shorter time of 20 min was chosen as optimised. The rest of anti-CA125 was collected from PDMS stamp and reused for repeatable procedures of µCP. After inking the PDMS stamp was gently dried with N_2 and placed on NHS/EDC activated SAM. The contact time between PDMS stamp and SAM was investigated having 5, 10, 20 and 40 min. It was observed that at short contact times 5 - 10 min the coverage of the protein layer was not homogenoius and after 20 min of µCP pattern with 50 µm lines was formed and no longer times where needed. The main advantage of µCP was the ability to pattern substrates with antibody, without losing high amounts of the ink itself. The coverage of anti-CA125 was studied using Imaging ellipsometer.

3.6.1 Investigation of surface coverage by antibody

Ellipsometry Imaging (EI) was used to investigate the antibody coverage on the substrate. The height mapping of patterned anti-CA125 is shown in Fig. 3.16. The average surface coverage by anti-CA125 calculated as 3.79 ± 0.54 nm (estimated from 7 different zones) similar to values of proteins coverage reported previously [164, 126].

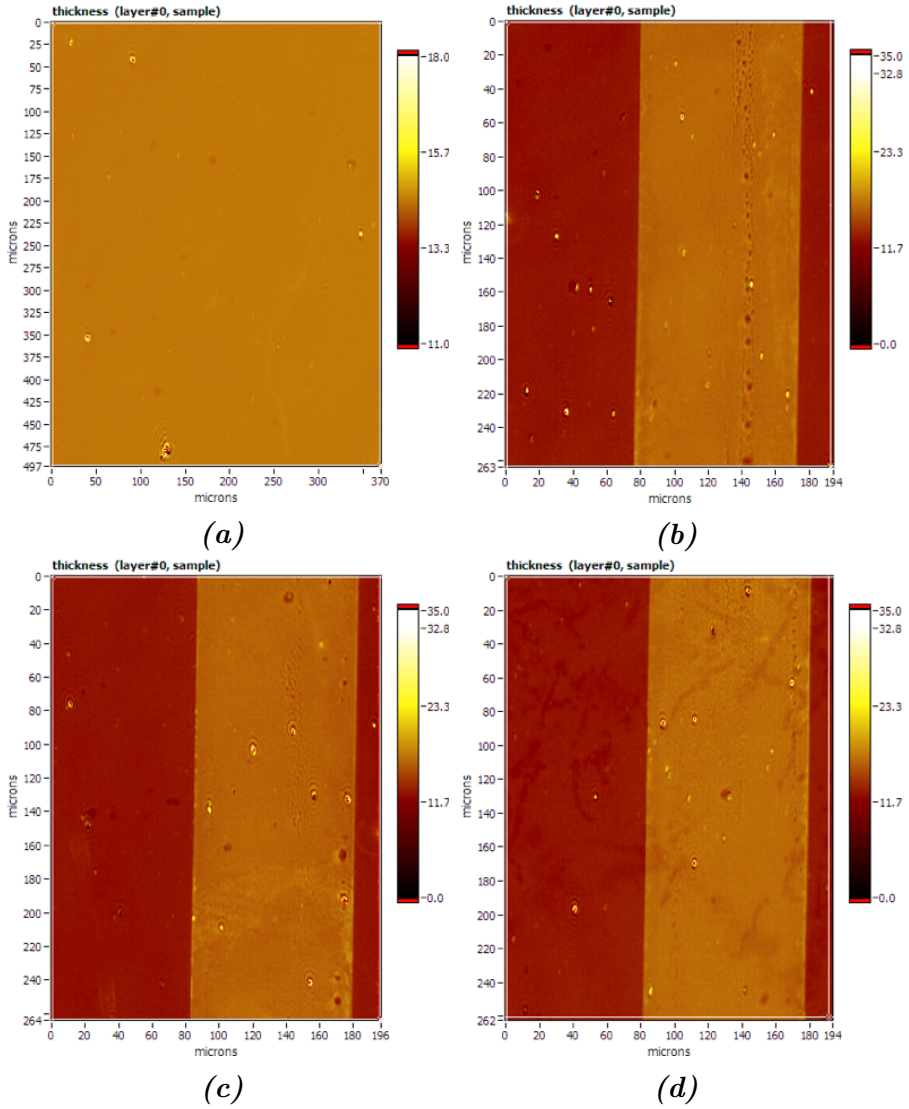

Fig. 3.16. *Height mapping before (a) and after anti-CA125 patterned on substrate by μCP in several areas (zones within 500 μm distance in between, were analysed) on 1x1 cm printed area (b), (c), (d), height scale-bar is in nm.*

3.6.2 Real time detection of carcinoma antigen 125

The substrate after µCP of anti-CA125 was blocked with 2% of BSA subsection 2.5.2. In Fig. 3.17, the kinetic of BSA non-specific binding and CA125 specific binding are shown. Two zones with and without antibody were compared for binding of CA125. The signal increase after CA125 injection was distinct. Some non-specific binding of CA125 was present possibly caused by the negatively charged substrate. The relative response (RR% = 100 % × (Signal-blank)/blank) was calculated and values for two interfaces compared, showing 40 % higher signal for anti-CA125 interface than for BSA interface.

3.6.3 Specificity to carcinoma antigen 125

The interactions of anti-CA125 and CA125 were studied by SPR. First of all, the SPR substrate was functionalised with SAM of carboxyalkyl thiols on which anti-CA125 was attached via amide bond using microcontact printing. To form a mixed self-assembled monolayer of carboxyl- terminated alkanethiols, the SPR Au chips were washed once in n-Hexan and sonicated in distilled ethanol for 5 min. Subsequently, the substrates were immersed overnight in 40 µM solution consisted of of 70 % HS−EG_3OH and 30 % of HS−EG_6−COOH. The SPR substrate was subsequently ultrasonicated for 3 seconds in purified ethanol and rinsed with water and gently dried in N_2 stream before immobilisation of antibodies on the surface. Carboxylic terminal groups were activated with a mixture of 2.5 mM NHS and 10 mM EDC in ethanol for 30 min. In parallel, 500 µL of 1:100 diluted in 0.1 M PBS anti-CA125 (150 mM NaCl added freshly before dilution) was incubated as an ink on PDMS stamp with 200 µm lines and 200 µm gaps for 20 min and the solution of antibodies was collected for further use. After incubation, PDMS stamp was dried with gentle N_2 stream and placed on SPR chip for 10 min. Any, active carboxy- groups on the chip were blocked with 0.5 % BSA. Subsequently, the sensor was placed to the SPR cell.

The non-specific binding signal of BSA and specific of CA125 was 3.5 times lower than specific CA125 binding (Fig. 3.17 (b)), which is optimal for sensing applications.

3.7 Sensing of carcinoma antigen 125 on interdigitated electrodes

The sensor for CA125 was fabricated as described in experimental section 2.5. The CV of Au IDA electrode in 1 mM FcMeOH before and after

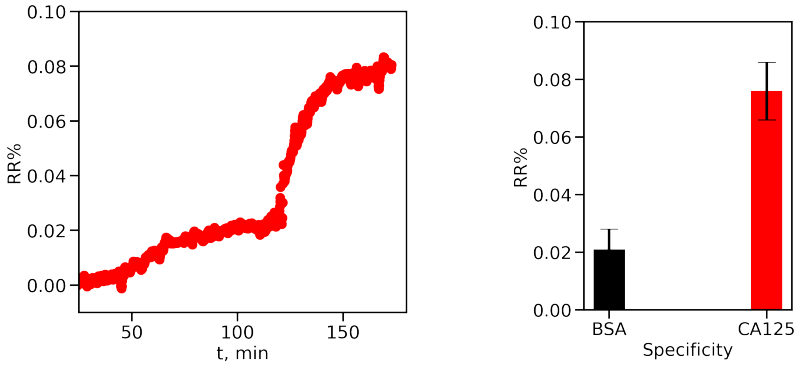

(a) *(b)*

Fig. 3.17. *SPR kinetic (step 0.5 s) during non-specific BSA binding (from 40 to 120 min) and specific binding of 50 μgmL^{-1} of CA125 (from 120 to 170 min) in 7.3 pH PB (the signal smooth to windowlength = 9, polyorder = 3) (a) Specificity of antibody to CA125, RR% = 100 % × (δ-δ_{blank})/δ_{blank} (b), errorbar calculated as 1 STDEV.*

SAM formation is shown in Fig. 3.18. After SAM formation, the anodic peak was suppressed by 40 % and shifted to higher potential, i.e. 300 mV. Cathodic peak almost disappeared, showing that Au surface is not available for electron transfer caused by SAM formed on IDA (Fig. 3.18). Also, the peak to peak separation in CV increased, demonstrating slow electron charge transfer similar to reported previously [7].

Subsequently, anti-CA125 was immobilised as described in subsection 2.5.2 and the sensor calibrated for CA125. As CV was not sensitive for antigen concentration changes, EIS was used for sensing of CA125. EIS method has been reported in literature as having an inherent ability to sensitively control the characteristics of conductivity, steric, dielectric or charging potential at an electrode / electrolyte interface [23, 22, 49]. When the surface was changed by Anti-CA125 and IDA was immersed in electrolyte, an electrical double layer was formed. EIS were recorded and ploted as a Nyquist plot, which is typically performed inside a Randles-equivalent circuit scheme. As sometimes it is difficult to find equivalent circuit giving acceptable fitting, two types of data analysis methodologies: classical fitting of R_{ct} and Immittance function analysis by screening slope, LOD and R^2 values were used.

Electrochemical detection of CA125 using EIS in a dynamic range of concentrations from 0.4 μgmL^{-1} to 3 μgmL^{-1} was studied. As seen in Fig. 3.19 (a), almost ideal semicircle was obtained indicating that the SAM was well packed on Au IDA. The signal of electrochemical imped-

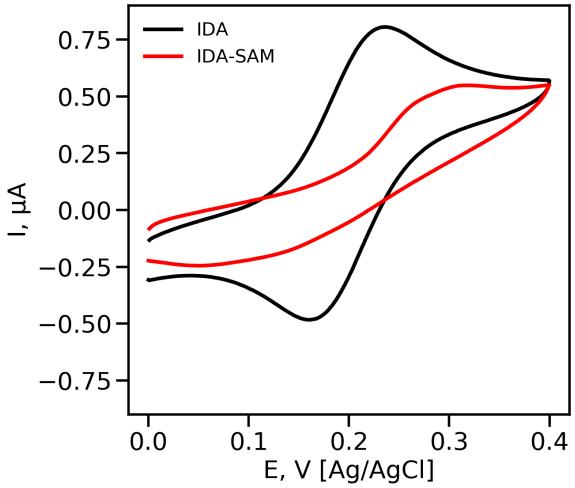

Fig. 3.18. *CV of IDA in WE/CE interdigitated configuration after SAM formation, scan rate 50 mVs^{-1}, in 1 mM FcMeOH, supported by 0.1 M PB.*

ance increased - with the increased of the concentration of CA125 as shown in Fig. 3.19 demonstrating slower charge transfer within the adsorption of CA125. The diameter of semicircle (R_{ct}) increased from 26.3 kΩ to 49.9 kΩ with the increase of CA125 from 0 to 3 µgmL^{-1} (Fig. 3.19 (a)). In $Z^{'}$ ploted vs frequency (Fig. 3.19 (b), the values of $Z^{'}$ at low frequencies increased from 35.2 to 53.5 kΩ with increased concentration of CA125, which are similar resistance values obtained from R_{ct}. It has been reported in literature that $Z^{'}$ vs frequency can be linked to R_{ct} value if steady state values at low frequencies are reached [23]. In Fig. 3.19 (c) $Z^{''}$ vs frequency is plotted, showing increase of the maximum of the peak value with increased concentration of CA125. The position of obtained peak frequency (23.82 ± 2.2 Hz) is related to time constant of the system. As the time constant doesn't change with increase concentration of CA125, the immitance analysis can be applied.

Nyquist (Fig. 3.19 (a)) and $Z^{'}$ and $Z^{''}$ plots vs. frequency (Fig. 3.19 (b), (c)) were analysed using several methods including Nyquist fitting to equivalent circuit and immittance analysis for single frequency analysis. In the Fig. 3.20 (a), (b) the dependence of RR% vs. amount of CA125 reflecting sensitivity of biosensor is shown. The RR% of 90 % was obtained when RR% was calculated from R_{ct} values (Fig. 3.20 (a)). The RR% of 160 % was obtained when RR% was calculated from the maximum of the peak of $Z^{''}$ (Fig. 3.20 (b)), with almost two times higher slope (58.56

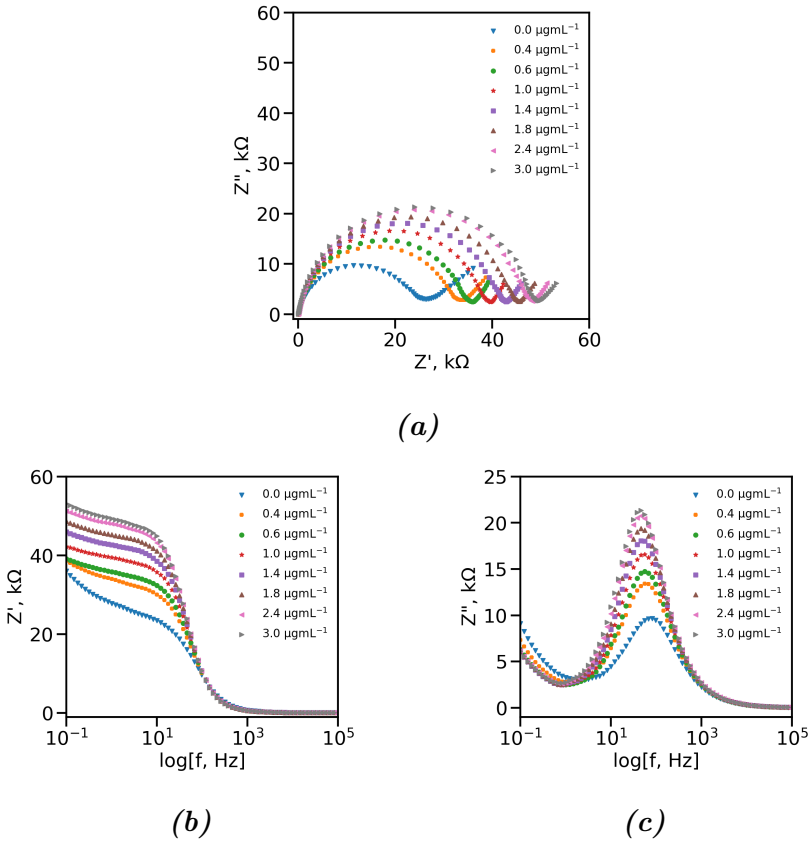

Fig. 3.19. *Increase of the signal in electrochemical impedance plots after sensor exposure to several concentrations of CA125, Nyquist plots (a), plot vs. frequency of $Z^{'}$ (b), $Z^{''}$ (c), measured from 100,000 Hz to 0.1 Hz at 10 mV amplitude, DC voltage at OCP.*

RR%/µgmL^{-1}) value in comparison to slope (32.32 RR%/µgmL^{-1}) calculated from R_{ct}. The LOD was compared for several methodologies of data analysis and calculated using eq. 3.5, where σ - residual standard deviation of the linear regression [35]. When plot of RR% calculated using R_{ct} value vs concentration was used, the LOD with lowest value of 1.23 µgmL^{-1} was obtained.

$$LOD = \frac{3 \times \sigma}{Slope} \tag{3.5}$$

For comparison LOD value obtained from the maximum of the $Z^{''}$ peak was 1.31 µgmL^{-1}, which is 6 % higher. Additionally, LOD was analysed from $Z^{'}$ and $Z^{''}$ plots vs. frequency (Fig. 3.19 (b), (c)). The frequencies were selected between 0 - 100 Hz and only having the best linear response

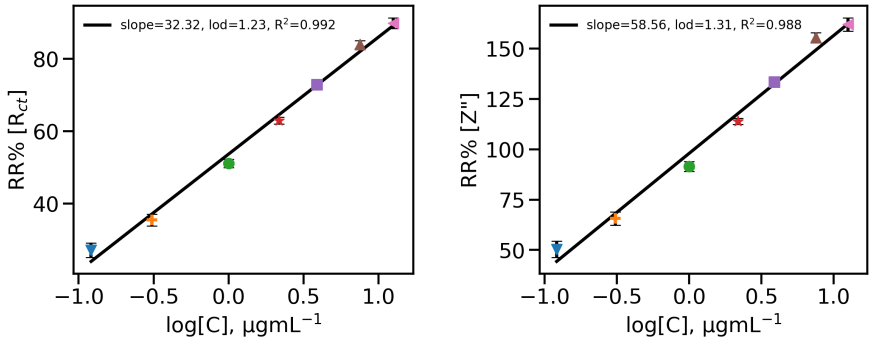

(a) ***(b)***

Fig. 3.20. *Calibration curves, where slope obtained from R_{ct} fitted data to Randles equivalent circuit (a), the maximum of Z'' vs frequency plot (b).*

(R^2>0.900). The RR% obtained from Z' and Z'' plots at several selected frequencies vs concentration of CA125 are shown in Fig. 3.21 (a) and (b) respectively.

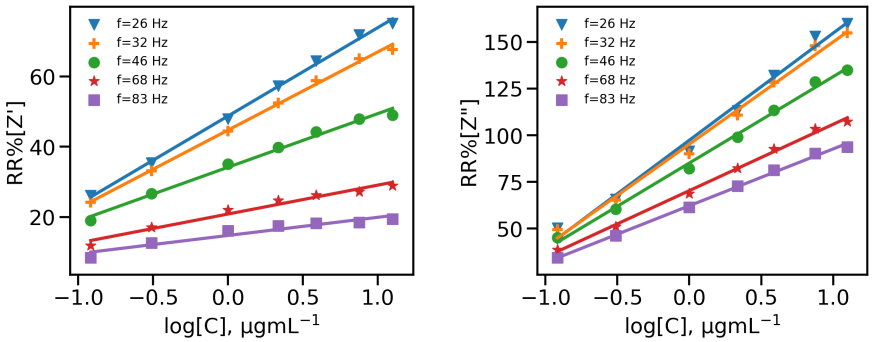

(a) ***(b)***

Fig. 3.21. *Calibration curves obtained at selected frequencies from plot vs. frequency of Z' (a) and Z'' (b).*

Slope, LOD and R^2 obtained at several frequencies (26.1, 31.6, 46.4, 68.1, 82.5 Hz) from Z' are summarised in Table. 3.5, with obtained sensitivity from 5.1 ± 0.7 to 25.1 ± 0.6 RR%/µgmL^{-1} and LOD from 2.03 (at 82.5 Hz) to 1.13 (at 26.1 Hz) µgmL^{-1}.

Slope, LOD obtained at the same frequencies (26.1, 31.6, 46.4, 68.1, 82.5 Hz) from Z'' are summarised in Table. 3.6, with obtained sensitivity

Table. 3.5. *Parameters from $Z^{'}$ EIS data for sensing of CA125 at several frequencies.*

f, Hz	Slope, RR%/µgmL^{-1}	LOD, µgmL^{-1}	R^2
26.1	25.1 ± 0.6	1.13	0.998
31.6	22.2 ± 0.5	1.14	0.997
46.4	15.2 ± 0.7	1.28	0.990
68.1	8.2 ± 0.6	1.52	0.971
82.5	5.1 ± 0.7	2.03	0.927

from 30.5 ± 0.7 (at 82.5 Hz) to 57.4 ± 2.6 RR%/µgmL^{-1} (at 26.1 Hz) and LOD from 1.25 µgmL^{-1} (at 31.2 Hz) to 1.13 µgmL^{-1} (at 82.5 Hz). This

Table. 3.6. *Parameters from $Z^{''}$ EIS data for sensing of CA125 at several frequencies.*

f, Hz	Slope, RR%/µgmL^{-1}	LOD, µgmL^{-1}	R^2
26.1	57.4 ± 2.6	1.24	0.989
31.2	54.8 ± 2.3	1.25	0.992
46.4	46.3 ± 1.3	1.17	0.996
68.1	35.5 ± 0.9	1.16	0.996
82.5	30.5 ± 0.7	1.13	0.997

data analysis method called immittance electroanalysis was discussed in literature for faradaic (redox probe amplified) and non-faradaic assays, where no equivalent circuit analysis is required [107, 15]. The immittance electroanalysis might lead to simplified methodology without required additional, time-consuming data fitting. Also, for some interfaces, semicircle in the Nyquist plot is not always ideal, leading to difficulties in selecting and modelling equivalent circuit. Plots vs. frequency might be better expressed, giving high sensitivity and lower LOD[108, 107]. The key feature of this strategy was to use EIS as a transition method to track interfacial activities without relying on pre-modelling it using equivalent cirquits.

In Fig. 3.22 and Fig. 3.23 for $Z^{'}$ and $Z^{''}$ respectively, we show the spectra of slope, LOD and R^2 values in a whole range of frequencies from 100,000 Hz to 0.1 Hz for CA125 sensing on IDA interface. In case of values obtained from $Z^{'}$ vs frequency plot, R^2 and slope values (Fig. 3.22 (a)) were optimal for sensing in lower range of frequencies from 26.1 to 82.5 Hz. As a result, LOD was lowest in the same frequency range (Fig. 3.22 (b)).

In higher frequencies (above 82.5 Hz) the slope was significantly lower (up to 0.4 RR%/µgmL^{-1} at its lowest), and R^2 also low and unstable throughout most of that range, resulting in less than optimal LOD,

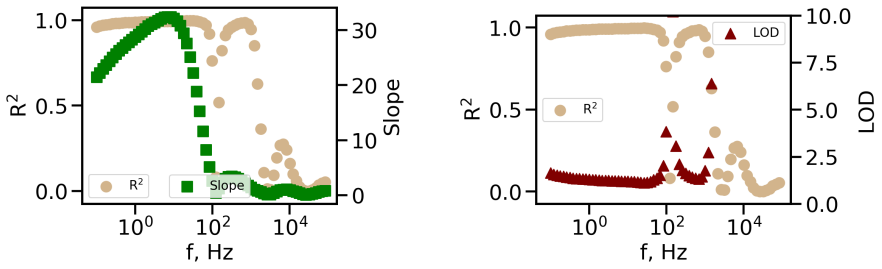

(a) *(b)*

Fig. 3.22. *Slope (a) and LOD (b) obtained from plot vs. frequency of $Z^{'}$, showing the ranges of frequencies for best values of LOD (and the R^2 = 0.991).*

and thus making $Z^{'}$ measurements not suitable for detection above 82.5 Hz frequency range. In case of values obtained from $Z^{''}$ vs frequency plot(Fig. 3.23(a)), R^2 and slope follow a different pattern. R^2 was close to 1.0 in higher frequency range of 12.1 - 82,520 Hz, although slope peaked at 26.1 Hz and was relatively high (above 30 RR%/µgmL^{-1}) only in 4.6 - 82.5 Hz range of frequencies (Fig. 3.23 (a)). Resulting LOD value on IDA interface was at its lowest in 12.1 - 82,520 Hz frequencies (Fig. 3.23 (b)), demonstrating that R^2 value has greater significance for LOD than slope. Although the lowest LOD was measured at 82.5 Hz (1.13 µgmL^{-1}), detection at higher frequencies could be more attractive in cases where faster measurement is needed and slightly higher LOD is still acceptable (e.g. 1001 Hz, LOD 1.24 µgmL^{-1}).

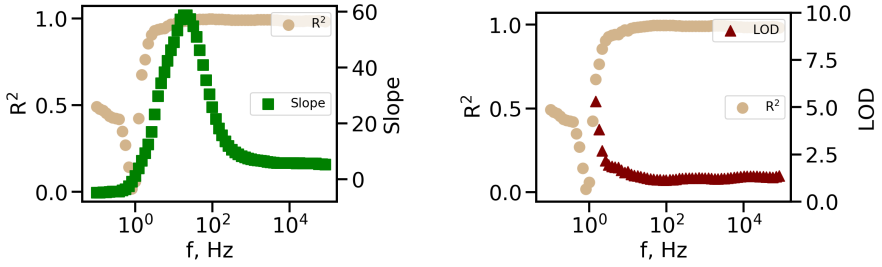

(a) *(b)*

Fig. 3.23. *Slope (a) and LOD (b) obtained from plot vs. frequency of $Z^{''}$, showing the ranges of frequencies for best values of LOD (and the R^2 = 0.991).*

The study specificity of fabricated sensor, the sensor was exposed to 200 µgmL^{-1} of BSA, HSA, FN and IgG selected as commonly used proteins for specificity test. After IDA/anti-CA125 exposure to non-specific proteins, the changes in RR% of 11 ± 2 % for BSA, 9 ± 1% for IgG, 12 ± 2 % for HSA, 16 ± 3 % for FN were obtained. After sensor exposure to 10 µgmL^{-1} of CA125, the change in signal reached almost 70 %, demonstrating successfully formed antibody-antigen complex causing high percentage change in signal. In literature, the RR% of almost 100 % was achieved for sensing of similar biomarker (MUC4) [65].

To sum up, once an appropriate frequency region is identified, acquisition and analysis time can be significantly reduced for CA125 analysis by measuring only at select frequencies, thus achieving superior assay sensitivity and LOD values equal to or better than those obtained based on using R_{ct} obtained from Nyquist plots as the analytical transducer signal.

3.8 Sensing of carcinoma antigen 125 on Au and Pt nano-structured electrodes

It has been reported that increased roughness factor of the working electrode can enhance the magnitude of the electrochemical response since more antibody can be immobilised for a given electrode area [140, 137, 95]. For this plane electrodes were electroplated by Au or Pt nanostructures to compare performance in electrochemical sensing.

No oxidation or reduction peaks are observed for the unmodified SPCE, suggesting that the SPCE electrode surface was mostly free of oxygen functionalities. This behaviour was typical for a carbon electrode that has not been exposed to oxidants but indicates a low number of sites that can covalently link to antibodies, e.g., by coupling the amines to the surface carboxyl groups.

The Fig. 3.24 shows voltammograms in 10 mM aqueous H_2SO_4 after electroplating with Au and Pt nanostructures. For the Au nanostructured electrodes typical hydrogen adsorbtion and desorbtion peaks were observed at 0.6 and 1.1 V respectively (Fig. 3.24 (a)). For the Pt electrodes, hydrogen adsorption and desorption peaks are observed in the potential range from -0.1 to 0.25 V (Fig. 3.24 (b)). Additionally, for both Au and Pt electrodes, peaks corresponding to the formation and subsequent reduction of metal oxide layers are observed in the potential range from 0.2 to 1.6 V. EASA for both Au and Pt electroplated nanostructures were estimated from the charge passed under the oxide reduction peaks at 0.6 V and 0.4 V for Au and Pt, respectively. The charges associated with the reduction of Au_2O_3 and PtO_2 monolayers were 440 mCcm^{-2} and 390

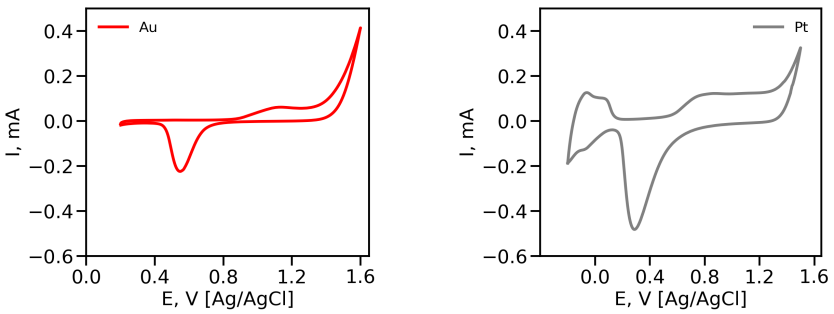

Fig. 3.24. *CVs of electrode after Au electroplating (a), Pt electroplating (b) in 10 mM H_2SO_4, at 100 mVs^{-1}.*

$mCcm^{-2}$, respectively. The total charges associated with the oxide reduction for the Au was 168 ± 11 mC and for Pt was 1300 ± 102 mC, corresponding to EASA of 0.382 ± 0.032 cm^2 and 3.250 ± 0.249 cm^2 for Au and Pt respectively. The Pt-modified electrodes showed 8.5 times greater EASA than that of Au.

Unmodified electrodes have a surface which was relatively smooth at the scalebar of 10 and 5 µm (Fig. 3.25 (a), (b)). In sharp contrast, the surface was strongly textured at a nano/micro-scale following the metal electroplating, consistent with the increase area in the surface found using CV. Fig. 3.25 (c), (d) displays electrode after deposition of Au and reveals micro-to-nano particle formation (566 ± 19 nm) separated by unmodified electrode regions. This morphology indicates that deposition continued from the initial nuclei forming on the surface of the electrode and was overgrowing to give continuous Au film. Fig. 3.25 (e), (f) shows that Pt nanoparticles were formed with a diameter of 141 ± 27 nm. The smaller size Pt nanoparticles were obtained possibly because Pt is much less easily oxidized and has higher surface energy than Au [141].

Fig. 3.26 shows Nyquist and plots vs. frequency in different concentrations of PB. The radius of the semicircle or max value in plot vs. frequency of $Z^{'}$ corresponds to the total cell resistance, i.e., the sum of the solution and electrode resistance decreases with increasing electrolyte concentration. The obtained values of the signal are summarised in Table. 3.7. 0.1 M PB buffer, with the lowest resistance (high ionic strength), was chosen for further analysis in immunosensor fabrication.

In order to obtain a more in-depth insight into the effect of metal functionalisation, voltammetry was recorded at higher potential scan rates so that the rate of heterogeneous electron transfer exerts a more con-

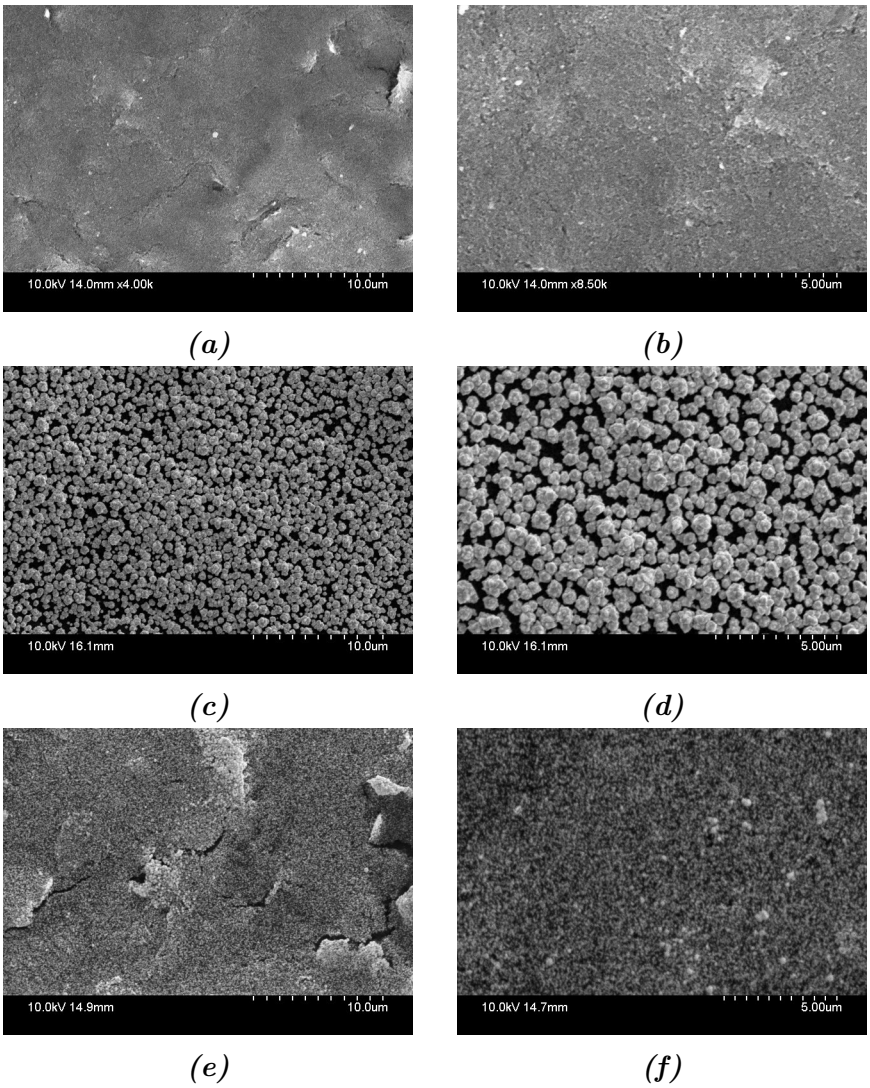

Fig. 3.25. *SEM images of bare SPCE (a), (b) Au electroplated from -0.8 V to 0.9 V, at 100 mVs^{-1} (c), (d) and Pt electroplated in potential window of 0.65 to 0.9 V at 100 mVs^{-1}, (e), (f) showing nano-particle structure.*

siderable influence over the observed response. Fig. 3.27 (a) shows the effect of changing the potential scan rate on the voltammetry of 5 mM $[Fe(CN_6)]^{3-/4-}$ at the carbon modified with Au nanostructures in 0.1 M PB buffer solution. The ratio of I_{pa} and I_{ca} was 0.958 ± 0.013 for all potential scan rates investigated, and the peak currents increased linearly with the square root of the potential scan rate Fig. 3.27 (b). At 100 mV

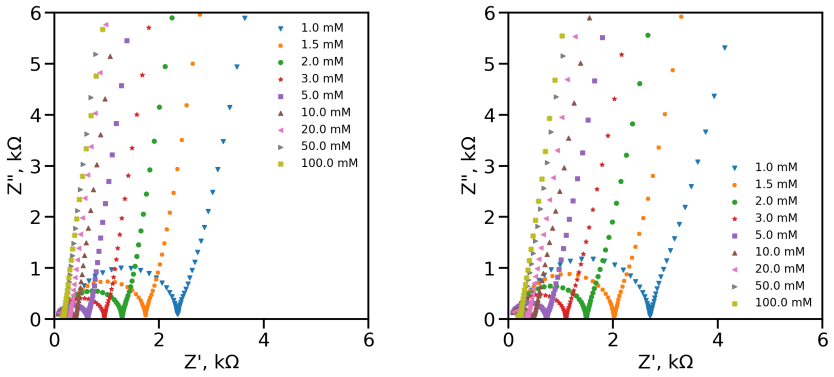

(a) *(b)*

Fig. 3.26. *Nyquist plots after exposure to several concentrations (different ionic strength) of PB using Au (a) and Pt (b) interfaces, measured from 100,000 Hz to 0.1 Hz at 10 mV amplitude, DC voltage at OCP.*

s^{-1} scan rate, peak to peak separation was 165 mV, significantly more significant than the 57 mV (expected for an ideally reversible couple). Moreover, despite the ohmic drop being negligible, △Ep increases with increasing potential scan rate. These observations are consistent with a quasi-reversible response that was influenced by the heterogeneous electron transfer dynamics and under semi-infinite linear diffusion control.

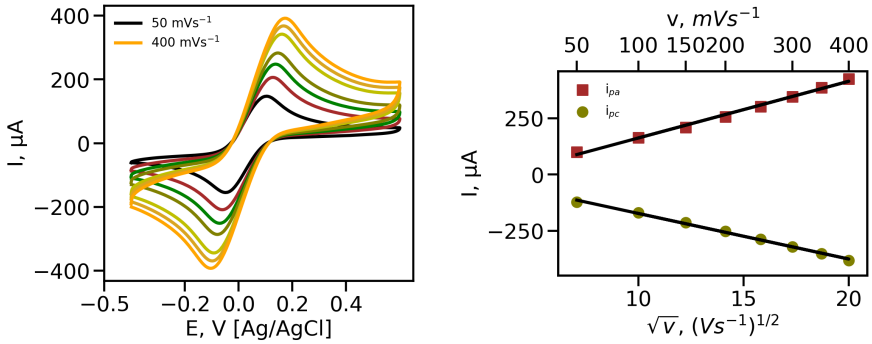

(a) *(b)*

Fig. 3.27. *CV at different scan rates (50, 100, 150, 200, 250, 300, 350, 400 mVs^{-1}) in 5 mM $[Fe(CN_6)]^{3-/4-}$, 0.1 M PB (pH 7.4) showing diffusion controlled process (b).*

Obtained electrochemical parameters are summarised in Table. 3.8.

Table. 3.7. *Obtained R_{ct} values on Au and Pt nanostructured same geometrical area electrode at numerous concentrations of PB buffer at 7.4 pH.*

PB/ mM	R_{ct}/ kΩ	
	Au	Pt
1.0	2717 ± 138	2360 ± 118
1.5	2017 ± 101	1741 ± 87
2.0	1500 ± 75	1299 ± 66
3.0	1088 ± 53	945 ± 48
5.0	726 ± 36	636 ± 31
10.0	485 ± 23	393 ± 19
20.0	347 ± 18	276 ± 13
50.0	244 ± 12	195 ± 10
100.0	212 ± 11	171 ± 9

The half wave potential ($E_0{}'$) after electrodeposition was 86 ± 4 mV and 92 ± 5 mV for Au and Pt, respectively. This value was much lower than the value observed for the unmodified SPCE (128 ± 2 mV). The peak to peak separation (△Ep) after electrodeposition was 155 ± 7 mV and 172 ± 3 mV for Au and Pt, respectively.

Table. 3.8. *Obtained $E_0{}'$, △Ep and k^o values on Au and Pt nanostructured electrodes after modification with anti-CA125, BSA and CA125.*

Configuration	$E_0{}'$/mV	△Ep/mV	k^o/x10^{-5}cms^{-1}
SPCE	128 ± 2	263 ± 4	52.8 ± 8.9
Au	86 ± 4	155 ± 7	185.0 ± 3.7
Pt	92 ± 5	172 ± 3	132.0 ± 4.6
Au/anti-CA125	96 ± 9	224 ± 15	81.0 ± 9.5
Pt/anti-CA125	68 ± 10	223 ± 12	65.7 ± 8.50
Au/anti-CA125/BSA	118 ± 4	320 ± 11	6.20 ± 0.87
Pt/anti-CA125/BSA	99 ± 5	498 ± 52	5.10 ± 0.19
Au/anti-CA125/BSA/CA125	101 ± 12	306 ± 53	6.70 ± 0.97
Pt/anti-CA125/BSA/CA125	110 ± 13	158 ± 49	2.50 ± 0.82

This value was significantly lower than the value observed for the unmodified SPCE (263 ± 4 mV), indicating faster electron transfer following the metal deposition. Anti-CA125 immobilisation decreased the peak current and increased △Ep. This behaviour could arise for several reasons. First, the presence of immobilised antibodies may decrease the rate of heterogeneous electron transfer to the solution-phase redox probe. Second, the electron transfer at regions modified with antibody may be effectively

blocked, causing the available area to decrease, in turn resulting in lower peak currents. These two possibilities affect the voltammetric response in different ways. The former mechanism was expected to change the apparent k^o, while the latter was expected only to decrease the peak current. In order to extract the heterogeneous electron transfer k^o, the full CVs (Fig. 3.28) were fitted using the formal potential. The working area of the electrode was set to the geometric area, 0.126 cm^2. The CVs fitted using the heterogeneous electron transfer rate constant as the only variable accurately reproduced the peak potentials across a range of potential scan rates.

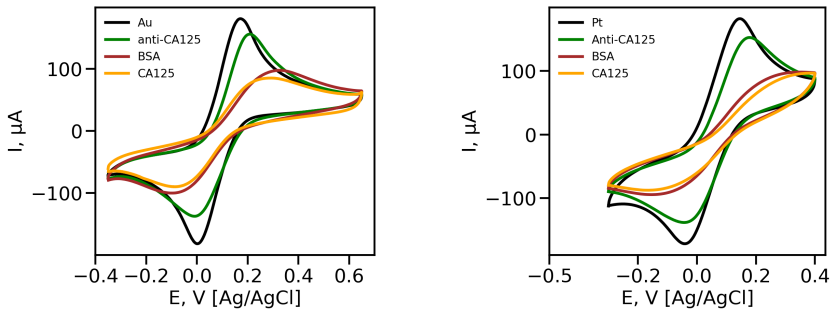

(a) ***(b)***

Fig. 3.28. *CVs of electrode Au (a) and Pt (b) nano-structured interfaces showing decrease of electron charge transfer caused by sensor fabrication steps including anti-CA125 loading, non-specific signal blocking with BSA, and detection of CA125, in 5 mM* $[Fe(CN_6)]^{3-/4-}$*, supported by 0.1 M PB (pH 7.4), at 100* mVs^{-1}.

For the Au nanostructures, k^o decreased after antibody immobilisation by a factor of two from 1.6 x 10^{-3} cms^{-1} to 8.1 x 10^{-4} cms^{-1}. At the Pt surface, the k^o decreased from 1.3 x 10^{-3} cms^{-1} to 6.5 x 10^{-4} cm s^{-1}. Immobilisation of the blocking agent, BSA, caused a further decrease in the current. Significantly, after BSA blocking at the Au nanostructured electrode, k^o decreased to 6.2 x 10^{-5} cms^{-1}.

These observations were consistent with the k^o decreased more than 13-fold to 5.1 x 10^{-5} cms^{-1} after BSA blocking. The change of k^o after BSA blocking was higher, since Au surface coverage by BSA was relatively higher than the surface coverage by antibody. Finally, when antigen CA125 was captured, the current of the peak in CVs decreased again. However, the k^o was indistinguishable before and after antigen binding at the antibody-modified Au nanostructures. In contrast, k^o decreased to 2.5 x 10^{-5} cms^{-1} after antigen binding at Pt nanostructured electrodes.

While the CV peak shapes were well-described by the theoretical fits, the magnitude of the experimental peak currents for the metal-coated electrodes was significantly lower than those predicted by the simulation. The fact that the experimental peak currents were lower than those predicted theoretically, even with the lower k^o values, could arise due to a lower effective electrode area (blockage of the electrode by the bound antibodies/blocking protein), impeded diffusion or electrostatic repulsion of the negatively charged probe by the polyanionic capture layer. However, the fact that an acceptable agreement between the theory and the experiment can be achieved without changing the diffusion coefficient suggests that the lower currents do not arise from the changes in the diffusional profile following antibody/protein adsorption.

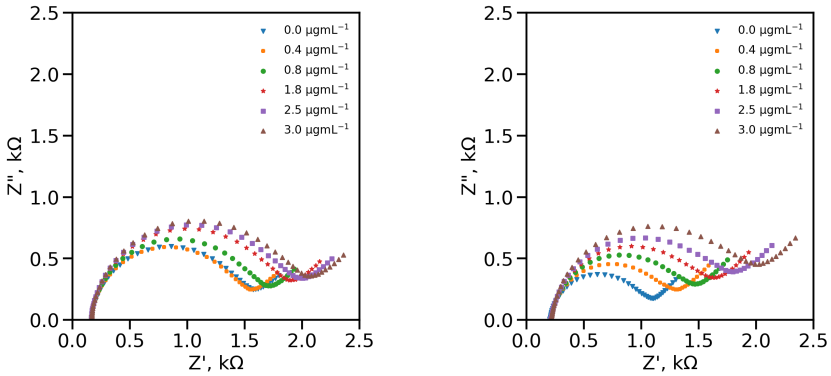

Fig. 3.29. *Nyquist plots of the signal after exposure to several concentrations of CA125 on Au nanostructured (a) and Pt nanostructured (b) interfaces, measured from 100,000 Hz to 0.1 Hz at 10 mV amplitude, DC voltage at OCP.*

An important factor that can influence the voltammetric response was the interfacial concentration of the probe that can deviate from the bulk value if there were electrostatic interactions between the adsorbed proteins and the probe. As the pI for the monoclonal anti-CA125 is 6.5 - 7.0; i.e., under the used voltammetric conditions, it is uncharged. However, BSA is negatively charged in the PBS buffer (pH 7.4). The CA125 antigen has an isoelectric point between 6.2 and 7.3, indicating that antigen is also negatively charged at pH 7.4. Thus, the entire antigen-capturing surface, consisting of the anti-CA125 and BSA, is likely to repel the $[Fe(CN_6)]^{3-/4-}$, decreasing its interfacial concentration electrostatically.

In Fig. 3.29 Nyquist plot semicircle sizes increase with increasing

amounts of CA125. Same concentration ranges of CA125 were used to compare response on Au (Fig. 3.29 (a)) and Pt (Fig. 3.29 (b)) nanostructured interfaces. The Nyquist plots presented in Fig. 3.29 were analysed using R_{ct} values and the standard Randles equivalent circuit model. As presented in Fig. 3.29, the charge transfer resistance increased with the increase in the target analyte concentration in the range from 0.4 µgmL^{-1} to 3 µgmL^{-1} on Au (a) and Pt (b) nanostructured interfaces.

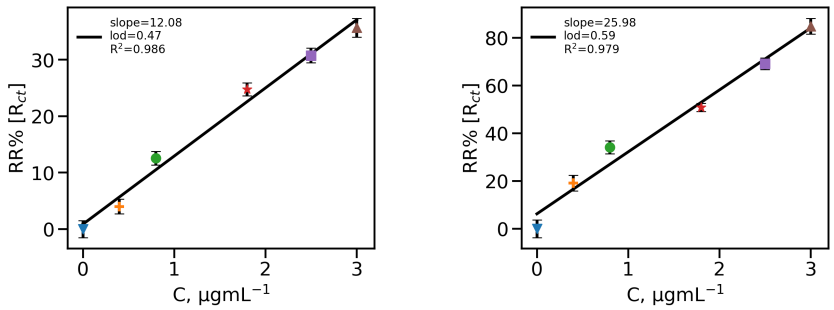

(a) ***(b)***

Fig. 3.30. *Calibration of CA125 from fitted Rct values obtained on Au nanostructured (a) and Pt nanostructured (b) interfaces, measured from 100,000 Hz to 0.1 Hz at 10 mV amplitude, DC voltage at OCP.*

The obtained slope values were of 12.08 RR%/ µgmL^{-1} and 25.98 RR%/ µgmL^{-1} for Au (Fig. 3.30 (a)) and Pt (Fig. 3.30 (b)) nanostructured interfaces, respectively. More than twice higher sensitivity of Pt nanostructures might be caused by a smaller size of Pt particles in comparison to Au nanostructures. Smaller nanoparticles might lead to higher antibody loading, which gives better sensor performance [36]. Also, higher sensitivity might be caused by higher electroactivity of the Pt itself. However, LOD value for Au nanostructured interface was slightly better (0.473 µgmL^{-1}) than that for Pt (0.589 µgmL^{-1}). Such a variation in LOD can be explained by the lower value of R^2 for Pt (R^2 = 0.979) than for Au (R^2 = 0.986).

As Z$''$ vs. frequency plot had well expressed wave shape (Fig. 3.31 (c), (d)), next step in the analysis was to plot maximum Z$''$ values vs. concentration of CA125 (Fig. 3.32). Using this method obtained sensitivity was 15.6 RR%/ µgmL^{-1} (Au) and 58.67 RR%/ µgmL^{-1} (Pt), with LOD values of 0.35 µgmL^{-1} and 0.68 µgmL^{-1} on Au and Pt interfaces, respectively.

Additionally, LOD values for Au or Pt nanostructured interfaces for CA125 were also analysed at several specific frequencies selected from Z$'$

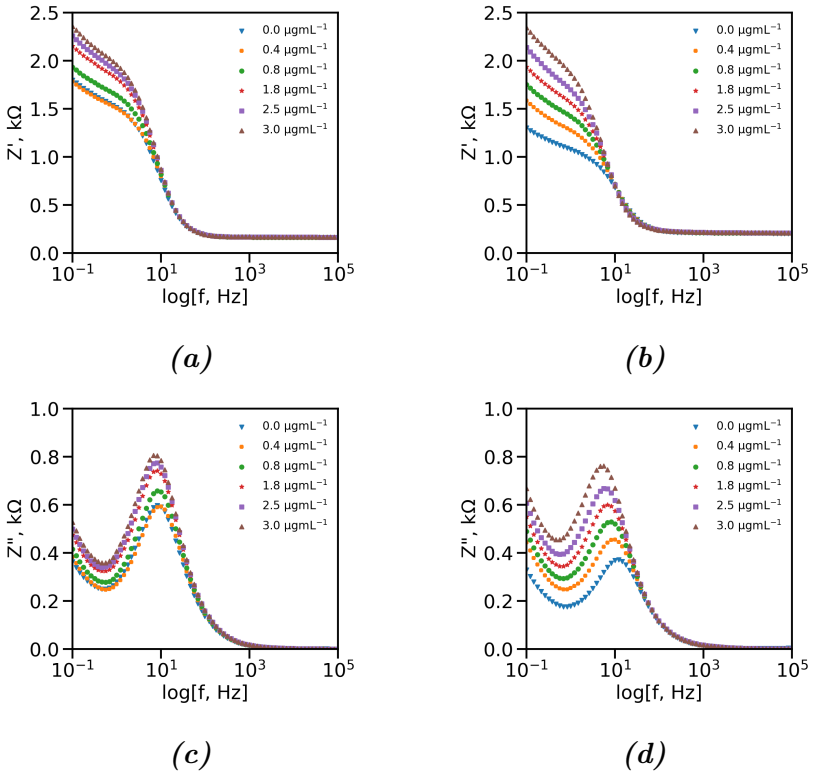

Fig. 3.31. *Z′ and Z″ plot vs. frequency of the signal after exposure to several concentrations of CA125 on Au ((a), (c)) and Pt ((b), (d)) nanostructured interfaces, measured from 100,000 Hz to 0.1 Hz at 10 mV amplitude, DC voltage at OCP.*

and Z″ vs. frequency plots (Fig. 3.31). Calibration curves are shown in Fig. 3.33 for Au (Z′ (a), Z″ (c)) and Pt (Z′ (b), Z″ (d)). In case of Au, values of slope, LOD and R^2 obtained at several frequencies (0.1, 2.61, 4.64, 6.81, 8.25, 38.31 Hz) are summarised in Table. 3.9. Resulting Z′ sensitivity ranged from 0.73 ± 0.52 RR%/ µgmL^{-1} (at 38.31 Hz) to 11.16 ± 0.79 RR%/ µgmL^{-1} (at 0.1 Hz) and LOD from 5.78 µgmL^{-1} (at 38.31 Hz) to 0.57 µgmL^{-1} (at 0.1 Hz). In case of Z″ (Au), sensitivity ranged from 6.85 ± 0.91 RR%/ µgmL^{-1} (at 38.31 Hz) to 15.2 ± 0.72 RR%/ µgmL^{-1} (at 0.1 Hz) and LOD from 1.08 µgmL^{-1} (at 38.31 Hz) to 0.38 µgmL^{-1} (at 0.1 Hz).

In case of Pt, values of slope, LOD and R^2 obtained at the same (0.1, 2.61, 4.64, 6.81, 8.25, 38.31 Hz) frequencies are summarised in Table. 3.10. Resulting Z′ sensitivity ranged from 2.07 ± 0.13 RR%/ µgmL^{-1} (at 38.31 Hz) to 23.69 ± 2.32 RR%/ µgmL^{-1} (at 0.1 Hz) and LOD from 3.60

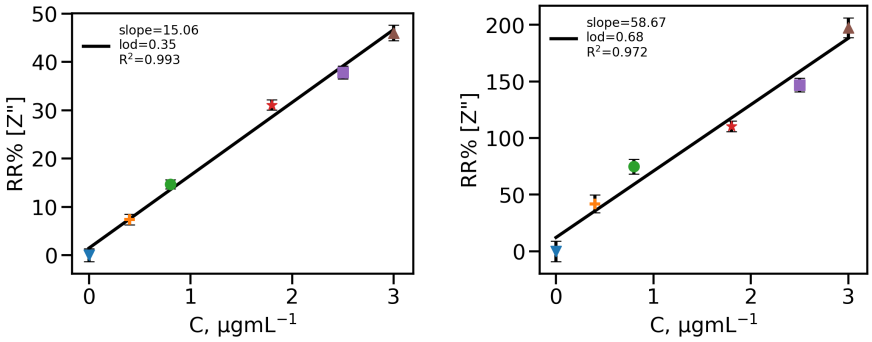

(a) *(b)*

Fig. 3.32. *Calibration of CA125 from maximum values of the peak of $Z^{''}$ vs frequency plot, obtained on Au nanostructured (a) and Pt nanostructured (b) interfaces, measured from 100,000 Hz to 0.1 Hz at 10 mV amplitude, DC voltage at OCP.*

Table. 3.9. *Parameters from $Z^{'}$ and $Z^{''}$ from EIS data for sensing of CA125 at several frequencies on Au nanostructured interface.*

f, Hz	Slope, RR%/μgmL^{-1}		LOD, μgmL^{-1}		R^2	
	$Z^{'}$	$Z^{''}$	$Z^{'}$	$Z^{''}$	$Z^{'}$	$Z^{''}$
0.1	11.16 ± 0.79	15.2 ± 0.72	0.57	0.38	0.98	0.991
2.61	9.40 ± 0.74	16.66 ± 1.72	0.64	0.86	0.976	0.957
4.64	7.83 ± 0.63	15.20 ± 1.59	0.65	0.84	0.975	0.958
6.81	6.26 ± 0.66	13.54 ± 1.32	0.81	0.79	0.962	0.963
8.25	5.37 ± 0.67	12.58 ± 1.17	1.01	0.75	0.941	0.967
38.31	0.73 ± 0.52	6.85 ± 0.91	5.78	1.08	0.328	0.934

μgmL^{-1} (at 8.25 Hz) to 0.50 μgmL^{-1} (at 38.31 Hz). In case of $Z^{''}$ (Pt), sensitivity ranged from 3.95 ± 0.91 RR%/ μgmL^{-1} (at 38.31 Hz) to 29.63 ± 3.76 RR%/μgmL^{-1} (at 0.1 Hz) and LOD from 1.87 μgmL^{-1} (at 38.31 Hz) to 0.67 μgmL^{-1} (at 2.61 Hz).

The spectra of values of Slope, R^2 and LOD in a range of frequencies (from 100,000 Hz to 0.1 Hz) for CA125 sensing on Au and Pt nanostructured interfaces are shown in Fig. 3.34 and Fig. 3.35 for $Z^{'}$ and $Z^{''}$ signal respectively.

In the case of values obtained from $Z^{'}$ measurements Fig. 3.34 R^2 and slope values were optimal for sensing in lower frequencies for both Au and Pt (Fig. 3.34 (a), (b)). In Au case, R^2, which shows the strength of the linear relationship between signal and frequency, was close to 1.0 in a

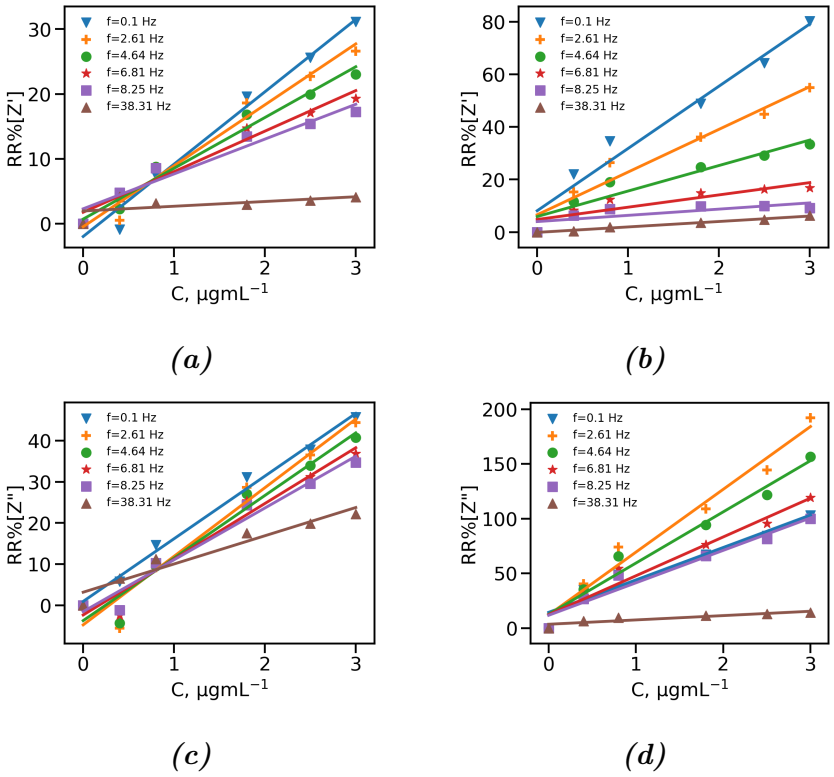

Fig. 3.33. *Calibration of CA125 obtained at several frequencies from Z' and Z'' plot vs. frequency on Au ((a), (c)) and Pt ((b), (d)) nanostructured interfaces, measured from 100,000 Hz to 0.1 Hz at 10 mV amplitude, DC voltage at OCP.*

range of frequencies from 0.1 to 5.623 Hz, while slope was at its highest in the similar range. LOD for Au was lowest in the same frequency range (Fig. 3.34 (c)). In comparison, Pt nano-structured interface R^2 and slope values were optimal in a narrower frequency range of 0.1 to 1.212 Hz, whereas a result LOD was lowest (Fig. 3.34 (b), (d)). Au LOD values in low frequencies were lower compared to that of Pt (Fig. 3.34 (c), (d)), which is explained by slightly lower R^2 for Pt (R^2 = 0.972) interface compared to Au interface (R^2 = 0.993). In case of values obtained from Z'' plots Fig. 3.35 R^2 follow a different pattern between Au and Pt. In the case of Au R^2 was optimal in a rather narrow low-frequency range of 0.1 - 0.215 Hz, although slope peaked at 1.468 Hz which was not part of this interval (Fig. 3.35 (a)).

Resulting LOD value on Au interface was at its lowest at 0.1 Hz (Fig. 3.35 (c)), demonstrating that R^2 value, in this case, has more con-

Table. 3.10. *Parameters from Z′ and Z″ from EIS data for sensing of CA125 at several frequencies on Pt nanostructured interface.*

f, Hz	Slope, RR%/μgmL^{-1}		LOD, μgmL^{-1}		R^2	
	Z′	Z″	Z′	Z″	Z′	Z″
0.1	23.69 ± 2.32	29.63 ± 3.76	0.79	1.02	0.963	0.940
2.61	16.24 ± 1.86	57.36 ± 4.77	0.92	0.67	0.95	0.973
4.64	9.70 ± 1.58	46.77 ± 4.15	1.32	0.72	0.904	0.969
6.81	4.68 ± 1.27	35.47 ± 3.64	2.19	0.83	0.772	0.959
8.25	2.37 ± 1.06	29.64 ± 3.35	3.60	0.91	0.558	0.951
38.31	2.07 ± 0.13	3.95 ± 0.91	0.50	1.87	0.985	0.824

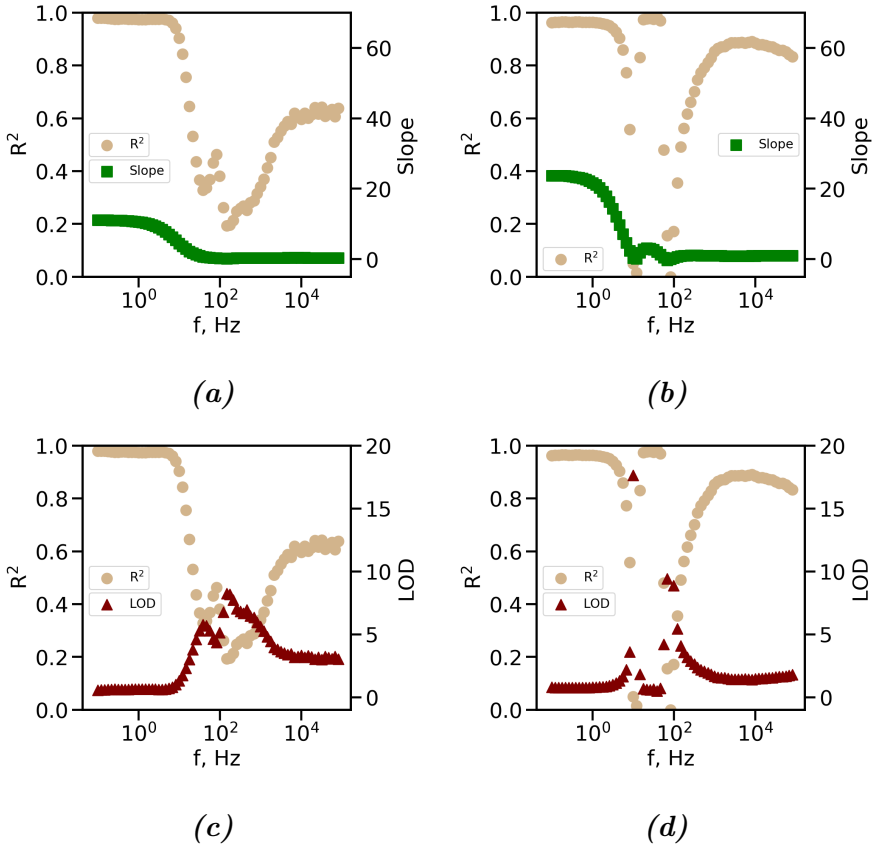

Fig. 3.34. *Slope and LOD calculated for CA125 at different frequencies from Bode Z′ plots on Au (a), (c) and Pt (b), (d) nanostructured interface.*

siderable significance for LOD than for slope. For comparison, in the case of Pt R^2 was optimal at frequency 2.61 Hz, and slope peaked dramatically at a similar frequency of 1.778 Hz (Fig. 3.35 (b)). Resulting LOD

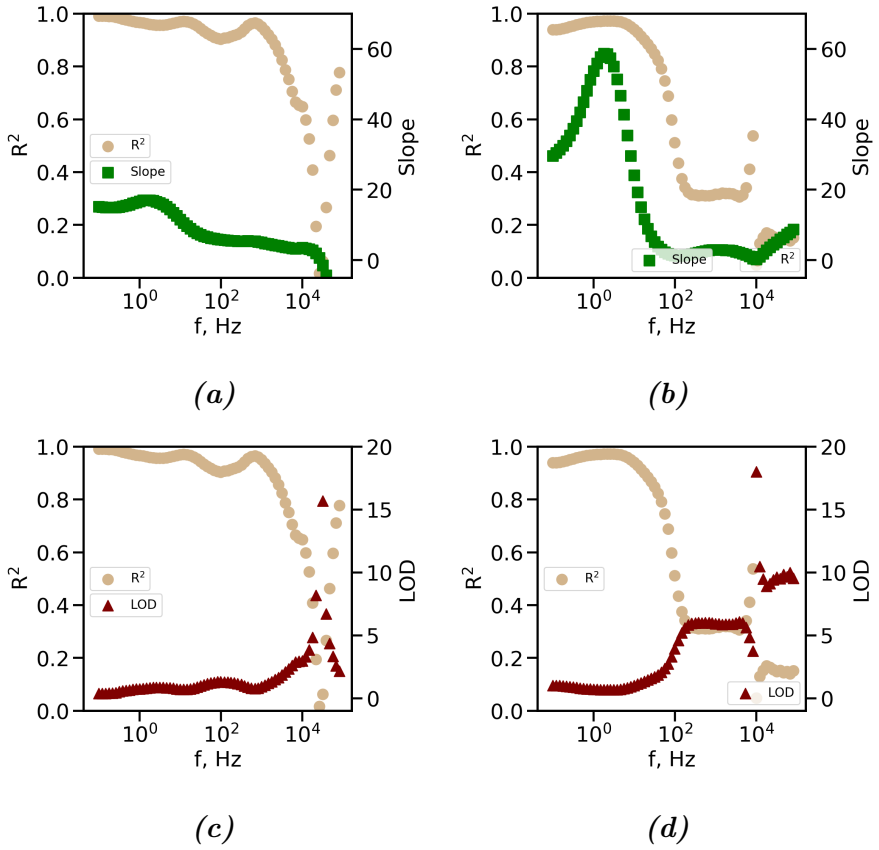

Fig. 3.35. *Slope and LOD calculated for CA125 at different frequencies from Bode Z'' plots on Au (a), (c) and Pt (b), (d) nanostructured interface.*

value on Pt interface was at its lowest at 2.61 Hz, which similarly to Au results shows the greater influence of R^2 on LOD (Fig. 3.35 (d)) rather than Slope. In summary, similarly to Z', Z'' vs frequency plots results had optimal LOD on Au interface at lower frequencies compared to Pt. In general, LOD on Au interface was lower compared to Pt, due to more fabulous linear fit (R^2).

Conclusions

1. For the first time, interdigitated gold microarray electrode was fabricated using soft lithography and wet etching. A special design of the electrode was created and optimised according to the results microscopic and electrochemical characterisation demonstrating electrochemical signal variation of only 5 %.

2. The interdigitated array electrodes were modified with Pt coating for H_2O_2 sensing with the determined sensitivity to H_2O_2 of $2662\,\mu Acm^{-2}mM^{-1}$ with an LOD value of 21.7 nM., using electroplating, where roughness of Pt can be reliably controlled by varying number of cycles performing cyclic voltammetry.

3. Completed analysis of fabricated interdigitated electrode geometry, using finite difference method, modelled CV response of the Fc/Fc+ redox couple including simulation of overlapping diffusion layers. The model has shown that current increases within 30 % at low scan rates (5 mVs^{-1}), when working and counter electrodes are in interdigitated array configuration.

4. Comparison of Au miniaturised electrode and conventional Ag/AgCl electrode revealed a -100 mV shift of CV signal for Au electrode caused by different potential of Au. No significant changes in CV anodic and catodic currents were observed when miniaturised (5 µL cell) Au reference was used, giving excellent CV signal variance characteristic of no greater than 1 %.

5. As a proof of miniaturised cell, electrochemically active species FcMeOH were detected using CV (in 5 µL volume) with a dynamic range from 0.5 µM to 1000 µM, with sensitivity of 0.718 and 0.283 $nA\mu M^{-1}$ and LOD of 32 µM and 74 µM obtained at 50 mVs^{-1}, and sensitivity of 0.851 and 0.498 $nA\mu M^{-1}$, LOD of 24 and 51 µM at 5 mVs^{-1} from anodic and cathodic currents.

6. Prior fabrication of electrochemical sensor to carcinoma antigen 125 on interdigitated array electrodes, antibody as bioreceptor was immobilised on flat substrate and antibody coverage was studied using imaging ellipsometry, showing the average height of bioreceptor (antibody) of 3.79 ± 0.54 nm, which was successfully tested for carcinoma antigen 125 detection using surface plasmon resonance.

7. Procedure of antibody immobilisation used on flat substrate was successfully adapted onto interdigitated array microelectrodes and carcinoma antigen 125 was detected in concentration range from

0.2 to 3 µgmL^{-1}. Data analysis using various parameters from electrochemical impedance spectroscopy data was performed utilising Nyquist, Z$'$ and Z$''$ vs frequency plots. The lowest LOD of 1.20 µgmL^{-1} was observed from Z$''$ vs frequency plot at 10 Hz using immittance single frequency analysis.

8. The Au and Pt modified electrodes, due to their higher area than plane electrodes, obtained better LOD than interdigitated array microelectrodes. The best obtained LOD values were 0.37 µgmL^{-1} and 0.58 µgmL^{-1} for Au and Pt nanostructured interfaces respectively.

Bibliography

[1] N. L. Abbottt, A. Kumar, and G. M. Whitesides. Using Micromachining, Molecular Self-Assembly, and Wet Etching to Fabricate 0.1-1-μm-Scale Structures of Gold and Silicon. *Chem. Mater.*, 6(5):596–602, 1994.

[2] B.-R. Adhikari, M. Govindhan, and A. Chen. Carbon Nanomaterials Based Electrochemical Sensors/Biosensors for the Sensitive Detection of Pharmaceutical and Biological Compounds. *Sensors*, 15(9):22490–22508, 2015.

[3] M. Aizawa, A. Morioka, H. Matsuoka, S. Suzuki, Y. Nagamura, R. Shinohara, and I. Ishiguro. An enzyme immunosensor for IgG. *J. Solid-Phase Biochem.*, 1(4):319–328, 1976.

[4] K. Akita, S. Yoshida, Y. Ikehara, S. Shirakawa, M. Toda, M. Inoue, J. Kitawaki, H. Nakanishi, H. Narimatsu, and H. Nakada. Different levels of sialyl-Tn antigen expressed on MUC16 in patients with endometriosis and ovarian cancer. *Int. J. Gynecol. Cancer*, 22(4):531–538, 2012.

[5] I. Al-Ogaidi, Z. P. Aguilar, S. Suri, H. Gou, and N. Wu. Dual detection of cancer biomarker CA125 using absorbance and electrochemical methods. *Analyst*, 138(19):5647, 2013.

[6] C. Amarasiri, T. B. Nguyen, L. T. Nguyen, V. T. Thu, N. T. M. Thuy, and T. Dai Lam. Electrochemical Immunosensor Based on Fe3O4/PANI/AuNP Detecting Interface for Carcinoembryonic Antigen Biomarker. *J. Electron. Mater.*, 46(10):5755–5763, 2017.

[7] L. Anicai, C. Stoica, C. Vladut, A. Negru, J. M. Teulon, M. Odorico, J. L. Pellequer, P. Parot, and M. Enachescu. Synthesis and characterization of a novel screen-printed modified gold electrode with applications in uranyl ions detection. *Rev. Chim.*, 66(10):1639–1644, 2015.

[8] S. Babacan, P. Pivarnik, S. Letcher, and A. Rand. Evaluation of antibody immobilization methods for piezoelectric biosensor application. *Biosens. Bioelectron.*, 15(11):615–621, 2000.

[9] K. Bagga, R. McCann, F. O'Sullivan, P. Ghosh, S. Krishnamurthy, A. Stalcup, M. Vázquez, and D. Brabazon. Nanoparticle functionalized laser patterned substrate: an innovative route towards low cost biomimetic platforms. *RSC Adv.*, 7(13):8060–8069, 2017.

[10] E. B. Bahadır and M. K. Sezgintürk. A review on impedimetric biosensors. *Artif. Cells, Nanomedicine, Biotechnol.*, 44(1):248–262, 2016.

[11] B. Balakrisnan, S. Patil, and E. Smela. Patterning PDMS using a combination of wet and dry etching. *J. Micromechanics Microengineering*, 19(4):047002, 2009.

[12] A. D. Bani-Yaseen. Fabrication of electrochemically deposited microelectrodes for microfluidic MEMS applications. *Int. J. Electrochem. Sci.*, 5(12):1837–1846, 2010.

[13] A. J. Bard and L. R. Faulkner. *Electrochemical Methods: Fundamentals and Applications*. John Wiley & Sons, Berlin, Heidelberg, 2 nd edition, 1994.

[14] E. Barsoukov and J. R. Macdonald. *Impedance spectroscopy*. John Wiley & Sons, 2nd edition, 2005.

[15] F. C. Bedatty Fernandes, A. V. Patil, P. R. Bueno, and J. J. Davis. Optimized Diagnostic Assays Based on Redox Tagged Bioreceptive Interfaces. *Anal. Chem.*, 87(24):12137–12144, 2015.

[16] D. J. Beebe, G. A. Mensing, and G. M. Walker. Physics and Applications of Microfluidics in Biology. *Annu. Rev. Biomed. Eng.*, 4(1):261–286, 2002.

[17] J. Benesch, S. Svedhem, S. C. Svensson, R. Valiokas, B. Liedberg, and P. Tengvall. Protein adsorption to oligo(ethylene glycol) self-assembled monolayers: Experiments with fibrinogen, heparinized plasma, and serum. *J. Biomater. Sci.*, 12(6):581–597, 2001.

[18] C. Berggren and G. Johansson. Capacitance Measurements of Antibody-Antigen Interactions in a Flow System. *Anal. Chem.*, 69(18):3651–3657, 1997.

[19] K. B. Blodgett. Monomolecular films of fatty acids on glass. *J. Am. Chem. Soc.*, 56(2):495, 1934.

[20] S. Brankovic, J. Wang, and R. Adžić. Metal monolayer deposition by replacement of metal adlayers on electrode surfaces. *Surf. Sci.*, 474(1-3):173–179, 2001.

[21] D. Brealey, S. Karyampudi, T. S. Jacques, M. Novelli, R. Stidwill, V. Taylor, R. T. Smolenski, and M. Singer. Mitochondrial dysfunction in a long-term rodent model of sepsis and organ failure. *Am. J. Physiol. - Regul. Integr. Comp. Physiol.*, 286(3 55-3):1–17, 2004.

[22] P. R. Bueno and J. J. Davis. Elucidating redox-level dispersion and local dielectric effects within electroactive molecular films. *Anal. Chem.*, 86(4):1997–2004, 2014.

[23] P. R. Bueno, G. T. Feliciano, and J. J. Davis. Capacitance spectroscopy and density functional theory. *Phys. Chem. Chem. Phys.*, 17(14):9375–9382, 2015.

[24] R. Burger, L. Amato, and A. Boisen. Detection methods for centrifugal microfluidic platforms. *Biosens. Bioelectron.*, 76:54–67, 2016.

[25] K. Chaisiwamongkhol, K. Ngamchuea, C. Batchelor-McAuley, and R. G. Compton. Multiwalled Carbon Nanotube Modified Electrodes for the Adsorptive Stripping Voltammetric Determination and Quantification of Curcumin in Turmeric. *Electroanalysis*, 29(4):1049–1055, 2017.

[26] D. Chen, Q. Tao, L. W. Liao, S. X. Liu, Y. X. Chen, and S. Ye. Determining the Active Surface Area for Various Platinum Electrodes. *Electrocatalysis*, 2(3):207–219, 2011.

[27] X. Chen, Q. Zhang, C. Qian, N. Hao, L. Xu, and C. Yao. Electrochemical aptasensor for mucin 1 based on dual signal amplification of poly(o-phenylenediamine) carrier and functionalized carbon nanotubes tracing tag. *Biosens. Bioelectron.*, 64:485–492, 2015.

[28] B. V. Chikkaveeraiah, A. A. Bhirde, N. Y. Morgan, H. S. Eden, and X. Chen. Electrochemical immunosensors for detection of cancer protein biomarkers. *ACS Nano*, 6(8):6546–6561, 2012.

[29] S. D. Collyer, F. Davis, and S. P. Higson. Sonochemically fabricated microelectrode arrays for use as sensing platforms. *Sensors*, 10(5):5090–5132, 2010.

[30] R. G. Compton and C. E. Banks. *Understanding Voltammetry*. Imperial College Press, 2nd edition, 2007.

[31] R. G. Compton, E. Laborda, and K. R. Ward. *Understanding voltammetry: Simulation of electrode processes*. Imperial College Press, London, UK, 2013.

[32] P. Damborský, J. Švitel, and J. Katrlík. Optical biosensors. *Essays Biochem.*, 60(1):91–100, 2016.

[33] J. I. De Corcuera, R. P. Cavalieri, and J. R. Powers. Improved platinization conditions produce a 60-fold increase in sensitivity of amperometric biosensors using glucose oxidase immobilized in poly-o-phenylenediamine. *J. Electroanal. Chem.*, 575(2):229–241, 2005.

[34] H. Deng, W. Shen, Y. Peng, X. Chen, G. Yi, and Z. Gao. Nanoparticulate Peroxidase/Catalase Mimetic and Its Application. *Chem. - A Eur. J.*, 18(29):8906–8911, 2012.

[35] E. Desimoni, B. Brunetti, and R. Cattaneo. Comparing some operational approaches to the limit of detection. *Ann. Chim.*, 94(7-8):555–569, 2004.

[36] A. Detappe, M. Reidy, Y. Yu, C. Mathieu, H. V. Nguyen, T. P. Coroller, F. Lam, P. Jarolim, P. Harvey, A. Protti, Q. D. Nguyen, J. A. Johnson, Y. Cremillieux, O. Tillement, I. M. Ghobrial, and P. P. Ghoroghchian. Antibody-targeting of ultra-small nanoparticles enhances imaging sensitivity and enables longitudinal tracking of multiple myeloma. *Nanoscale*, 11(43):20485–20496, 2019.

[37] J.-P. Diard, B. Gorrec, and C. Le Montella. *Handbook of Electrochemical Impedance Spectroscopy. Electrical circuits containing CPEs.* 2013.

[38] J. M. Doña Rodríguez, J. A. H. Melián, and J. P. Peña. Determination of the Real Surface Area of Pt Electrodes by Hydrogen Adsorption Using Cyclic Voltammetry. *J. Chem. Educ.*, 77(9):1195–1197, 2000.

[39] S. Domínguez-Domínguez, J. Arias-Pardilla, Á. Berenguer-Murcia, E. Morallón, and D. Cazorla-Amorós. Electrochemical deposition of platinum nanoparticles on different carbon supports and conducting polymers. *J. Appl. Electrochem.*, 38(2):259–268, 2008.

[40] J. Dong, H. Zhao, M. Xu, Q. Maa, and S. Ai. A label-free electrochemical impedance immunosensor based on AuNPs/PAMAM-MWCNT-Chi nanocomposite modified glassy carbon electrode for detection of Salmonella typhimurium in milk. *Food Chem.*, 141(3):1980–1986, 2013.

[41] R. Drevinskas, T. Rakickas, A. Selskis, L. Rosa, and R. Valiokas. Cup-Shaped Nanoantenna Arrays for Zeptoliter Volume Biochemistry and Plasmonic Sensing in the Visible Wavelength Range. *ACS Appl. Mater. Interfaces*, 9(22):19082–19091, 2017.

[42] Y. Duan, X. Luo, Y. Qin, H. Zhang, G. Sun, X. Sun, and Y. Yan. Determination of epigallocatechin-3-gallate with a high-efficiency electrochemical sensor based on a molecularly imprinted poly(o-phenylenediamine) film. *J. Appl. Polym. Sci.*, 129(5):2882–2890, 2013.

[43] C. Dudok de Wit. Medische informatie voor verpleegkundigen. Autologe bloedtransfusie. *Tijdschr. Voor Ziekenverpl.*, 41(20):655–657, 1987.

[44] B. Eggins. Chemical Sensors and Biosensors. *Chem. Sensors Biosens.*, pages 1–273, 2007.

[45] A. A. Ensafi, H. A. Alinajafi, M. Jafari-Asl, B. Rezaei, and F. Ghazaei. Cobalt ferrite nanoparticles decorated on exfoliated graphene oxide, application for amperometric determination of NADH and H 2 O 2. *Mater. Sci. Eng. C*, 60:276–284, 2016.

[46] P. Estrela, D. Paul, Q. Song, L. K. Stadler, L. Wang, E. Huq, J. J. Davis, P. K. Ferrigno, and P. Migliorato. Label-free subpicomolar protein detection with field-effect transistors. *Anal. Chem.*, 82(9):3531–3536, 2010.

[47] S. A. Evans, J. M. Elliott, L. M. Andrews, P. N. Bartlett, P. J. Doyle, and G. Denuault. Detection of hydrogen peroxide at mesoporous platinum microelectrodes. *Anal. Chem.*, 74(6):1322–1326, 2002.

[48] A. M. Feltham and M. Spiro. Platinized platinum electrodes. *Chem. Rev.*, 71(2):177–193, 1971.

[49] F. C. Fernandes, J. R. Andrade, and P. R. Bueno. A nanoscale redox-active composite as a low-fouling interface for capacitive assaying. *Sensors Actuators, B Chem.*, 291:493–501, 2019.

[50] J. P. Folkers, C. B. Gorman, P. E. Laibinis, S. Buchholz, G. M. Whitesides, and R. G. Nuzzo. Self-Assembled Monolayers of Long-Chain Hydroxamic Acids on the Native Oxides of Metals. *Langmuir*, 11(3):813–824, 1995.

[51] X. Fu, J. Wang, N. Li, L. Wang, and L. Pu. Label-free electrochemical immunoassay of carcinoembryonic antigen in human serum using magnetic nanorods as sensing probes. *Microchim. Acta*, 165(3-4):437–442, 2009.

[52] P. Gajendran and R. Saraswathi. Electrocatalytic performance of poly(o-phenylenediamine)-Pt-Ru nanocomposite for methanol oxidation. *J. Solid State Electrochem.*, 17(10):2741–2747, 2013.

[53] I. García-Pineda, M. Mayén, J. M. Rodríguez-Mellado, and R. Rodríguez-Amaro. NADH electrocatalytic oxidation on gold nanoparticle-modified PVC/TTF-TCNQ composite electrode. Application as amperometric sensor. *Electroanalysis*, 25(8):1981–1987, 2013.

[54] V. Gau, S. C. Ma, H. Wang, J. Tsukuda, J. Kibler, and D. A. Haake. Electrochemical molecular analysis without nucleic acid amplification. *Methods*, 37(1):73–83, 2005.

[55] M. Gavutis, V. Navikas, T. Rakickas, Š. Vaitekonis, and R. Valiokas. Lipid dip-pen nanolithography on self-assembled monolayers. *J. Micromechanics Microengineering*, 26(2):025016, 2016.

[56] M. Geissler, H. Schmid, A. Bietsch, B. Michel, and E. Delamarche. Defect-tolerant and directional wet-etch systems for using monolayers as resists. *Langmuir*, 18(6):2374–2377, 2002.

[57] S. Goncalves, A. Peixoto, J. Rodrigues, A. Silva, and J. Correia. Microshaping of Aluminum-based Neural Microelectrode Arrays Using Chemical Wet-etching. *Procedia Eng.*, 87:939–942, 2014.

[58] M. I. González-Sánchez, J. Agrisuelas, E. Valero, and R. G. Compton. Measurement of Total Antioxidant Capacity by Electrogenerated Iodine at Disposable Screen Printed Electrodes. *Electroanalysis*, 29(5):1316–1323, 2017.

[59] H. L. Gou, J. J. Xu, X. H. Xia, and H. Y. Chen. Air plasma assisting microcontact deprinting and printing for gold thin film and PDMS patterns. *ACS Appl. Mater. Interfaces*, 2(5):1324–1330, 2010.

[60] M. Govindhan, M. Amiri, and A. Chen. Au nanoparticle/graphene nanocomposite as a platform for the sensitive detection of NADH in human urine. *Biosens. Bioelectron.*, 66:474–480, 2015.

[61] L. Grosjean, B. Cherif, E. Mercey, A. Roget, Y. Levy, P. N. Marche, M. B. Villiers, and T. Livache. A polypyrrole protein microarray for antibody-antigen interaction studies using a label-free detection process. *Anal. Biochem.*, 347(2):193–200, 2005.

[62] M. Grossi and B. Riccò. Electrical impedance spectroscopy (EIS) for biological analysis and food characterization: A review. *J. Sensors Sens. Syst.*, 6(2):303–325, 2017.

[63] B. Grysakowski, J. J. Jasielec, B. Wierzba, T. Sokalski, A. Lewenstam, and M. Danielewski. Electrochemical Impedance Spectroscopy (EIS) of ion sensors: Direct modeling and inverse problem solving using the Nernst-Planck-Poisson (NPP) model and the HGS(FP) optimization strategy. *J. Electroanal. Chem.*, 662(1):143–149, 2011.

[64] S. B. Hall, E. A. Khudaish, and A. L. Hart. Electrochemical oxidation of hydrogen peroxide at platinum electrodes. Part II: Effect of potential. *Electrochim. Acta*, 43(14-15):2015–2024, 1998.

[65] O. Hosu, M. Tertiș, G. Melinte, B. Feier, R. Săndulescu, and C. Cristea. Mucin 4 detection with a label-free electrochemical immunosensor. *Electrochem. commun.*, 80:39–43, jul 2017.

[66] C. J. Huang, W. Knoll, A. Sessitsch, and J. Dostalek. SPR bacterial pathogen biosensor: The importance of fluidic conditions and probing depth. *Talanta*, 122:166–171, 2014.

[67] J. Huang, Z. Li, B. Y. Liaw, and J. Zhang. Graphical analysis of electrochemical impedance spectroscopy data in Bode and Nyquist representations. *J. Power Sources*, 309:82–98, 2016.

[68] M. M. Jankovic and B. S. Tapuskovic. Molecular forms and microheterogeneity of the oligosaccharide chains of pregnancy-associated CA125 antigen. *Hum. Reprod.*, 20(9):2632–2638, 2005.

[69] A. Jiménez, M. P. G. Armada, J. Losada, C. Villena, B. Alonso, and C. M. Casado. Amperometric biosensors for NADH based on hyperbranched dendritic ferrocene polymers and Pt nanoparticles. *Sensors Actuators, B Chem.*, 190:111–119, 2014.

[70] A. Johnson, Q. Song, P. Ko Ferrigno, P. R. Bueno, and J. J. Davis. Sensitive affimer and antibody based impedimetric label-free assays for C-reactive protein. *Anal. Chem.*, 84(15):6553–6560, 2012.

[71] H. J. Kang, E. J. Cha, and H. D. Park. Protein immobilization onto various surfaces using a polymer-bound isocyanate. *Appl. Surf. Sci.*, 324:198–204, 2015.

[72] A. Kaushik, A. Yndart, S. Kumar, R. D. Jayant, A. Vashist, A. N. Brown, C. Z. Li, and M. Nair. A sensitive electrochemical immunosensor for label-free detection of Zika-virus protein. *Sci. Rep.*, 8(1):3–7, 2018.

[73] D. Kim and A. E. Herr. Protein immobilization techniques for microfluidic assays. *Biomicrofluidics*, 7(4):1–47, 2013.

[74] J. Kitawaki, H. Ishihara, H. Koshiba, M. Kiyomizu, M. Teramoto, Y. Kitaoka, and H. Honjo. Usefulness and limits of CA-125 in diagnosis of endometriosis without associated ovarian endometriomas. *Hum. Reprod.*, 20(7):1999–2003, 2005.

[75] Y. Kong, J. Li, S. Wu, W. Cheng, R. K. Rana, and J. J. Zhu. Functionalization of poly(o-phenylenediamine) with gold nanoparticles as a label-free immunoassay platform for the detection of human enterovirus 71. *Sensors Actuators, B Chem.*, 183:187–193, 2013.

[76] G. Koukouvinos, P. Petrou, K. Misiakos, D. Drygiannakis, I. Raptis, G. Stefanitsis, S. Martini, D. Nikita, D. Goustouridis, I. Moser, G. Jobst, and S. Kakabakos. Simultaneous determination of CRP and D-dimer in human blood plasma samples with White Light Reflectance Spectroscopy. *Biosens. Bioelectron.*, 84:89–96, 2016.

[77] V. Kulasingam, M. P. Pavlou, and E. P. Diamandis. Integrating high-throughput technologies in the quest for effective biomarkers for ovarian cancer. *Nat. Rev. Cancer*, 10(5):371–378, 2010.

[78] D. Kyprianou, A. R. Guerreiro, I. Chianella, E. V. Piletska, S. A. Fowler, K. Karim, M. J. Whitcombe, A. P. Turner, and S. A. Piletsky. New reactive polymer for protein immobilisation on sensor surfaces. *Biosens. Bioelectron.*, 24(5):1365–1371, 2009.

[79] P. E. Laibinis, G. M. Whitesides, D. L. Aliara, Y. T. Tao, A. N. Parikh, and R. G. Nuzzo. Comparison of the Structures and Wetting Properties of Self-Assembled Monolayers of n-Alkanethiols on the Coinage Metal Surfaces, Cu, Ag, Au. *J. Am. Chem. Soc.*, 113(19):7152–7167, 1991.

[80] Y. Li, C. Sella, F. Lemaître, M. GuilleCollignon, L. Thouin, and C. Amatore. Highly Sensitive Platinum-Black Coated Platinum Electrodes for Electrochemical Detection of Hydrogen Peroxide and Nitrite in Microchannel. *Electroanalysis*, 25(4):895–902, 2013.

[81] J. C. Liao, M. Mastali, V. Gau, M. A. Suchard, A. K. Møller, D. A. Bruckner, J. T. Babbitt, Y. Li, J. Gornbein, E. M. Landaw, E. R. McCabe, B. M. Churchill, and D. A. Haake. Use of electrochemical DNA biosensors for rapid molecular identification of uropathogens in clinical urine specimens. *J. Clin. Microbiol.*, 44(2):561–570, 2006.

[82] D. Lin, K. D. Harris, N. W. Chan, and A. B. Jemere. Nanostructured indium tin oxide electrodes immobilized with toll-like receptor proteins for label-free electrochemical detection of pathogen markers. *Sensors Actuators, B Chem.*, 257:324–330, 2018.

[83] X. Lin, Q. Wang, S. Zhu, J. Xu, Q. Xia, and Y. Fu. A highly sensitive glutamic acid biosensor based on the determination of NADH enzymically generated by l-glutamic dehydrogenase. *RSC Adv.*, 6(51):45829–45834, 2016.

[84] C. H. Liu, K. T. Liao, and H. J. Huang. Amperometric immunosensors based on protein A coupled polyaniline- perfluorosulfonated ionomer composite electrodes. *Anal. Chem.*, 72(13):2925–2929, 2000.

[85] F. Liu, G. Kolesov, and B. A. Parkinson. Time of Flight Electrochemistry: Diffusion Coefficient Measurements Using Interdigitated Array (IDA) Electrodes. *J. Electrochem. Soc.*, 161(13):H3015–H3019, 2014.

[86] L. Liu, Y. Li, L. Tian, T. Guo, W. Cao, and Q. Wei. A label-free voltammetric immunoassay based on 3D-structured rGO-MWCNT-Pd for detection of human immunoglobulin G. *Sensors Actuators, B Chem.*, 211:170–176, 2015.

[87] Y. Liu, X. Liu, S. Chen, Q. Liu, and W. Peng. Investigation of a Capillary-Based Surface Plasmon Resonance Sensor for Biosensing. *J. Light. Technol.*, 34(17):4030–4042, 2016.

[88] M. P. Longinotti and H. R. Corti. Diffusion of ferrocene methanol in super-cooled aqueous solutions using cylindrical microelectrodes. *Electrochem. commun.*, 9(7):1444–1450, 2007.

[89] J. C. Love, L. A. Estroff, J. K. Kriebel, R. G. Nuzzo, and G. M. Whitesides. Self-assembled monolayers of thiolates on metals as a form of nanotechnology. *Chem. Rev.*, 105(4):1103–1169, 2005.

[90] B. Lu, M. R. Smyth, and R. O'Kennedy. Oriented immobilization of antibodies and its applications in immunoassays and immunosensors, 1996.

[91] X. Luo and J. J. Davis. Electrical biosensors and the label free detection of protein disease biomarkers. *Chem. Soc. Rev.*, 42(13):5944–5962, 2013.

[92] X. Luo, M. Xu, C. Freeman, T. James, and J. J. Davis. Ultrasensitive label free electrical detection of insulin in neat blood serum. *Anal. Chem.*, 85(8):4129–4134, 2013.

[93] N. S. Lynn, H. Šípová, P. Adam, and J. Homola. Enhancement of affinity-based biosensors: Effect of sensing chamber geometry on sensitivity. *Lab Chip*, 13(7):1413–1421, 2013.

[94] M. Lyons. Mediated Electron Transfer at Redox Active Monolayers Part 2 : Analysis of the Chronoamperometric Response to a Potential Step Perturbation. *Sensors*, 2(8):314–330, 2002.

[95] J. Ma, S. Luan, L. Song, S. Yuan, S. Yan, J. Jin, and J. Yin. Facile fabrication of microsphere-polymer brush hierarchically three-dimensional (3D) substrates for immunoassays. *Chem. Commun.*, 51(31):6749–6752, 2015.

[96] L. Malysheva, A. Onipko, R. Valiokas, and B. Liedberg. First-principles modeling of oligo(ethylene glycol)-terminated and amide group containing alkanethiolates. *Appl. Surf. Sci.*, 246(4):372–376, 2005.

[97] G. Mattana and D. Briand. Recent advances in printed sensors on foil. *Mater. Today*, 19(2):88–99, 2016.

[98] D. Menshykau, X. J. Huang, N. V. Rees, F. J. Del Campo, F. X. Muñoz, and R. G. Compton. Investigating the concept of diffusional independence. Potential step transients at nano- and microelectrode arrays: Theory and experiment. *Analyst*, 134(2):343–348, 2009.

[99] M. H. Meyer, M. Hartmann, and M. Keusgen. SPR-based immunosensor for the CRP detection - A new method to detect a well known protein. *Biosens. Bioelectron.*, 21(10):1987–1990, 2006.

[100] T. Michurina, M. Kerzhner, and B. Klimovich. Development and characterization of three novel monoclonal antibodies against CA-125. *Monoclon. Antib. Immunodiagn. Immunother.*, 33(5):319–324, 2014.

[101] N. Nakatsuka, K. A. Yang, J. M. Abendroth, K. M. Cheung, X. Xu, H. Yang, C. Zhao, B. Zhu, Y. S. Rim, Y. Yang, P. S. Weiss, M. N. Stojanović, and A. M. Andrews. Aptamer-field-effect transistors overcome Debye length limitations for small-molecule sensing. *Science (80-.).*, 362(6412):319–324, 2018.

[102] K. Ngamchuea, S. Eloul, K. Tschulik, and R. G. Compton. Planar diffusion to macro disc electrodes—what electrode size is required for the Cottrell and Randles-Sevcik equations to apply quantitatively? *J. Solid State Electrochem.*, 18(12):3251–3257, 2014.

[103] K. Nustad, R. C. Bast, T. J. O'brien, O. Nilsson, P. Seguin, M. R. Suresh, T. Saga, S. Nozawa, O. P. Børmer, H. W. de Bruijn, M. Nap, A. Vitali, M. Gadnell, J. Clark, K. Shigemasa, B. Karlsson, F. T. Kreutz, D. Jette, H. Sakahara, K. Endo, E. Paus, D. Warren, S. Hammarström, P. Kenemans, and J. Hilgers. Specificity and affinity of 26 monoclonal antibodies against the CA 125 antigen: First report from the ISOBM TD-1 workshop. *Tumor Biol.*, 17(4):196–219, 1996.

[104] T. J. O'Brien, J. B. Beard, L. J. Underwood, R. A. Dennis, A. D. Santin, and L. York. The CA 125 gene: An extracellular superstructure dominated by repeat sequences. *Tumor Biol.*, 22(6):348–366, 2001.

[105] R. Ojani, P. Hamidi, and J. B. Raoof. Sensitive amperometric pyridoxine sensor based on self-assembled Prussian blue nanoparticle-modified poly(o-phenylenediamine)/glassy carbon electrode. *Appl. Organomet. Chem.*, 30(5):297–303, 2016.

[106] E. Ouellet, C. Lausted, T. Lin, C. W. T. Yang, L. Hood, and E. T. Lagally. Parallel microfluidic surface plasmon resonance imaging arrays. *Lab Chip*, 10(5):581–588, 2010.

[107] A. V. Patil, F. C. Bedatty Fernandes, P. R. Bueno, and J. J. Davis. Immittance electroanalysis in diagnostics. *Anal. Chem.*, 87(2):944–950, jan 2015.

[108] A. V. Patil, F. B. Fernandes, P. R. Bueno, and J. J. Davis. Graphene-based protein biomarker detection. *Bioanalysis*, 7(6):725–742, 2015.

[109] R. Pauliukaite, A. M. Chiorcea Paquim, A. M. Oliveira Brett, and C. M. Brett. Electrochemical, EIS and AFM characterisation of biosensors: Trioxysilane sol-gel encapsulated glucose oxidase with two different redox mediators. *Electrochim. Acta*, 52(1):1–8, 2006.

[110] R. Pauliukaite, M. E. Ghica, O. Fatibello-Filho, and C. M. Brett. Electrochemical impedance studies of chitosan-modified electrodes for application in electrochemical sensors and biosensors. *Electrochim. Acta*, 55(21):6239–6247, 2010.

[111] A. POCKELS. On the relative contamination of the water-surface by equal quantities of different substances. *Nature*, 46(1192):418–419, sep 1892.

[112] B. Prieto-Simón and E. Fàbregas. New redox mediator-modified polysulfone composite films for the development of dehydrogenase-based biosensors. *Biosens. Bioelectron.*, 22(1):131–137, 2006.

[113] L. Qiang, S. Vaddiraju, J. F. Rusling, and F. Papadimitrakopoulos. Highly sensitive and reusable Pt-black microfluidic electrodes for long-term electrochemical sensing. *Biosens. Bioelectron.*, 26(2):682–688, 2010.

[114] D. Qin, Y. Xia, and G. M. Whitesides. Soft lithography for micro- and nanoscale patterning. *Nat. Protoc.*, 5(3):491–502, 2010.

[115] Y. Qu, L. Chen, H. Deng, and C. Li. Sandwich-type electrochemical immunosensor for sensitive determination of IgG based on the enhanced effects of poly-L-lysine functionalized reduced graphene

oxide nanosheets and gold nanoparticles. *J. Solid State Electrochem.*, 21(11):3281–3287, 2017.

[116] D. G. Rackus, M. H. Shamsi, and A. R. Wheeler. Electrochemistry, biosensors and microfluidics: a convergence of fields. *Chem. Soc. Rev.*, 44(15):5320–5340, 2015.

[117] G. Rahman, S. A. Mian, A. u. H. A. Shah, and O. S. Joo. Electrocatalytic behavior of glassy carbon electrode modified with ruthenium nanoparticles and ruthenium film. *J. Appl. Electrochem.*, 46(4):459–468, 2016.

[118] T. Rakickas, M. Gavutis, A. Reichel, J. Piehler, B. Liedberg, and R. Valiokas. Protein-Protein Interactions in Reversibly Assembled Nanopatterns. *Nano Lett.*, 8(10):3369–3375, 2008.

[119] C. R. Rao and D. C. Trivedi. Chemical and electrochemical depositions of platinum group metals and their applications. *Coord. Chem. Rev.*, 249(5-6):613–631, 2005.

[120] S. V. Rao, K. W. Anderson, and L. G. Bachas. Oriented Immobilization of Proteins. *Mikrochim. Acta*, 128(3–4):127–143, 1998.

[121] M. A. Raso, I. Carrillo, E. Navarro, M. A. Garcia, E. Mora, and T. J. Leo. Fuel cell electrodes prepared by e-beam evaporation of Pt compared with commercial cathodes: Electrochemical and DMFC behaviour. *Int. J. Hydrogen Energy*, 40(34):11315–11321, 2015.

[122] A. Ravalli, G. Pilon Dos Santos, M. Ferroni, G. Faglia, H. Yamanaka, and G. Marrazza. New label free CA125 detection based on gold nanostructured screen-printed electrode. *Sensors Actuators B Chem.*, 179:194–200, mar 2013.

[123] L. Reverté, B. Prieto-Simón, and M. Campàs. New advances in electrochemical biosensors for the detection of toxins: Nanomaterials, magnetic beads and microfluidics systems. A review. *Anal. Chim. Acta*, 908:8–21, 2016.

[124] B. Rezaei, M. K. Boroujeni, and A. A. Ensafi. Development of Sudan II sensor based on modified treated pencil graphite electrode with DNA, o-phenylenediamine, and gold nanoparticle bioimprinted polymer. *Sensors Actuators, B Chem.*, 222:849–856, 2016.

[125] M. R. Russell, C. Graham, A. D'Amato, A. Gentry-Maharaj, A. Ryan, J. K. Kalsi, C. Ainley, A. D. Whetton, U. Menon, I. Jacobs, and R. L. Graham. A combined biomarker panel shows improved sensitivity for the early detection of ovarian cancer allowing

the identification of the most aggressive type II tumours. *Br. J. Cancer*, 117(5):666–674, 2017.

[126] B. Saha, T. H. Evers, and M. W. Prins. How antibody surface coverage on nanoparticles determines the activity and kinetics of antigen capturing for biosensing. *Anal. Chem.*, 86(16):8158–8166, aug 2014.

[127] S. Saipanya, S. Lapanantnoppakhun, and T. Sarakonsri. Electrochemical deposition of platinum and palladium on gold nanoparticles loaded carbon nanotube support for oxidation reactions in fuel cell. *J. Chem.*, 2014:1–6, 2014.

[128] R. Saldova, W. B. Struwe, K. Wynne, G. Elia, M. J. Duffy, and P. M. Rudd. Exploring the glycosylation of serum CA125. *Int. J. Mol. Sci.*, 14(8):15636–15654, 2013.

[129] A. Santos. Fundamentals and Applications of Impedimetric and Redox Capacitive Biosensors. *J. Anal. Bioanal. Tech.*, 7(12):2155–9872, 2014.

[130] C. Schopf, A. Wahl, A. Martín, A. O'Riordan, and D. Iacopino. Direct Observation of Mercury Amalgamation on Individual Gold Nanorods Using Spectroelectrochemistry. *J. Phys. Chem. C*, 120(34):19295–19301, 2016.

[131] W. H. Scouten, J. H. Luong, and R. Stephen Brown. Enzyme or protein immobilization techniques for applications in biosensor design. *Trends Biotechnol.*, 13(5):178–185, 1995.

[132] A. N. Sekretaryova, M. Y. Vagin, A. P. Turner, and M. Eriksson. Electrocatalytic Currents from Single Enzyme Molecules. *J. Am. Chem. Soc.*, 138(8):2504–2507, 2016.

[133] N. R. Shanmugam, S. Muthukumar, and S. Prasad. Ultrasensitive and low-volume point-of-care diagnostics on flexible strips-a study with cardiac troponin biomarkers. *Sci. Rep.*, 6:33423–33433, 2016.

[134] A. Sharma, C. H. Han, and J. Jang. Rapid electrical immunoassay of the cardiac biomarker troponin I through dielectrophoretic concentration using imbedded electrodes. *Biosens. Bioelectron.*, 82:78–84, 2016.

[135] E. W. Silverton, M. A. Navia, and D. R. Davies. Three dimensional structure of an intact human immunoglobulin. *Proc. Natl. Acad. Sci. U. S. A.*, 74(11):5140–5144, 1977.

[136] N. G. Skinner and E. A. Hall. The relevance of an equivalent circuit for polyaniline using immittance spectroscopy. *Synth. Met.*, 63(2):133–145, 1994.

[137] P. R. Solanki, A. Kaushik, V. V. Agrawal, and B. D. Malhotra. Nanostructured metal oxide-based biosensors. *NPG Asia Mater.*, 3(1):17–24, jan 2011.

[138] M. E. Stephens, T. N. Ellis, J. S. Huebner, E. M. Kelly, and D. F. Bowers. Streptococcal Protein G Enhances Antibody Binding to Platinum Sensor Surfaces. *J. Sens. Technol.*, 05(01):1–6, 2015.

[139] J. Sun, Y. Xianyu, and X. Jiang. Point-of-care biochemical assays using gold nanoparticle-implemented microfluidics. *Chem. Soc. Rev.*, 43(17):6239–6253, 2014.

[140] Z. Taleat, C. Cristea, G. Marrazza, M. Mazloum-Ardakani, and R. Săndulescu. Electrochemical immunoassay based on aptamer–protein interaction and functionalized polymer for cancer biomarker detection. *J. Electroanal. Chem.*, 717-718:119–124, mar 2014.

[141] F. Tao, M. E. Grass, Y. Zhang, D. R. Butcher, J. R. Renzas, Z. Liu, J. Y. Chung, B. S. Mun, M. Salmeron, and G. A. Somorjai. Reaction-Driven Restructuring of Rh-Pd and Pt-Pd Core-Shell Nanoparticles. *Science (80-.).*, 322(5903):932–934, 2008.

[142] A. Tarasov, D. W. Gray, M. Y. Tsai, N. Shields, A. Montrose, N. Creedon, P. Lovera, A. O'Riordan, M. H. Mooney, and E. M. Vogel. A potentiometric biosensor for rapid on-site disease diagnostics. *Biosens. Bioelectron.*, 79:669–678, 2016.

[143] I. Taurino, G. Sanzó, F. Mazzei, G. Favero, G. De Micheli, and S. Carrara. Fast synthesis of platinum nanopetals and nanospheres for highly-sensitive non-enzymatic detection of glucose and selective sensing of ions. *Sci. Rep.*, 5:15277, 2015.

[144] P. B. Tchounwou, C. G. Yedjou, D. N. Foxx, A. B. Ishaque, and E. Shen. Lead-induced cytotoxicity and transcriptional activation of stress genes in human liver carcinoma (HepG 2) cells. *Mol. Cell. Biochem.*, 255(2):161–170, jan 2004.

[145] A. Tinazli, J. Tang, R. Valiokas, S. Picuric, S. Lata, J. Piehler, B. Liedberg, and R. Tampé. High-affinity chelator thiols for switchable and oriented immobilization of histidine-tagged proteins: A generic platform for protein chip technologies. *Chem. - A Eur. J.*, 11(18):5249–5259, 2005.

[146] P. Tomčík. Microelectrode arrays with overlapped diffusion layers as electroanalytical detectors: Theory and basic applications. *Sensors (Switzerland)*, 13(10):13659–13684, oct 2013.

[147] S. R. Torati, K. C. Kasturi, B. Lim, and C. G. Kim. Hierarchical gold nanostructures modified electrode for electrochemical detection of cancer antigen CA125. *Sensors Actuators, B Chem.*, 243:64–71, 2017.

[148] A. Tsigara, A. Benkhial, S. Warren, F. Akkari, J. Wright, F. Frehill, and E. Dempsey. Metal microelectrode nanostructuring using nanosphere lithography and photolithography with optimization of the fabrication process. *Thin Solid Films*, 537:269–274, 2013.

[149] X. Tu, Q. Xie, Z. Huang, Q. Yang, and S. Yao. Synthesis and characterization of novel quinone-amine polymer/carbon nanotubes composite for sensitive electrocatalytic detection of NADH. *Electroanalysis*, 19(17):1815–1821, 2007.

[150] E. Turkmen, S. Z. Bas, H. Gulce, and S. Yildiz. Glucose biosensor based on immobilization of glucose oxidase in electropolymerized poly(o-phenylenediamine) film on platinum nanoparticles-polyvinylferrocenium modified electrode. *Electrochim. Acta*, 123:93–102, 2014.

[151] A. P. Turner. Biosensors: Sense and sensibility. *Chem. Soc. Rev.*, 42(8):3184–3196, mar 2013.

[152] R. Valiokas, M. Östblom, F. Björefors, B. Liedberg, J. Shi, and P. Konradsson. Structural and kinetic properties of laterally stabilized, oligo(ethylene glycol)-containing alkylthiolates on gold: A modular approach. *Biointerphases*, 1(1):22–34, 2006.

[153] R. Valiokas, M. Östblom, S. Svedhem, S. C. Svensson, and B. Liedberg. Temperature-driven phase transitions in oligo(ethylene glycol)-terminated self-assembled monolayers. *J. Phys. Chem. B*, 104(32):7568–7569, 2000.

[154] R. Valiokas, S. Svedhem, S. C. Svensson, and B. Liedberg. Self-assembled monolayers of oligo(ethylene glycol)-terminated and amide group containing alkanethiolates on gold. *Langmuir*, 15(10):3390–3394, 1999.

[155] D. J. Vanderah, G. Valincius, and C. W. Meuse. Self-assembled monolayers of methyl 1-thiahexa(ethylene oxide) for the inhibition of protein adsorption. *Langmuir*, 18(12):4674–4680, 2002.

[156] J. Wang and H. Wu. Permselective lipidpoly(o-phenylenediamine) coatings for amperometric biosensing of glucose. *Anal. Chim. Acta*, 283(2):683–688, 1993.

[157] K. M. Wassum, V. M. Tolosa, J. Wang, E. Walker, H. G. Monbouquette, and N. T. Maidment. Silicon wafer-based platinum microelectrode array biosensor for near real-time measurement of glutamate in vivo. *Sensors*, 8(8):5023–5036, 2008.

[158] F. Wei, W. Liao, Z. Xu, Y. Yang, D. T. Wong, and C. M. Ho. Bio/abiotic interface constructed from nanoscale DNA dendrimer and conducting polymer for ultrasensitive biomolecular diagnosis. *Small*, 5(15):1784–1790, 2009.

[159] F. Weiland, K. Martin, M. K. Oehler, and P. Hoffmann. Deciphering the molecular nature of ovarian cancer biomarker CA125. *Int. J. Mol. Sci.*, 13(8):10568–10582, 2012.

[160] N. G. Welch, J. A. Scoble, B. W. Muir, and P. J. Pigram. Orientation and characterization of immobilized antibodies for improved immunoassays (Review). *Biointerphases*, 12(2):02D301, 2017.

[161] W. Wen, T. Bao, J. Yang, M. Z. Zhang, W. Chen, H. Y. Xiong, X. H. Zhang, Y. D. Zhao, and S. F. Wang. A novel amperometric adenosine triphosphate biosensor by immobilizing graphene/dual-labeled aptamers complex onto poly(o-phenylenediamine) modified electrode. *Sensors Actuators, B Chem.*, 191:695–702, 2014.

[162] Y. Xia and G. M. Whitesides. Soft lithography. *Annu. Rev. Mater. Sci.*, 28(1):153–184, 1998.

[163] S. Xiao, F. Xiao, Y. Hu, S. Yuan, S. Wang, L. Qian, and Y. Liu. Hierarchical nanoporous gold-platinum with heterogeneous interfaces for methanol electrooxidation. *Sci. Rep.*, 4(1):4370, 2014.

[164] H. Xu, J. R. Lu, and D. E. Williams. Effect of surface packing density of interfacially adsorbed monoclonal antibody on the binding of hormonal antigen human chorionic gonadotrophin. *J. Phys. Chem. B*, 110(4):1907–1914, 2006.

[165] C. Yan, X. Liu, R. Zhang, Y. Chen, and G. Wang. A selective strategy for determination of ascorbic acid based on molecular imprinted copolymer of o-phenylenediamine and pyrrole. *J. Electroanal. Chem.*, 780:276–281, 2016.

[166] H. M. Yasin, G. Denuault, and D. Pletcher. Studies of the electrodeposition of platinum metal from a hexachloroplatinic acid bath. *J. Electroanal. Chem.*, 633(2):327–332, 2009.

[167] J. L. Yin, Y. J. Lee, and J. Y. Park. Fabrication and characterization of micro-structured supercapacitor with nickel on porous copper. In *8th Annu. IEEE Int. Conf. Nano/Micro Eng. Mol. Syst. IEEE NEMS 2013*, pages 919–922, 2013.

[168] Y. Yin, Y. Lü, P. Wu, and C. Cai. Direct electrochemistry of redox proteins and enzymes promoted by carbon nanotubes. *Sensors*, 5(4-5):220–234, 2005.

[169] T. You, O. Niwa, M. Tomita, and S. Hirono. Characterization of platinum nanoparticle-embedded carbon film electrode and its detection of hydrogen peroxide. *Anal. Chem.*, 75(9):2080–2085, 2003.

[170] Y. Yu, J. Chen, and J. Zhou. Parallel plate lab on a chip based on digital microuidics for on-chip electrochemical analysis. *J. Micromechanics Microengineering*, 24(1):015020, 2014.

[171] L. G. Zamfir, I. Geana, S. Bourigua, L. Rotariu, C. Bala, A. Errachid, and N. Jaffrezic-Renault. Highly sensitive label-free immunosensor for ochratoxin A based on functionalized magnetic nanoparticles and EIS/SPR detection. *Sensors Actuators, B Chem.*, 159(1):178–184, 2011.

[172] D. K. Zeybek, B. Zeybek, N. Ö. Pekmez, u. Pekyardimci, and E. Kiliç. Development of an amperometric enzyme electrode based on poly(o-phenylenediamine) for the determination of total cholesterol in serum. *J. Braz. Chem. Soc.*, 23(12):2222–2231, 2012.

[173] X. Zhao, F. Pan, B. Cowsill, J. R. Lu, L. Garcia-Gancedo, A. J. Flewitt, G. M. Ashley, and J. Luo. Interfacial immobilization of monoclonal antibody and detection of human prostate-specific antigen. *Langmuir*, 27(12):7654–7662, 2011.

[174] Y. Zheng, H. Wang, and Z. Ma. A nanocomposite containing Prussian Blue, platinum nanoparticles and polyaniline for multiamplification of the signal of voltammetric immunosensors: highly sensitive detection of carcinoma antigen 125. *Microchim. Acta*, 184(11):4269–4277, 2017.

About author

Name, Surename: Ausra Baradoke
email: ausra.baradoke@nanolab.lt
Education:

- **2014–2019** PhD in Chemistry, Fizinių ir technologijos mokslų centras, Vilniaus universitetas, Vilnius, Lithuania, Thesis: Fabrication of miniaturised electrochemical sensor for cancerogenic biomarker detection.
  Supervisor: Prof. R. Pauliukaite, Prof. R.J.Forster
- **2018–2019** Part time PhD studies, Trinity College Dublin, The University of Dublin, Dublin, Ireland, Project: Finite element model simulations for interdigitated micro-array electrodes.
  Supervisor: Prof. K. McKelvey
- **2016–2019** Part time PhD studies, National Centre for Sensor Research, Dublin City UniversityDublin, Ireland, Project: Sensor platform design based on IDA electrodes for biomarker detection.
  Supervisor: Prof. R. J. Forster
- **2012–2014** Master degree of Physics, Lithuanian University of Educational Sciences, Vilnius, Lithuania, Thesis: Stability of silver nanoparticles in dendrimer matrix.
  Supervisor: Prof. R. Vaisnoras
- **2013–2014** Part time master degree studies, University of Vigo, Vigo, Spain Thesis: Sensor platform design based on ruthenium and graphene nanostructures
  Supervisors: Prof. E. Gonzalez-Romero and Prof. Isabel Pastoriza-Santos
- **2008–2012** Bachelor degree in Physics, Lithuanian University of Educational Sciences, Vilnius, Lithuania, Thesis: Optical and structural study of hybrid system of dendrimer-silver nanoparticles
  Supervisor: Dr. Loreta Rasteniene

Experience:

- **2014.04–2016.09** Scientist, ERUMPO Ltd, Vilnius, Lithuania, Skills: biological sample preparation, antibody immobilisation on hydrogel and SAM, characterisation based on Ellipsometry Imaging, biomarker detection using Au nanoparticles (enhanced with Ag ions), Project: Biochip technology for detection of cancer biomarkers., "Intelektas LT" 2013.11-2015.09 VP2-1.3-uM-02-K-04-122

- **2016.04–2016.12** Junior scientist, Center for Physical Sciences and Technology, Vilnius, Lithuania, Project: graphene supercapacitor powered FET all carbon circuit for sensing applications., G-SUPERCAP, 3200-P325, LAT-16002
- **2015.10–2016.05** Junior scientist, Center for Physical Sciences and Technology, Vilnius, Lithuania, Skills: fabrication of interdigitated microelectrodes arrays, modification with electroplating of Au or Pt, micro-contact printing of fibronectin for cell adhesion and hydrogen peroxide studies, Project: single cell on a chip platform for metabolite sensing and integrated analysis., (METASENS), CH-3-SMM-01-11
- **2014.07–2014.09** Junior scientistDepartment of Molecular Compound Physics, Center for Physical Sciences and Technology, Vilnius, Lithuania, Project: synthesis of triangular silver nanoparticles for enhancement of fluorescence in dyes for solar cell application.,
- **2014.02–2014.06** EngineerDepartment of Molecular Compound Physics, Center for Physical Sciences and Technology, Vilnius, Lithuania, Project: synthesis of Ag nanoparticles and preparation of thin films using spin coating technique.,
- **2012.09–2013.09** Engineer, Department of Molecular Compound Physics, Center for Physical Sciences and Technology, Vilnius, Lithuania
- **2010.09–2013.09** Research Assistant, Liquid Crystals Laboratory, Lithuanian University of Educational Sciences, Vilnius, Lithuania

List of publications and presentations

Articles in CA WoS journals

1. Ausra Baradoke, Jurga Juodkazyte, Ignas Masilionis, Algirdas Selskis, Rasa Pauliukaite, Ramūnas Valiokas. Combined Soft Lithographic and Electrochemical Fabrication of Nanostructured Platinum Microelectrode Arrays for Miniaturized Sensor Applications. *Microelectronics and Engineering*, 206 (2019) 39-46
DOI: 10.1016/j.mee.2019.02.003

2. Ausra Baradoke, Isabel Pastorisa-Santos, Elisa Gonzalez-Romero, Screen printed GPH electrode modified with Ru nanoplates and PoPD polymer film for NADH Sensor Platform: Design and Characterization. *Electrochimica Acta*, 300 (2019) 316-323
DOI: 10.1016/j.electacta.2019.01.128

3. Ausra Baradoke, Bincy Jose, Rasa Pauliukaite, Robert J. Forster. Properties of Anti-CA125 Antibody Layers on Screen-Printed Carbon Electrodes Modified by Gold and Platinum Nanostructures. *Electrochimica Acta*, 306 (2019) 299-306
DOI: 10.1016/j.electacta.2019.03.081

Published contributions to academic conferences

1. Ausra Baradoke, Aneta Radzevič, Raimonda Celiešiūtė, Ramūnas Valiokas, Rasa Pauliukaite, Graphene for Electrochemical Detection of Biomarkers, Lithuanian National Physics Conference, Vilnius, Lithuania, 2015, June 17-19 (Poster Presentation).

2. Ausra Baradoke, Gintarė Garbenčiūtė, Vytautas Cėpla, Tomas Rakickas, Ramūnas Valiokas, PEG Methacrylate Hydrogels for Imaging Ellipsometry, The Optical Society IONS konferencija, Nanjing, China, 2015, July 9-12. (Poster Presentation).

3. Ausra Baradoke, Aneta Radzevic, Raimonda Celiesiute, Ramunas Valiokas, Rasa Pauliukaite, Graphene Electrodes for Electrochemical Detection of Biomarkers. 66th ISE Conference,Taipei, Taiwan, 2016 October 4-9 (Poster Presentation).

4. Ausra Baradoke, I. Pastorisa-Santos, E. Gonzalez Romero, Ruthenium Nanocomposites for Electrochemical Detection: Design and Modification of Graphene Electrodes for Biosensors. 66th ISE Conference,Taipei, Taiwan, 2016 October 4-9 (Poster Presentation).

5. Ausra Baradoke, Jurga Juodkazytė, Ignas Masilionis, Airina Mazėtytė, Vytautas Navikas, Martynas Gavutis, Ramūnas Valiokas, Rasa Pauliukaite, Soft Lithographic Fabrication of Electrodes for Detection of Hydrogen Peroxide. Chemistry and Chemistry Technology 2016, Vilnius, Lithuania, 2016 April 28-29 (Poster Presentation).

6. Ausra Baradoke, Jurga Juodkazytė, Ignas Masilionis, Airina Mazėtytė, Vytautas Navikas, Martynas Gavutis, Ramūnas Valiokas, Rasa Pauliukaite, Platinum Electrode Platform for Detection of Hydrogen Peroxide, Baltic Electrochemistry Conference, Helsinki, Finland, 2016 June 15-17 (Oral presentation).

7. Ausra Baradoke, Jurga Juodkazytė, Ignas Masilionis, Airina Mazėtytė, Vytautas Navikas, Martynas Gavutis, Ramūnas Valiokas, Rasa Pauliukaite, Formation of Electrodes for Detection of Hydrogen Peroxide, 67th Conference of International Electrochemistry Society, Haga, Netherlands, 2016 August 21-26 (Oral presentation).

8. Ausra Baradoke, Jurga Juodkazytė, Ignas Masilionis, Airina Mazėtytė, Vytautas Navikas, Martynas Gavutis, Ramūnas Valiokas, Rasa Pauliukaite, Formation of Electrodes for Detection of Hydrogen Peroxide. 67th Conference of International Electrochemistry Society, Haga, Netherlands, 2016 August 21-26 (Poster presentation).

9. Eliza Gonalez-Romero, L. Bounab, Ausra Baradoke, J. M. Gonzalez, Rui Gusmao, From Creativity to Industrialization: Design and Modification of SPEs for (Bio)sensors. First Workshop on electrochemistry devices (Bio)Sensors, Porto, Portugal, 2016 October 1-2 (Oral presentation).

10. Ausra Baradoke, Samantha Douman, Bincy Jose, Rasa Pauliukaite, Ramūnas Valiokas, Robert Forster, Development of an Electrochemical Biosensor Based on Nanomodified IDA Biochip for High Sensitivity Non-Labeled Biomarker Detection, 24th International Bioelectrochemistry Society Conference for Bioelectrochemistry and Bioenergetic. Lyon, France, 2017 July 3-7 (Oral presentation).

11. Ausra Baradoke, Jurga Juodkazytė, Ignas Masilionis, Rasa Pauliukaite, Ramūnas Valiokas, Nanostruktūrizuotos platinos elektrodai vandenilio peroksido detekcijai, 42-oji Lithuanian National Physics Conference, Vilnius, Lithuania, 2017 October 4-6 (Poster presentation).

12. Ausra Baradoke, Bincy Jose, Rasa Pauliukaite, Robert Forster, Label Free Impedimetric Detection of CA125 based on Gold and Plat-

inum nanostructures, NALS 2017, Oviedo, Spain, 2017 December 13-15 (Oral presentation).

13. Ausra Baradoke, Bincy Jose, Ramūnas Valiokas, Rasa Pauliukaite, Robert Forster, 3D Nanolithography for cells studies, Conference on Optics Atoms and Laser Applications, Okinawa, Japan, 2017 October 25-27 (Poster presentation).

14. Ausra Baradoke Technical University of Denmark (DTU) „PhD Summer School: Micro and Nano Sensors 2018", Project: Real Time Electrochemical Detection of Drugs from Microcontainers on a Disk, Lyngby, Denmark, 2018 August 19-30 (Poster presentation).

15. Ausra Baradoke, Kim McKelvey, Rasa Pauliukaite, Ramūnas Valiokas, Mike Lyons, Robert Forster. Cyclic Voltammetry of Interdigitated Working/Counter Microelectrode Array, 18th IEEEnano, Cork, Ireland, 2018 July 23-26 (Poster presentation).

16. Ausra Baradoke, Bincy Jose, Lukas Laurinavicius, Rasa Pauliukaite, Robert Forster, Impedimetric Immunosensors Based on Crosslinked Antibodies to Poly-L-Lysine, 23rd Topical Meeting of ISE, Vilnius, Lithuania, 2018 June 8-11 (Oral presentation).

17. Ausra Baradoke, Isabel Pastorisa-Santos, Elisa Gonzales-Romero, Catalytic Activity of Ruthenium Nanoparticles for NADH Sensing, 23rd Topical Meeting of ISE, Vilnius, Lithuania, 2018 June 8-11 (Poster presentation).

Research abroad: Half of research (2017-2018) in this thesis was performed in Dublin City University and Trinity College Dublin, in the Republic of Ireland.

Notes

Vilnius University Press
9 Saulėtekio Ave., Building III, LT-10222 Vilnius
Email: info@leidykla.vu.lt, www.leidykla.vu.lt
Print run copies 20